Master Thesis

Ultrafast magnetization dynamics in highly magnetostrictive thin films

submitted for the academic degree *Master of Science* in the subject of *Physics*

Constantin Walz

15.01.2025

1st Reviewer	Prof. Dr. Matias Bargheer
2nd Reviewer	Dr. Clemens von Korff Schmising
Supervisor	Dr. Alexander von Reppert

Ultrafast Dynamics in Condensed Matter
Institute of Physics and Astronomy
Faculty of Mathematics and Science
University of Potsdam

Abstract

Rare Earth-Iron ($REFe_2$) compounds are well known for their giant magnetostriction, with more than 1‰ lattice constant change when applying a magnetic field. Despite their widespread usage as ultrasonic transducers, their ultrafast magnetization dynamics have remained mostly unexplored. In this thesis, the transient magneto-optical Kerr effect (trMOKE) responses following laser excitation of $TbFe_2$, $DyFe_2$ and $Tb_{0.3}Dy_{0.7}Fe_2$ are investigated. The effects of different magnetic anisotropies are studied by a systematic comparison between the three materials in different sample configurations. While $TbFe_2$ and $DyFe_2$ exhibit strong, but opposing magnetocrystalline anisotropies, combining them to $Tb_{0.3}Dy_{0.7}Fe_2$ leads to a significantly lower anisotropy. Additionally, differences in crystalline texture are expected to lead to reduced anisotropy in films thinner than $\approx 100\,\mathrm{nm}$.

The intrinsic de- and remagnetization dynamics are measured in almost homogeneously pumped and probed thin 20 to 40 nm films. The trMOKE signals show opposing signs for $TbFe_2$ and $DyFe_2$ at low excitation fluences, likely due to opposing anisotropies. A compensation effect between Tb and Dy in $Tb_{0.3}Dy_{0.7}Fe_2$ leads to an apparently shorter remagnetization timescale.

The trMOKE signals of thick 335 to 450 nm $TbFe_2$ films exhibit strong signatures of picosecond strain pulses, which couple to the magnetization via inverse magnetostriction. Their timing, shape and sign is rationalized with strain simulations obtained from the udkm1dsim-toolbox. It is demonstrated that a significant part of the total observed signal is caused by the magneto-elastic contribution of the quasi-static strain.

Under an oblique magnetic field, a strong precession with opposing phase and sign is observed in thin $TbFe_2$ and $DyFe_2$, but not in $Tb_{0.3}Dy_{0.7}Fe_2$ due to the same compensation mechanism as before. The thick $TbFe_2$ samples show no precession, likely due to their large magnetocrystalline anisotropy. The magnetization merely follows the strain with a delay of 5 ps, which is interpreted as an intrinsic timescale of the magnetization response set by the Landau-Lifshitz-Gilbert equation.

Kurzdarstellung

Seltene-Erden-Eisen-Verbindungen ($REFe_2$) sind bekannt für ihre riesige Magnetostriktion mit einer Änderung der Gitterkonstante von über 1‰ bei Anlegen eines Magnetfelds. Trotz ihrer häufigen Verwendung als Ultraschallwandler ist ihre ultraschnelle Magnetisierungsdynamik noch weitestgehend unerforscht. In dieser Arbeit werden die transienten magneto-optischen Kerr-Effekt (trMOKE) Signale von $TbFe_2$, $DyFe_2$ und $Tb_{0.3}Dy_{0.7}Fe_2$ nach einer Laseranregung untersucht. Die Auswirkungen unterschiedlicher magnetischer Anisotropien werden durch einen systematischen Vergleich der drei Materialien in unterschiedlichen Probenstrukturen diskutiert. Während $TbFe_2$ und $DyFe_2$ eine starke, aber entgegengesetzte magnetokristalline Anisotropie zeigen, führt ihre Kombination in $Tb_{0.3}Dy_{0.7}Fe_2$ zu einer deutlich niedrigeren Anisotropie. Zusätzlich wird eine reduzierte Anisotropie in dünnen Filmen unter 100 nm aufgrund unterschiedlicher kristalliner Texturen erwartet.
Die intrinsische De- und Remagnetisierungsdynamik wird in annähernd homogen angeregten und abgefragten, 20 bis 40 nm dünnen Filmen bestimmt. Die trMOKE-Signale zeigen bei kleinen Anregungsfluenzen entgegengesetzte Vorzeichen für $TbFe_2$ und $DyFe_2$, wahrscheinlich aufgrund der entgegengesetzten Anisotropien. Ein Kompensationseffekt zwischen Tb und Dy führt zu einer scheinbar kürzeren Remagnetisierungszeitskala in $Tb_{0.3}Dy_{0.7}Fe_2$.
Die trMOKE-Signale von 335 bis 450 nm dicken $TbFe_2$-Filmen zeigen starke Signaturen von Hyperschallpulsen, welche über inverse Magnetostriktion an die Magnetisierung koppeln. Ihre Ankunftszeiten, Formen und Vorzeichen werden durch Schallsimulationen aus der udkm1dsim-Toolbox rationalisiert. Es konnte gezeigt werden, dass der Großteil des beobachteten Signals durch den magneto-elastischen Beitrag der quasi-statischen Gitterausdehnung erklärt werden kann.
Unter einem geneigten Magnetfeld wird eine starke Präzession im dünnen $TbFe_2$ und $DyFe_2$ mit entgegengesetzten Vorzeichen und Phase beobachtet, nicht jedoch in $Tb_{0.3}Dy_{0.7}Fe_2$ wegen des gleichen Kompensationsmechanismus wie vorher. Die dicken $TbFe_2$-Proben zeigen keine Präzession, wahrscheinlich aufgrund ihrer großen magnetokristallinen Anisotropie. Die Magnetisierung folgt lediglich der Gitterverformung mit einer Verzögerung von 5 ps, was als intrinsische Zeitskala der Magnetisierungsantwort durch die Landau-Lifshitz-Gilbert-Gleichung interpretiert wird.

Contents

1 Introduction and motivation

Since the advent of the digital age, the demand for high-performance magnetic hard disk drives (HDD) has continuously increased. The rise of the storage density creates challenges, as very small bits are more susceptible to thermally induced random magnetization flips [9]. This can be circumvented by choosing a magnetic material with a large anisotropy, however this necessitates stronger writing fields. Several techniques were developed to overcome this issue. For example, the anisotropy can be temporarily reduced by ultrafast heating with a laser pulse which allows for a much smaller writing field (heat-assisted magnetic recording, HAMR) [40]. Apart from that, there is an ongoing search for alternative magnetic storage solutions that do not rely on heat, for example by using strain pulses to overcome the anisotropy barrier [29, 52].
This thesis focuses on Rare Earth-Iron ($REFe_2$) compounds as promising materials for future applications. These compounds are known for their giant magnetostriction at room temperature since the 1970s [7], and were initially used as ultrasonic transducers for naval applications like sonar. Magnetostriction refers to an expansion or contraction (strain) induced in a magnetic material when a magnetic field is applied. Terbium-Iron ($TbFe_2$) exhibits one of the largest magnetostriction, with over 2‰ strain generated by applying an external field. However it also has a strong magnetic anisotropy, resulting in a high saturation field. The anisotropy can be reduced by mixing $TbFe_2$ with Dysprosium-Iron ($DyFe_2$) to create Terfenol-D ($Tb_{0.3}Dy_{0.7}Fe_2$). Terfenol-D exhibits the same giant magnetostriction without the drawbacks of the high anisotropy.
Magnetostriction opens up new opportunities to manipulate the magnetization without heat through strain, an effect known as inverse magnetostriction. In 2013, Kovalenko at al. [27] demonstrated theoretically that this can be used to switch the magnetization in $Tb_{0.3}Dy_{0.7}Fe_2$. A strain pulse with the right amplitude and duration switches the magnetization between different equilibrium states. While their work was purely theoretical, and relied on idealized strain pulse properties, it nonetheless highlighted the potential of these compounds for magneto-acoustic switching. Additionally, these compounds could serve as field-tuneable transducers, where the shape of a picosecond strain pulse generated by ultrafast laser excitation depends on the external field amplitude [35].
The group of Prof. Matias Bargheer has already investigated the ultrafast dynamics of $REFe_2$ compounds and elementary rare earths after laser excitation. The core techniques include ultrafast x-ray diffraction (UXRD) as a powerful technique to measure the transient strain response in a crystalline material, and the transient magneto-optical Kerr effect (trMOKE), which allows direct measurement of the magnetization. Rare earth elements like Dy and Ho exhibit giant magnetostriction on a picosecond timescale [55, 44]. It was shown that the magnetostriction changes the shape of the generated GHz strain pulse [56], and that the effect is influenced by an external magnetic field [35]. However, a full control of the picosecond acoustics through a magnetic

field is yet to be achieved. Problems include the different timescales of the electronic (sub-picosecond) and magnetic stresses (several picoseconds), and the fact that due to the low Curie temperature in elementary rare earths the effects are limited to cryogenic temperatures.
Therefore, it is interesting to explore the $REFe_2$ compounds, which exhibit giant magnetostriction also at room temperature. Their time-resolved magnetization dynamics are still relatively unexplored, and the timescales of the ultrafast demagnetization and ultrafast magnetostriction have not yet been finally determined. The laser-induced lattice dynamics of thick $TbFe_2$ specimen were measured with UXRD by Zeuschner et al. [64]. Comparison between UXRD and trMOKE revealed that signatures of strain pulses also appear in the trMOKE signal, which has been verified and further analyzed by Parpiiev et al. [41]. However, a detailed experimental analysis of the origin of these strain signals in the trMOKE response is still pending.
In this thesis, a systematic comparison of the trMOKE response between three different $REFe_2$ materials with varying anisotropies $TbFe_2$, $DyFe_2$ and $Tb_{0.3}Dy_{0.7}Fe_2$ is presented. Different sample structures are used to disentangle strain-dependent magnetization signals from the pure magnetic response. With this approach, the timescales for the ultrafast de- and remagnetization are determined and the strain contribution to the total trMOKE signal is extracted. The effects of unipolar stain pulses on the magnetic precession observed under oblique magnetic fields, such as resonant enhancement or suppression, are explored. Finally, a comparison between transient reflectivity and trMOKE is used to identify the origin of the strain pulses in the trMOKE response.

2 Theoretical background

The following sections aims to provide the theoretical background necessary to understand the measurements and results of this work. After introducing the material class of $REFe_2$ compounds and their general magnetic properties, the free energy model is presented as an important framework for describing magnetization dynamics. The different contributions to the free energy are discussed, especially the magneto-elastic coupling, which is related to magnetostriction, and the magnetocrystalline anisotropy. Afterwards, the free energy is incorporated into the Landau-Lifshitz-Gilbert equation, which describes the magnetization dynamics. The final part of the chapter focuses on the mechanism behind magneto-optic effects, which are used to probe the magnetization response throughout this thesis.

2.1 Magnetism and magnetostriction in $REFe_2$ compounds

$REFe_2$ compounds are known for their giant magnetostriction since the 1970s [7]. Commonly used materials include $TbFe_2$ and $DyFe_2$, which both crystallize in a cubic C15 Laves phase, that is depicted in Figure 1. The rare earth atoms contribute a large magnetic moment of $9.3\mu_B$ [9] and are responsible for the large anisotropy and magnetostriction. While elementary Tb and Dy also exhibit giant magnetostriction, their low Curie temperatures prevent this effect from being observed at room temperature. In combination with Fe, the Curie temperature is significantly increased above 360 °C [19]. The two Fe atoms also carry a magnetic moment of $1.65\mu_B$ each, and they couple antiferromagnetically with the RE moment. The resulting compound thus exhibits a ferrimagnetic behavior with a net magnetic moment of $(9.3 - 2 \cdot 1.65)\,\mu_B = 6\mu_B$ [9].
The magnetostriction is defined as the

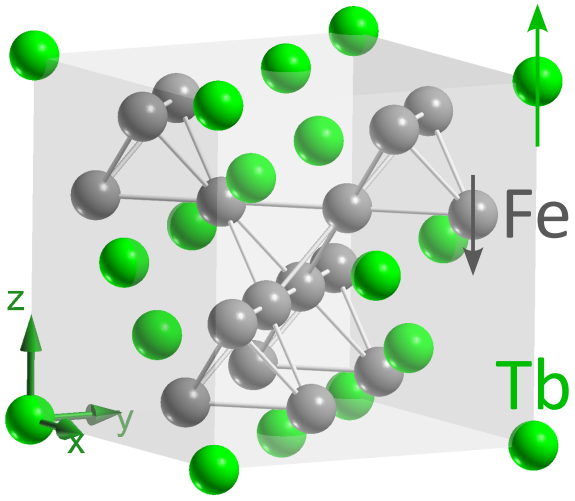

Figure 1: Sketch of the C15 Laves phase crystal structure of $TbFe_2$. The magnetic moments of Tb and Fe are antiferromagneticly coupled, resulting in a ferrimagnetic behavior. Data from [36] and plotted with [50].

relative length change of a material when an external magnetic field is applied [19]:

$$\lambda = \frac{\Delta l}{l}. \tag{1}$$

In an amorphous or polycrystalline material, the strength of the magnetostriction is characterized by the magnetostrictive constant [19]:

$$\frac{3}{2}\lambda_S = \lambda_\parallel - \lambda_\perp, \tag{2}$$

where $\lambda_\parallel - \lambda_\perp$ is difference between the relative length change parallel and perpendicular to the applied magnetic field. At a microscopic level, or in a monocrystalline sample, the magnetostrictive constant is defined with respect to specific crystallographic directions, such as λ_{100} or λ_{111}. The giant magnetostriction in $TbFe_2$ is characterized by a large $\lambda_S \approx 10^{-3}$, compared to $\lambda_S \approx 10^{-5}$ for the elementary ferromagnets Fe or Ni [19].

2.2 The free energy model

The free energy F is a thermodynamical concept for describing the equilibrium state and dynamics of the magnetization. It represents the energy required to align the magnetization, i.e. a single macro-spin, in a specific direction. In equilibrium, the magnetization is orientated so that the free energy is minimized. Any deviations from this equilibrium require additional energy, typically provided in the form of an external magnetic field that forces the magnetization along a different direction. The free energy can be written as a sum of various contributions that are described in the following [25]:

$$F = F_\mathrm{Z} + F_\mathrm{S} + F_\mathrm{ani} + F_\mathrm{me}. \tag{3}$$

Depending on the complexity of the described system, there are other contributions that are neglected here.

2.2.1 Zeeman energy

The Zeeman energy describes the energy of a magnetic dipole in an external magnetic field. It is given by [15]:

$$F_\mathrm{Z} = -\mu_0 M_S \vec{m} \cdot \vec{H}_\mathrm{ext}, \tag{4}$$

where μ_0 is the vacuum permeability, M_S the saturation magnetization, $\vec{m} = \vec{M}/M_S$ the normalized magnetization vector and $\vec{H}_\mathrm{ext}$ the external field. As expected from electrodynamics, this energy is minimized for a parallel alignment of $\vec{m}$ and $\vec{H}_\mathrm{ext}$, and maximized for an antiparallel alignment.

2.2.2 Shape anisotropy

The shape anisotropy or demagnetization energy, as the name suggests, introduces a preferential orientation of the magnetization based on the macroscopic shape of the sample. In its most general form, it is given by [15]:

$$F_{\mathrm{S}} = \frac{\mu_0}{2} M_S^2 \left(\vec{m} \cdot \underline{N} \cdot \vec{m}\right). \tag{5}$$

The demagnetization tensor $\underline{N}$ contains the information about the shape of the sample. For a very thin film, like in the samples used here, it reduces to:

$$F_{\mathrm{S}} = \frac{\mu_0}{2} M_S^2 m_z^2. \tag{6}$$

In this scenario the shape anisotropy is minimized if the magnetization is orientated in-plane ($m_z = 0$), thus there is an in-plane easy plane and an out-of-plane hard axis, as illustrated in Figure 2(a). The shape anisotropy originates from the dipole-dipole interaction between magnetic moments, which favors a $\rightarrow\rightarrow$ alignment over a $\uparrow\uparrow$ alignment.

2.2.3 Magnetocrystalline anisotropy

The magnetocrystalline anisotropy is an additional anisotropy that is created by the interaction between the magnetization and the crystal lattice. A more detailed discussion of its origin is provided in Section 2.3. In case of a cubic crystal structure, like in the $REFe_2$ compounds, it has the following form [12, p. 41]:

$$F_{\mathrm{ani}} = K_1 \left(m_x^2 m_y^2 + m_x^2 m_z^2 + m_y^2 m_z^2\right) + K_2 \left(m_x^2 m_y^2 m_z^2\right). \tag{7}$$

The parameters K_1 and K_2 are the cubic anisotropy constants. Their signs and relative magnitudes determine the orientation, for a positive K_1 (Figure 2(b)), the resulting easy axes are aligned with the crystallographic [100] directions, whereas a negative K_1 (Figure 2(c)) leads to easy axes along [111].

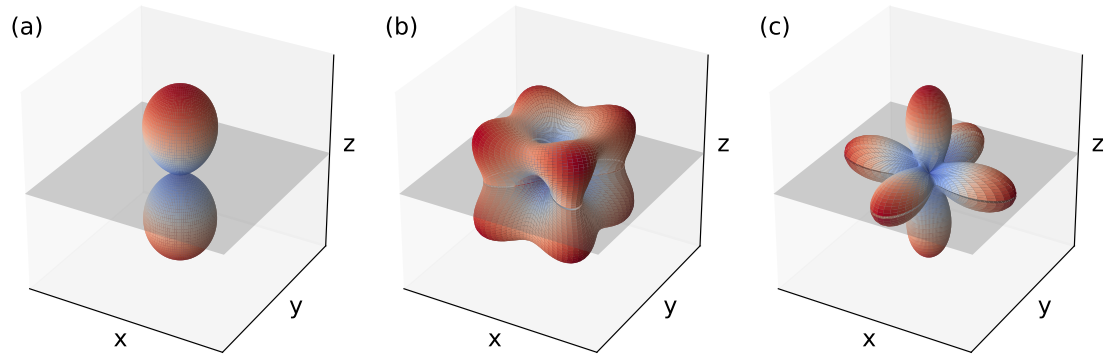

Figure 2: Free energy surfaces $F(\theta, \varphi)$ for a dominating shape anisotropy (a), a dominating positive K_1 cubic anisotropy (b) and a dominating negative cubic anisotropy (c).

2.2.4 Magneto-elastic energy

The magneto-elastic energy describes the magnetostriction in the free energy framework. It is given by [12]:

$$F_{\mathrm{me}} = b_1 \left(\eta_{xx} m_x^2 + \eta_{yy} m_y^2 + \eta_{zz} m_z^2\right) + b_2 \left(\eta_{xy} m_x m_y + \eta_{xz} m_x m_z + \eta_{yz} m_y m_z\right). \quad (8)$$

The first term with b_1 corresponds to the coupling between the magnetization and a longitudinal strain η_{ii}, while the second term with b_2 describes the interaction between the magnetization and a shear strain η_{ij}. Longitudinal strain is described by the relative length change $\Delta l/l_0$ in a specific direction. In a more general way, the strain is defined as the spatial derivative of the displacement field $\vec{u}\,(x, y, z)$:

$$\eta_{ij} = \frac{1}{2}\left(\frac{\partial u_i}{\partial j} + \frac{\partial u_j}{\partial i}\right), \quad (9)$$

which simplifies to

$$\eta_{ii} = \frac{\partial u_i}{\partial i} \quad (10)$$

for a longitudinal strain with $i = j$. The displacement field is the difference between the atom positions before and after deformation: $\vec{u} = \vec{r}' - \vec{r}$.
In $REFe_2$ compounds, shear magnetostriction is typically much larger than longitudinal magnetostriction: $b_2 \gg b_1$. This is attributed to crystal and orbital symmetries, as discussed in Section 2.3.
The magnetoelastic constants b_i are related to the magnetostrictive parameter λ as follows [12]:

$$\lambda_{100} = -\frac{2b_1}{3\left(C_{11} - C_{12}\right)}, \quad (11)$$

$$\lambda_{111} = -\frac{b_2}{3C_{44}}. \quad (12)$$

The two quantities are related by certain elements of the elastic tensor C. This tensor is analogous to the spring constant in the generalized Hooke's law:

$$\sigma_{ij} = C_{ijkl}\eta_{kl} \quad (13)$$

$$\overset{\text{Voigt}}{\Leftrightarrow} \sigma_m = C_{mn}\eta_n \quad (14)$$

where σ_{ij} is the stress, directed towards i and acting on surface j. Compare Figure 3 for a geometrical representation. The Voigt notation uses symmetry arguments to reduce the number of components of the elastic tensor from 81 down to 21 and also reduces C from a $3 \times 3 \times 3 \times 3$ tensor to a 6×6 matrix [15, 20]. The elements of the elastic tensor are material specific. Equations (11) and (12) show again that the parameter b_1 describes the longitudinal magneto-elastic coupling and b_2 describes the shear magneto-elastic coupling.

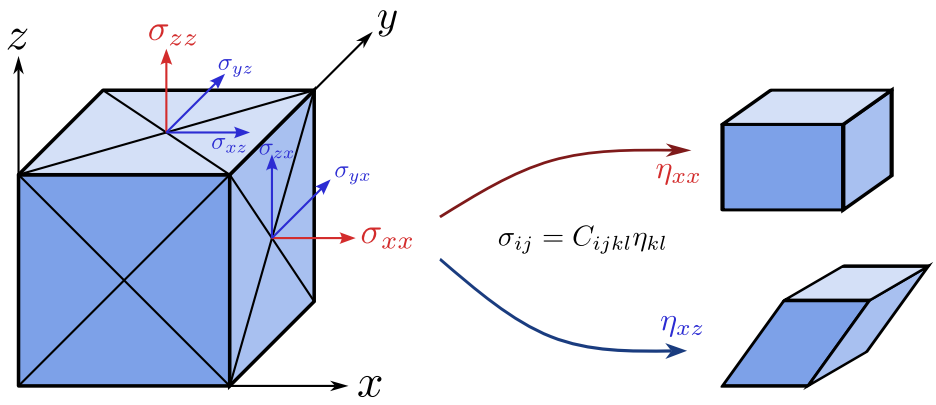

Figure 3: Definitions of the components of the stress tensor σ_{ij} (left), and the effects of longitudinal (red) and shear (blue) strain η_{kl}. Longitudinal stress/strain has the same indices $i = j$, while for shear stress/strain $i \neq j$. Figure adapted from [15].

2.3 Origin of magnetostriction and anisotropy

	Tb	Dy
$4f$ e^- config.	$4f^8$	$4f^9$
$\mu_S = 2\sum s_i$ $[\mu_\mathrm{B}]$	6	5
$\mu_L = \sum \ell_i$ $[\mu_\mathrm{B}]$	3	5
$\mu_J = \mu_S + \mu_L$ $[\mu_\mathrm{B}]$	9	10

Table 1: Spin and orbital magnetic moments for Tb and Dy in units of $\mu_\mathrm{B} = e\hbar/(2m_e)$. Adapted from [12].

Rare earth-iron compounds are characterized by their giant magnetostriction. In a microscopic view, this corresponds to a significant change of the lattice constant by over 1‰ when an external magnetic field is applied. For comparison, the elementary ferromagnets Iron (Fe), Nickel (Ni) and Cobalt (Co) only exhibit a magnetostrictive strain on the order of 0.01‰ to 0.1‰ [19]. This giant magnetostriction is linked to a large magnetocrystalline anisotropy, and the current textbook explanation is summarized in this section based on [4].

The magnetism of the rare earth atoms originates from their partially filled $4f$ orbitals. For Tb, it is filled with 8 electrons (configuration $[\mathrm{Xe}]\,4f^8\,(5d6s)^3$) and for Dy with 9 electrons (configuration $[\mathrm{Xe}]\,4f^9\,(5d6s)^3$). The resulting spin and orbital magnetic moments according to Hund's rule are shown in Table 1. Note how for Tb the theoretical value of the total magnetic moment $\mu_J = 9\mu_B$ almost matches the measured value of $9.3\mu_B$. Using spherical harmonic functions $Y_{\ell m}(\theta, \varphi)$ the approximate electron density in the partially filled $4f$ modeled as [53]:

$$\rho(r, \theta, \varphi) = \rho(r)^2 \cdot \sum_m |Y_{3m}(\theta, \varphi)|^2 . \tag{15}$$

The polar angle is represented by θ, while φ denotes the azimuthal angle. The resulting electron distributions are oblate for both Tb and Dy, as presented in Figure 4.

Figure 4: Approximate shape of the $4f$ electron cloud density for Tb (green) and Dy (red). Inspired by [12].

The interaction of these localized, anisotropic $4f$ orbitals with the neighboring ions gives rise to magnetostriction. Due to strong spin-orbit coupling of the RE elements, the spin magnetic moment is rigidly aligned to the orbital magnetic moment. Consider now the situation depicted in Figure 5: Initially, the electron cloud is orientated so that it exerts equal Coulomb forces on all surrounding positive ions, leading to a stable state. When an external magnetic field rotates the magnetization as depicted in the graphic, the orbital follows this rotation due to spin-orbit coupling. Now, the left and right ions are subjected to a stronger Coulomb attraction than lower and upper ions, which leads to a deformation of the unit cell, preferentially along the [111]-axes. This is reflected in by the fact that $\lambda_{111} \gg \lambda_{100}$, or equivalently $b_2 \gg b_1$ according to Equations (11) and (12). This specific model of magnetostriction is known as "anisotropy striction" that is different from the mechanism of "exchange striction", which explains magnetostriction for isotropic $4f$-orbitals based on the distance dependence of the magnetic exchange constant [24].

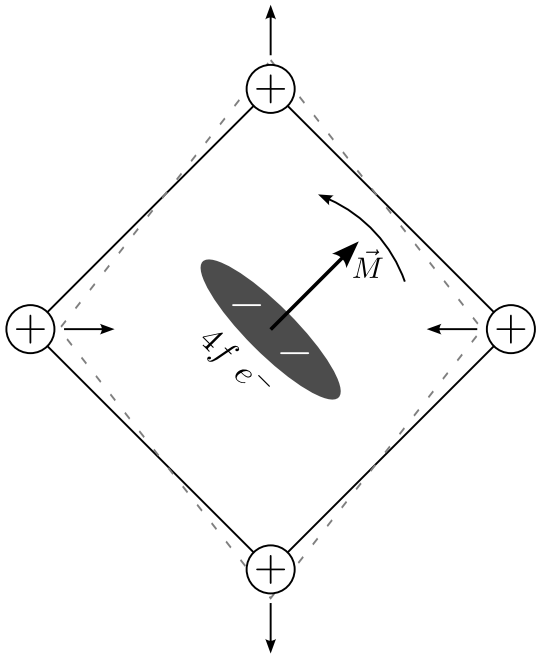

Figure 5: An external magnetic field rotates the magnetization. Due to strong spin-orbit coupling, the associated anisotropic $4f$ orbital rotates with it. Different Coulomb forces on the positive ions lead to a deformation of the lattice. Figure adapted from [12].

The giant magnetostriction of the $REFe_2$ compounds is inherently linked to their large magnetocrystalline anisotropy. Both effects arise from spin-orbit coupling and interactions of the RE $4f$ electrons with the neighboring atoms. The magnetocrystalline anisotropy introduces preferences for the orientation of the magnetization (easy axes), resulting in high saturation fields along the hard axes. As the name suggests the easy axes are often aligned with specific crystal directions. Despite the same underlying principles as for the magnetostriction, the anisotropies of $TbFe_2$ and $DyFe_2$ oppose each other. While the magnetization in $TbFe_2$ prefers a [111]-orientation, in $DyFe_2$ it tends to align with the [100]-axes. Patrick et al. [42] show that different quantum numbers of the $4f$ electrons in Tb and Dy cause opposing magnetocrystalline anisotropies, despite sharing similar orbital shapes and magnetostrictive properties. This allows for the creation of Terfenol-D, a material with a Tb to Dy ratio of $\approx 30/70$, where the magnetocrystalline anisotropies effectively cancel, while retaining the giant magnetostriction of the its source materials.

2.4 Magnetization dynamics

The free energy does not only allow to model the steady state magnetization direction but also provides a basis to describe the magnetization dynamics, which are governed by the Landau-Lifshitz-Gilbert equation. The magneto-elastic term in the free energy couples the lattice strain to the magnetization dynamics. To better understand how the strain dynamics affect the magnetization via magneto-elastic coupling, the mechanisms behind strain simulations with the udkm1dsim toolbox are also explained.

2.4.1 The effective field and the LLG equation

The effective field $\vec{H}_{\text{eff}}$ is central to describing the magnetization dynamics with the Landau-Lifshitz-Gilbert (LLG) equation. It is defined as the gradient of the free energy with respect to the magnetization direction [15]:

$$\vec{H}_{\text{eff}} = -\frac{1}{\mu_0 M_S} \nabla_m F. \tag{16}$$

As the gradient is a linear operator, all free energy contributions can be converted to a corresponding effective field contribution:

$$\vec{H}_{\text{Z}} = \vec{H}_{\text{ext}} \tag{17}$$

$$\vec{H}_{\text{S}} = -M_S m_z \hat{z} \tag{18}$$

$$\vec{H}_{\text{ani}} = -\frac{2K_1}{\mu_0 M_S} \begin{pmatrix} m_x \left(m_y^2 + m_z^2\right) \\ m_y \left(m_x^2 + m_z^2\right) \\ m_z \left(m_x^2 + m_y^2\right) \end{pmatrix} - \frac{2K_2}{\mu_0 M_S} \begin{pmatrix} m_x m_y^2 m_z^2 \\ m_y m_x^2 m_z^2 \\ m_z m_x^2 m_y^2 \end{pmatrix} \tag{19}$$

$$\vec{H}_{\text{me}} = -\frac{2b_1}{\mu_0 M_S} \begin{pmatrix} \eta_{xx} m_x \\ \eta_{yy} m_y \\ \eta_{zz} m_z \end{pmatrix} - \frac{b_2}{\mu_0 M_S} \begin{pmatrix} \eta_{xy} m_y + \eta_{xz} m_z \\ \eta_{xy} m_x + \eta_{yz} m_z \\ \eta_{xz} m_x + \eta_{yz} m_y \end{pmatrix} \tag{20}$$

There exist different definitions of the LLG equation, however in this thesis the following convention is used [57]:

$$\frac{\partial \vec{m}}{\partial t} = \underbrace{-\mu_0 \gamma \vec{m} \times \vec{H}_{\text{eff}}}_{\text{precession}} - \underbrace{\mu_0 M_S \gamma \alpha \vec{m} \times \left(\vec{m} \times \vec{H}_{\text{eff}}\right)}_{\text{damping}}. \tag{21}$$

The equation consists of two terms: a precession term proportional to the gyromagnetic ratio γ and a damping term with a damping constant α. The interplay between the effective field and the magnetization, which are both time-dependent, leads to nontrivial magnetization dynamics. In general, after a change of the effective field, the magnetization precesses around the new effective field direction. The damping term leads to an alignment with the new effective field over time, as sketched in Figure 6.

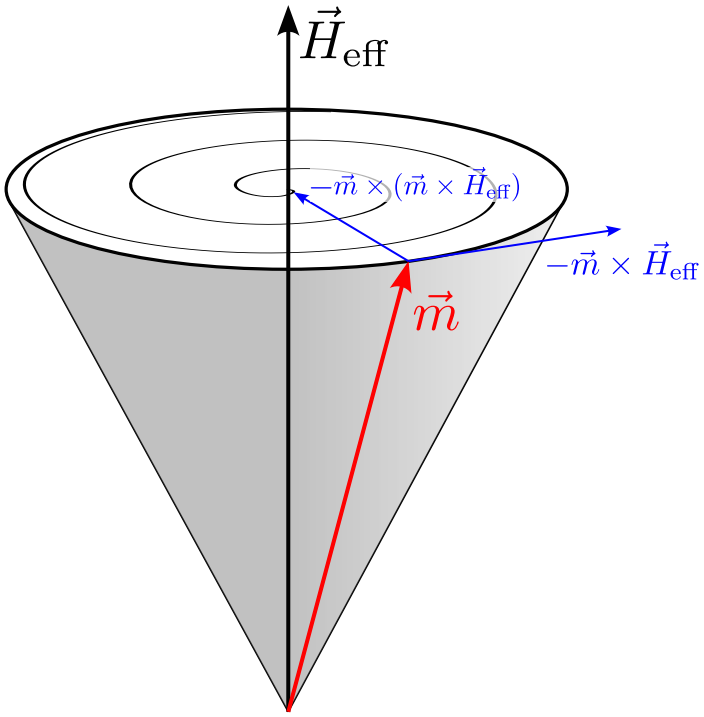

Figure 6: Geometry of the different terms in the LLG equation. The precession term $\propto -\vec{m} \times \vec{H}_{\text{eff}}$ leads to a circular trajectory of the magnetization around the effective field. The damping term $\propto -\vec{m} \times \left(\vec{m} \times \vec{H}_{\text{eff}}\right)$ is directed inwards, toward the effective field and aligns the magnetization over time. Figure adapted from [15].

2.4.2 Simulations of the strain dynamics

In highly magnetostrictive materials the strain is expected to influence the magnetization dynamics via inverse magnetostriction [27]. However the strain pulses that are used in theoretical model are often very idealized and oversimplified versions of the potentially complex strain patterns that arise in real laser-excited heterostructures. The udkm1dsim toolbox [48, 49] provides a realistic model for the strain in heterostructures that contains multireflections of strain pulses. The toolbox simulates the strain dynamics following the laser excitation using a one-dimensional model of masses and springs. Thus it is limited to longitudinal strain only. Performing a simulation requires several steps, some of which require user input, while other are done automatically.
First, the sample structure is defined with the different materials and thicknesses. Then, the deposited energy by the pump beam is calculated using a multilayer absorption model [28] (Figure 7(b)). In the spring model, this added energy leads to a stress that is represented by spacer sticks inserted into the chain (Figure 7(a)).

In a one-temperature model, the absorbed energy heats up the phonons. The toolbox then calculates a heat diffusion model both in space and time:

$$C_V(T)\frac{\partial T}{\partial t} = \frac{\partial}{\partial z}\left(\kappa(T)\frac{\partial T}{\partial z}\right) + S, \tag{22}$$

where C_V is the heat capacity at constant volume, T is the temperature, κ the thermal conductivity and a source term S. The resulting spatio-temporal temperature map $T(z,t)$ in Figure 7(c) shows the excited surface layers with red colors.
The extension of the springs back to their initial length results in an expansion of the lattice, so a positive strain. This quasi-static strain from thermal expansion is largest where the longest spacer sticks have been inserted, i.e. in the near surface region where most of the light was absorbed. In the spatio-temporal strain map $\eta(z,t)$ in Figure 7(d), it appears as a diffuse red (positive) area in the near surface region.
Additionally, as the stress (depicted as the tension of the springs) decreases with depth, a compressive strain wave is launched both upwards and downwards. The upper part of this strain wave is reflected from the surface and undergoes a phase shift there, thus the initial compressive strain wave is followed by an expansion. This can be seen as diagonal blue and red lines in Figure 7(d) and results in a bipolar strain profile in time. The slope of these lines depends on the sound velocity of the respective layer, for example the sapphire substrate (bottom layer) has a significantly higher sound velocity than the other layers, causing a steeper strain feature there.
The propagation of longitudinal elastic waves is given by the elastic wave equation [34]:

$$\rho\frac{\partial^2 u_3}{\partial t^2} = \frac{\partial}{\partial z}\left(C_{3333}\eta_{33} - \sigma_{33}^{\text{ext}}\right), \tag{23}$$

with the mass density ρ and an external stress σ_{33}^{ext}.
Thermal energy transport into the substrate reduces the temperature over longer timescales of 100s of picoseconds and results in a decreasing quasi-static strain on longer timescales. In the spring model, this can be understood as a redistribution and general decrease of the spacer stick lengths, until the initial state is reached again.
The observable strain $\eta(t)$ in the different layers between d_1 and d_2 is calculated by integrating over the spacial axis of the strain map, using the absorption profile $A(z)$ of the 400 nm probe light as a weighting function:

$$\eta(t) \propto \int_{d_1}^{d_2} \eta(z,t)A(z)\,\mathrm{d}z. \tag{24}$$

Exemplary strain responses of the $TbFe_2$ and Nb layers are provided in Figure 7(e).

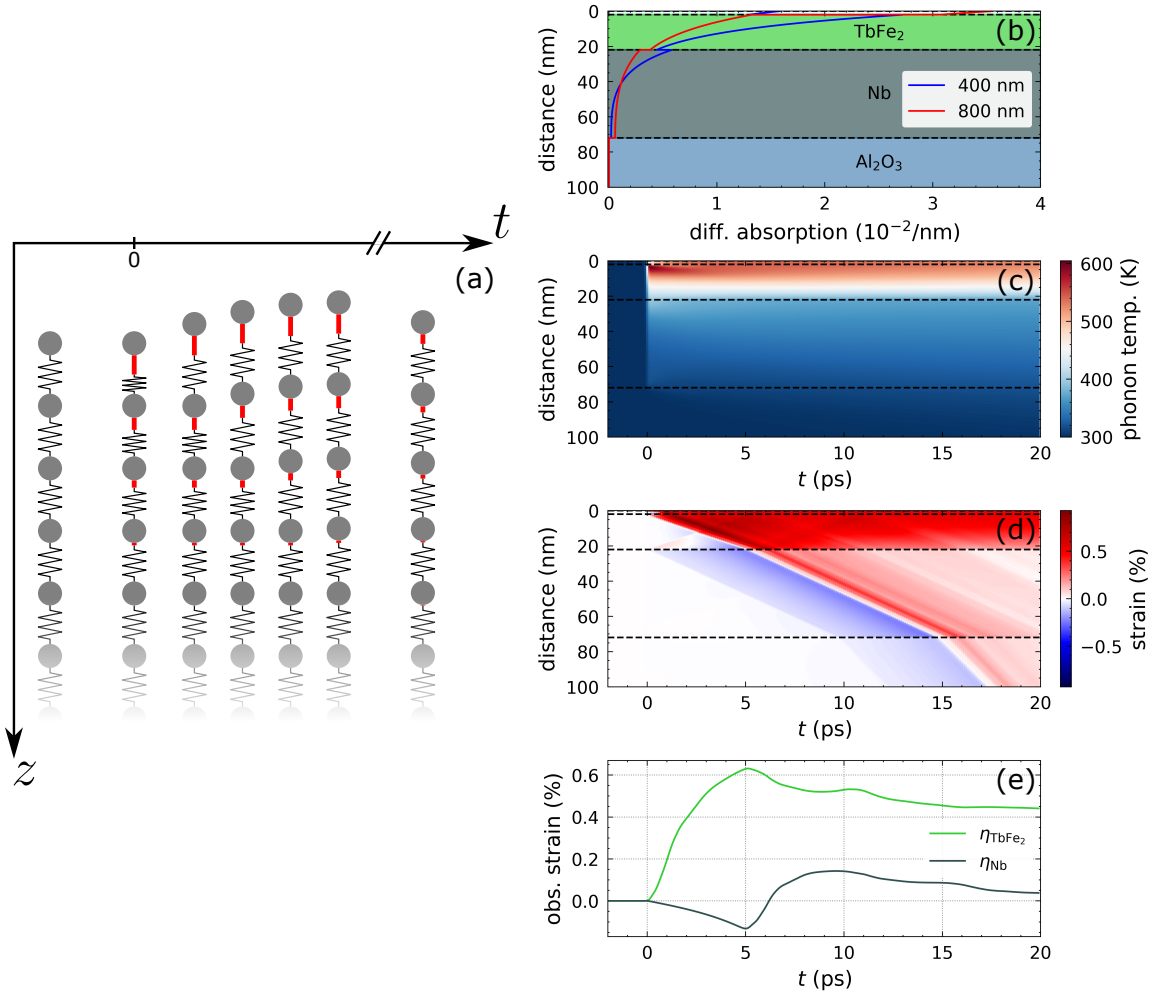

Figure 7: (a): Visualization of the masses and springs approach to calculate the strain dynamics. The absorbed energy density from the pump pulse yields a stress that is represented by red spacer sticks, and their length follows the absorption profile given in panel (b). (c): Exemplary temperature map for 20 nm $TbFe_2$ on 50 nm Nb on a sapphire substrate, showing the distribution of thermal energy in the phononic subsystem over time and space. (d): Resulting strain map, generated from the temperature map in (c). Red areas correspond to a positive strain (expansion) and blue areas to a negative strain (compression). (e): Observed strain in the $TbFe_2$ and Nb layers calculated as the weighted average of the strain map. Figure inspired by [57].

2.5 Magneto-optic theory

The theory of magneto-optics forms the foundation for understanding the experimental techniques utilized in this thesis. This section draws on concepts from the book of Fumagalli and Schoenes [13] and focuses on polarization effects that occur when light

interacts with magnetic materials. It starts with a review of fundamental polarization states of light. After an introduction to the most relevant effects and geometries, an explanation based on a birefringence for circular polarized light is provided. The last subsection discusses the origin of the circular birefringence based on a Lorentz oscillator model.

2.5.1 Overview of polarization states of light

In addition to wavelength and intensity, polarization is the third fundamental property of light. Polarization describes the orientation of the electric field vector relative to the propagation direction.
The simplest polarization state is linear polarization. Consider a wave with frequency ω traveling along the z-axis with a wave vector k. The electric field of the wave can be described as the real part of the following expression:

$$\vec{E}(z,t) = \vec{E}_0 \mathrm{e}^{\mathrm{i}(\omega t - kz)}, \tag{25}$$

where $\vec{E}_0 = E_0 \hat{e}$ represents the amplitude and polarization direction of the electric field. Since light is a transverse wave, the polarization vector $\hat{p}$ lies in a plane perpendicular to the propagation direction. Using polar coordinates, it can be written as:

$$\hat{e} = \begin{pmatrix} \cos\alpha \\ \sin\alpha \\ 0 \end{pmatrix}, \tag{26}$$

with the polarization angle α. All polarization states can be described as combinations of two orthogonal linear polarization components.
The second fundamental polarization state is circular polarized light. Here, the $\vec{E}$-field vector rotates around the the propagation direction. It is mathematically described by a superposition of two orthogonal linear polarization states with a phase shift of $\pm\pi/2$:

$$\vec{E}_{\pm}(z,t) = \frac{1}{\sqrt{2}} \left(\vec{E}_x(z,t) + \mathrm{e}^{\pm \mathrm{i}\frac{\pi}{2}} \vec{E}_y(z,t) \right). \tag{27}$$

The sign of the phase shift determines the rotation direction of the $\vec{E}$-field. When facing the light source, a clockwise rotation is called right circular polarized (RCP), as it is described by a right hand rule, and corresponds to $\vec{E}_-$ in equation (27). Conversely, a counterclockwise rotation is labeled LCP and corresponds to $\vec{E}_+$ in equation (27). The two circular polarizations also form a basis to describe all other polarization states. Circular polarization is a special case of elliptical polarization, which is described by a superposition of linear polarizations with an arbitrary phase angle and amplitude ratio.

2.5.2 Overview of magneto-optic effects

There are numerous magneto-optic effects, however this discussion is limited to the magneto-optical Faraday and Kerr effect (MOKE). Both effects are characterized by a change of the polarization state of light. Specifically, the polarization axis of initially linear polarized light is rotated by an angle θ and the light becomes elliptically polarized with an ellipticity ζ. The Faraday effect is observed in a transmission geometry, whereas the Kerr effect describes the polarization change of reflected light from a magnetic surface.
The Kerr effect is further divided into the polar Kerr effect (PMOKE), with an out-of-plane field (or magnetization) and ideally measured at normal incidence. The longitudinal Kerr effect (LMOKE) is measured at grazing incidence with the magnetization in-plane and parallel to the plane of reflection. Finally, for the transversal Kerr effect (TMOKE), the magnetization is orientated in-plane and perpendicular to the plane of reflection. Unlike PMOKE and LMOKE, TMOKE is observed as an intensity change of the reflected light rather than a polarization change. Figure 8 provides an overview of the magneto-optic effects and their geometries. The discussion here will be limited to the Faraday and polar and longitudinal Kerr effects.

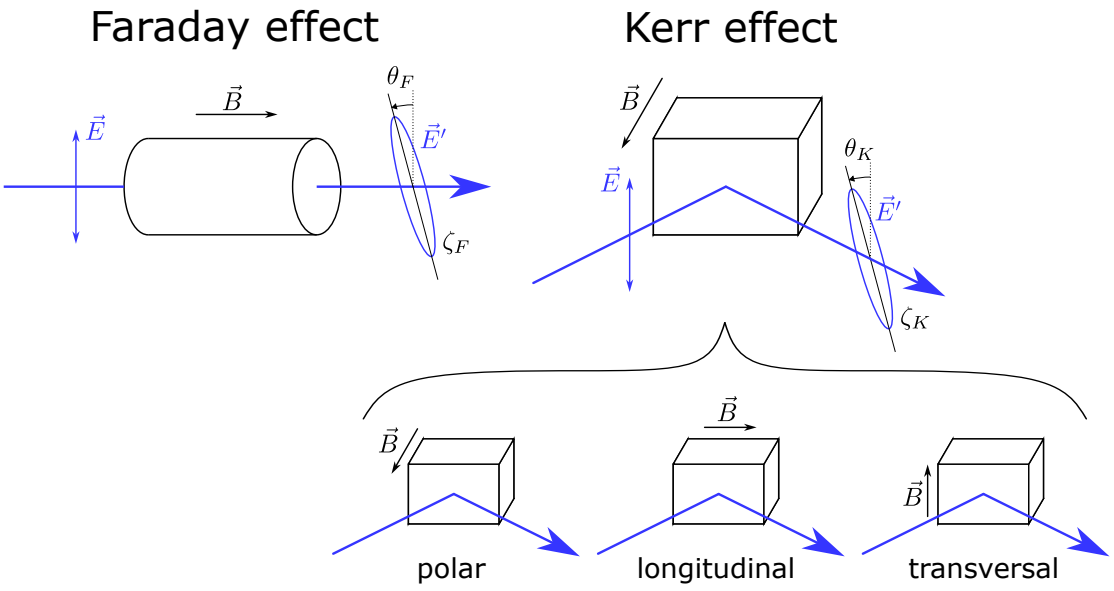

Figure 8: Overview of the different magneto-optical effects discussed here. Depending on whether a transmissive or reflective geometry is used, the effect is called Faraday or Kerr effect, respectively. The Kerr effect is further subdivided depending on the relative orientation of the plane of reflection and the magnetic field or magnetization vector. Figure adapted from [13].

2.5.3 Effects of circular birefringence

The observed polarization rotation and ellipticity change in the Faraday and Kerr effects is explained by a circular birefringence induced by an external magnetic field, local magnetization change or change of the local effective field. It is characterized by different complex refractive indices $\tilde{n} = n - \mathrm{i}\kappa \to \tilde{n}_\pm$ for LCP and RCP light. Thus it it is practical to express the incident linear polarized light in a circular basis, for example:

$$\vec{E}_x = \frac{1}{2} E_0 \left(\vec{E}_+ + \vec{E}_- \right) \tag{28}$$

$$= \frac{1}{2} E_0 \left((\hat{x} + \mathrm{i}\hat{y}) + (\hat{x} - \mathrm{i}\hat{y}) \right) \mathrm{e}^{\mathrm{i}\left(\omega t - \frac{\omega}{c}\tilde{n} z\right)}. \tag{29}$$

After propagation through a magnetized material in Faraday geometry, where the RCP and LCP components have different refractive indices, the resulting wave is:

$$\vec{E}' = \frac{1}{2} E_0 \left((\hat{x} + \mathrm{i}\hat{y}) \, \mathrm{e}^{\mathrm{i}\left(\omega t - \frac{\omega}{c}\tilde{n}_+ z\right)} + (\hat{x} - \mathrm{i}\hat{y}) \, \mathrm{e}^{\mathrm{i}\left(\omega t - \frac{\omega}{c}\tilde{n}_- z\right)} \right) \tag{30}$$

$$= \frac{1}{2} E_0 \left((\hat{x} + \mathrm{i}\hat{y}) \, \mathrm{e}^{-\mathrm{i}\frac{\omega}{c}\tilde{n}_+ z} + (\hat{x} - \mathrm{i}\hat{y}) \, \mathrm{e}^{-\mathrm{i}\frac{\omega}{c}\tilde{n}_- z} \right) \mathrm{e}^{\mathrm{i}\omega t}. \tag{31}$$

The refractive index can be rewritten with a complex phase difference $\tilde{\delta} = \delta_n + \mathrm{i}\delta_\kappa$:

$$\tilde{\delta} = \frac{\omega}{c} \left(\tilde{n}_+ - \tilde{n}_- \right) z. \tag{32}$$

Inserting into (31) gives:

$$\vec{E}' = \frac{1}{2} E_0 \left((\hat{x} + \mathrm{i}\hat{y}) \, \mathrm{e}^{-\mathrm{i}\tilde{\delta}/2} + (\hat{x} - \mathrm{i}\hat{y}) \, \mathrm{e}^{+\mathrm{i}\tilde{\delta}/2} \right) \mathrm{e}^{\mathrm{i}\left(\omega t - \frac{\omega}{c}\bar{\tilde{n}} z\right)} \tag{33}$$

$$= \frac{1}{2} E_0 \left(\hat{x} \left(\mathrm{e}^{-\mathrm{i}\tilde{\delta}/2} + \mathrm{e}^{+\mathrm{i}\tilde{\delta}/2} \right) + \mathrm{i}\hat{y} \left(\mathrm{e}^{-\mathrm{i}\tilde{\delta}/2} - \mathrm{e}^{+\mathrm{i}\tilde{\delta}/2} \right) \right) \mathrm{e}^{\mathrm{i}\left(\omega t - \frac{\omega}{c}\bar{\tilde{n}} z\right)} \tag{34}$$

$$= E_0 \left(\hat{x} \cos\left(\frac{\tilde{\delta}}{2}\right) + \hat{y} \sin\left(\frac{\tilde{\delta}}{2}\right) \right) \mathrm{e}^{\mathrm{i}\left(\omega t - \frac{\omega}{c}\bar{\tilde{n}} z\right)}. \tag{35}$$

It is apparent that the transmitted light has a rotated polarization axis by a complex angle $\tilde{\delta}/2$.
Considering a non-absorbing material, i.e. $\kappa = 0$ and $\tilde{n} = n$, the phase difference $\tilde{\delta} = \delta_r$ is also real. In this case the transmitted wave has a rotated polarization by the angle $\theta = \delta_r/2$, which depends on the magnitude of the splitting of the refractive index $n_+ - n_-$ and the propagation length z.
If the material is absorbing, i.e. $\tilde{n}$ and $\tilde{\delta}$ are both complex, the transmitted wave is

given by:

$$\vec{E}' = E_0 \left(\hat{x} \cos\left(\frac{\delta_r}{2} + \mathrm{i}\frac{\delta_\kappa}{2} \right) + \hat{y} \sin\left(\frac{\delta_r}{2} + \mathrm{i}\frac{\delta_\kappa}{2} \right) \right) \mathrm{e}^{\mathrm{i}\left(\omega t - \frac{\omega}{c}\bar{\tilde{n}} z\right)} \tag{36}$$

$$= E_0 \left(\hat{x} \left(\cos\frac{\delta_n}{2} \cos \mathrm{i}\frac{\delta_\kappa}{2} - \sin\frac{\delta_n}{2} \sin \mathrm{i}\frac{\delta_\kappa}{2} \right) \right.$$

$$\left. + \hat{y} \left(\sin\frac{\delta_n}{2} \cos \mathrm{i}\frac{\delta_\kappa}{2} - \cos\frac{\delta_n}{2} \sin \mathrm{i}\frac{\delta_\kappa}{2} \right) \right) \mathrm{e}^{\mathrm{i}\left(\omega t - \frac{\omega}{c}\bar{\tilde{n}} z\right)} \tag{37}$$

$$= E_0 \left(\hat{x} \left(\cos\frac{\delta_n}{2} \cosh\frac{\delta_\kappa}{2} - \mathrm{i} \sin\frac{\delta_n}{2} \sinh\frac{\delta_\kappa}{2} \right) \right.$$

$$\left. + \hat{y} \left(\sin\frac{\delta_n}{2} \cosh\frac{\delta_\kappa}{2} + \mathrm{i} \cos\frac{\delta_n}{2} \sinh\frac{\delta_\kappa}{2} \right) \right) \mathrm{e}^{\mathrm{i}\left(\omega t - \frac{\omega}{c}\bar{\tilde{n}} z\right)} \tag{38}$$

$$= E_0 \left(\cosh\left(\frac{\delta_\kappa}{2}\right) \left(\hat{x} \cos\frac{\delta_n}{2} + \hat{y} \sin\frac{\delta_n}{2} \right) \right.$$

$$\left. + \mathrm{i} \sinh\left(\frac{\delta_\kappa}{2}\right) \left(-\hat{x} \sin\frac{\delta_n}{2} + \hat{y} \cos\frac{\delta_n}{2} \right) \right) \mathrm{e}^{\mathrm{i}\left(\omega t - \frac{\omega}{c}\bar{\tilde{n}} z\right)}. \tag{39}$$

The last equation (39) describes an ellipse with a semi-major axis $\cosh(\delta_\kappa/2)$ and a semi-minor axis $\sinh(\delta_\kappa/2)$. The major axis is tilted by $\theta = \delta_n/2$. The ellipticity η is defined as the ratio between the major and minor axes:

$$\zeta = \frac{\cosh(\delta_\kappa/2)}{\sinh(\delta_\kappa/2)} = \tanh\left(\frac{\delta_\kappa}{2}\right). \tag{40}$$

Thus it is concluded that a difference in the real part of the refractive index n, which results in a phase difference between RCP and LCP light, gives rise to the polarization rotation θ. A difference in absorption κ leads to different amplitudes of RCP and LCP light, which causes the ellipticity change ζ. Both effects are illustrated in Figure 9. Similar principles apply to the reflective Kerr geometries.

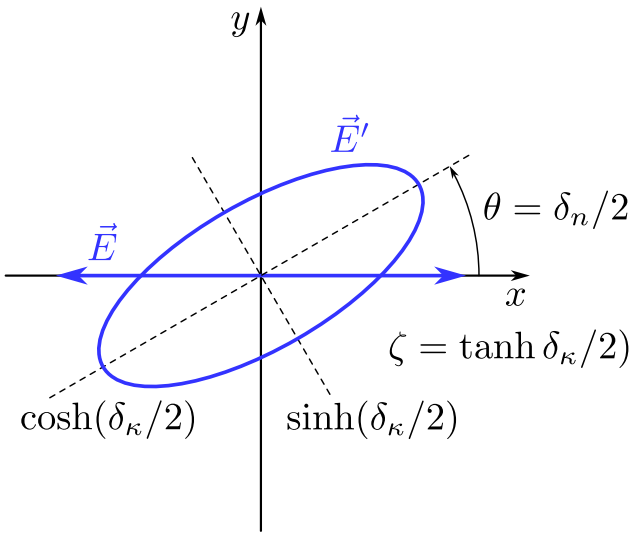

Figure 9: Geometry of the polarization state of the light before ($\vec{E}$) and after ($\vec{E}'$) transmission/reflection from a magnetic material. The polarization axis is rotated by $\theta = \delta_n/2$ and the light is elliptically polarized with an ellipticity change $\zeta = \tanh(\delta_\kappa/2)$.

2.5.4 Origin of the circular birefringence

So far no physical explanation for the existence of the magnetically induced circular birefringence has been provided. This effect can be understood by considering the effects of magnetic fields in the Lorentz oscillator model. The Lorentz oscillator is a classical model to describe the interaction of light with atoms, where the electrons are treated as a damped harmonic oscillator bound the the core. This oscillator is driven by the electric field of the light. To account for magneto-optical effects, a static magnetic field $\vec{B}$ is also included, which results in a Lorentz force on the electron. From the frequency response of the system the dielectric function $\tilde{\varepsilon} = \varepsilon_r - \mathrm{i}\varepsilon_i$ and the complex refractive index $\tilde{n} \propto \sqrt{\tilde{\varepsilon}}$ are calculated.
The equation of motion for the Lorentz oscillator is then given by:

$$\ddot{\vec{r}} + \gamma\dot{\vec{r}} + \omega_0^2\vec{r} = -\frac{e}{m_e}\left(\vec{E}_0 \mathrm{e}^{\mathrm{i}\omega t} + \dot{\vec{r}} \times \vec{B}\right), \tag{41}$$

with the damping constant γ, the resonance frequency ω_0 and the electron charge and mass e and m_e, respectively. The driving field $\vec{E}$ is linear polarized along $\vec{E}_0$.
Solving the equation yields the electron displacement $\vec{r}$, which determines the polarization of the material via

$$\vec{P} \overset{(1)}{=} \varepsilon_0 \underline{\tilde{\chi}} \vec{E} \overset{(2)}{=} n_V \vec{p} \overset{(3)}{=} -n_V e \vec{r}. \tag{42}$$

The first equation (42.1) is the definition of the polarization via the susceptibility $\underline{\tilde{\chi}}$. The second and third equations (42.2) and (42.3) define the polarization as the

dipole density, with n_V the electron density and $\vec{p}$ the electric dipole moment. The susceptibility is generally a tensor, indicated by the line under their symbols.
With the relation between the dielectric function, which is also a tensor, and the susceptibility

$$\tilde{\underline{\varepsilon}} = \underline{1} + \tilde{\underline{\chi}}, \tag{43}$$

we get:

$$-n_V e\tilde{\vec{r}}(\omega) = \varepsilon_0 \tilde{\underline{\chi}}(\omega)\,\tilde{\vec{E}}(\omega) \tag{44}$$

$$\Leftrightarrow \tilde{r}_i(\omega) = -\frac{\varepsilon_0}{n_V e}\tilde{\chi}_{ij}(\omega)\,\tilde{E}_j(\omega) \tag{45}$$

$$= -\frac{\varepsilon_0}{n_V e}\left(\tilde{\varepsilon}_{ij}(\omega) - \delta_{ij}\right)\tilde{E}_j(\omega) \tag{46}$$

$$\Leftrightarrow \tilde{\varepsilon}_{ij}(\omega) = \delta_{ij} - \frac{n_V e}{\varepsilon_0}\frac{\tilde{r}_i(\omega)}{\tilde{E}_j(\omega)}. \tag{47}$$

Note that this requires the complex displacement $\tilde{r}_i(\omega)$ in frequency space, i.e. the displacement amplitude at the frequency ω, obtained for example by Fourier transformation of $\vec{r}(t)$. The complex nature of $\tilde{r}_i$ indicates a phase shift between the driving field and the oscillation of the electron.
While there exists analytical solutions for some special cases, for example $B = 0$, using numerical methods the response to arbitrary electric and magnetic fields can be estimated. Doing this for every frequency of the driving field yields the frequency-dependent dielectric function. With a pulsed field that contains many frequencies at once, this calculation can be performed in a single step by simply dividing the Fourier transform of the displacement by the Fourier transform of the electric field.
The different entries of the dielectric tensor $\tilde{\varepsilon}_{ij}$ are calculated by analyzing the response in $i = x, y, z$ to a pulsed electric field applied in the j-direction. Results without (a) and with (b) an external magnetic field in the z-direction are compared in Figure 10. It shows a graphical representation of the dielecric tensor $\tilde{\underline{\varepsilon}}(\omega)$, where each subplot corresponds to the frequency-dependence of one component $\varepsilon_{ij}(\omega)$.

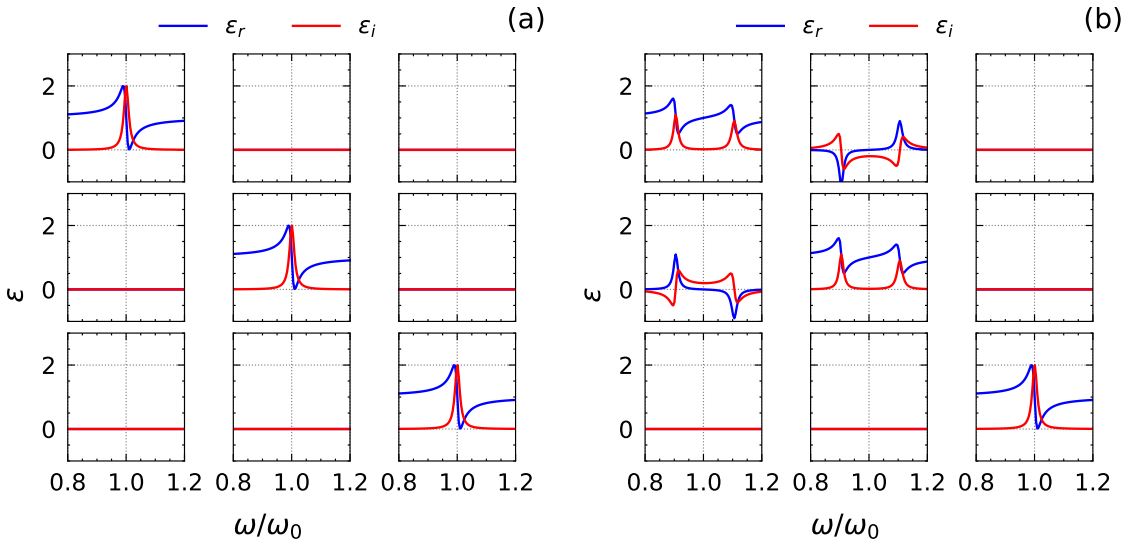

Figure 10: Dielectric tensor elements $\tilde{\varepsilon}_{ij}(\omega)$ in a cartesian (xyz) basis. (a): Without an external magnetic field, the material is isotropic, and thus the dielectric tensor is diagonal with the same diagonal elements. No birefringence is observed in this case. (b): With an external magnetic field along the z-axis, the dielectric tensor now contains non-zero off-diagonal elements which lead to a circular birefringence.

Without the magnetic field, the dielectric tensor takes a diagonal form with equal entries, so no birefringence is observed. With the magnetic field, the dielectric function splits in the $\tilde{\varepsilon}_{xx}$ and $\tilde{\varepsilon}_{yy}$ components, and the off-diagonals $\tilde{\varepsilon}_{xy} = -\tilde{\varepsilon}_{yx}$ are non-zero. In first order, this splitting is proportional to the cyclotron frequency

$$\Delta\omega = \omega_C = \frac{eB}{m_e}. \tag{48}$$

Directions parallel to the magnetic field remain unaffected, as the cross product in the Lorentz force yields 0 in this case.
The splitting of the diagonal elements and the appearance of non-zero off-diagonals corresponds to a circular birefringence, which becomes apparent when transforming $\tilde{\varepsilon}$ into a circular basis. For a circular polarization, the transformation is defined as [13]:

$$\underline{\tilde{\varepsilon}}^{\mathrm{c}} = T\underline{\tilde{\varepsilon}}T^{-1}, \tag{49}$$

with the transformation matrix T, which is obtained by expressing the the circular basis in the cartesian basis, as in (27):

$$T = \frac{1}{\sqrt{2}}\begin{pmatrix} 1 & i & 0 \\ 1 & -i & 0 \\ 0 & 0 & \sqrt{2} \end{pmatrix}. \tag{50}$$

The resulting $\tilde{\underline{\varepsilon}}^c$ now contains the dielectric functions $\tilde{\varepsilon}_\pm$ for LCP and RCP in the first two diagonal entries. Graphical representations of this transformed dielectric tensor for the same configurations as before, i.e. without a magnetic field (a) and with a magnetic field along z (b), are provided in Figure 11.

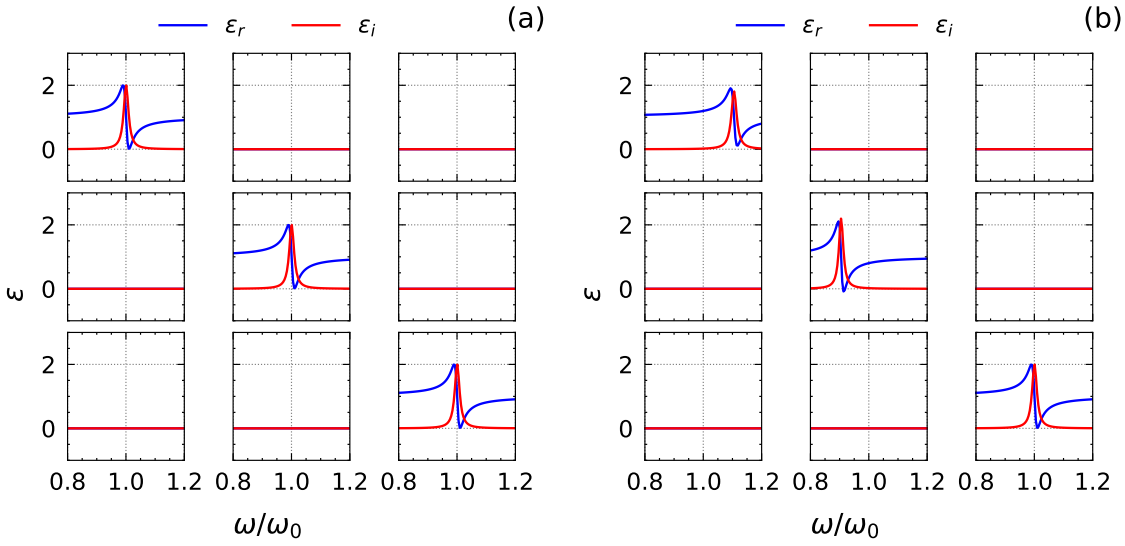

Figure 11: Dielectric tensor elements $\tilde{\varepsilon}^c_{ij}(\omega)$ in a circular basis. (a): Without an external magnetic field, the material is still isotropic, and thus no birefringence is observed again. (b): An external magnetic field results in different $\tilde{\varepsilon}_\pm$, which translates to different $\tilde{n}_\pm$, i.e. a circular birefringence.

Transformation to a circular basis does not change the shape of the dielectric tensor without the magnetic field, most importantly $\tilde{\varepsilon}_+ = \tilde{\varepsilon}_-$, so no circular birefringence occurs. With the magnetic field, a symmetric shift in $\tilde{\varepsilon}_+$ and $\tilde{\varepsilon}_-$ is observed. It becomes apparent that the double-feature in the xyz-basis (Figure 10) is caused by the equal contribution of RCP and LCP polarizations to a linear polarized wave (28). This difference in $\tilde{\varepsilon}_\pm$ leads to a difference in $\tilde{n}_\pm$, causing a magneto optic contrast in both the polarization rotation ($n_\pm$) and ellipticity change ($\kappa_\pm$). Figure 12(a) presents the frequency-dependence of the magneto-optical contrast in n, i.e. the amplitude of the polarization rotation θ. This contrast is reduced if the angle β between the $\vec{k}$-vector of the light and the $\vec{B}$-field increases. If the $\vec{B}$-field is orientated perpendicular to the $\vec{k}$-vector, no magneto-optic contrast is observed. The relative amplitude of the magneto-optical contrast decreases proportional to $\cos\beta$, as shown in panel (b), thus it is proportional to the projection of the $\vec{B}$-field onto the $\vec{k}$-vector:

$$\delta n \propto B\cos\beta \propto \vec{B}\cdot\vec{k}. \tag{51}$$

Thus, in the typical PMOKE geometry the out-of-plane component of the magnetization m_z is measured, due to the normal incidence of the probe light.

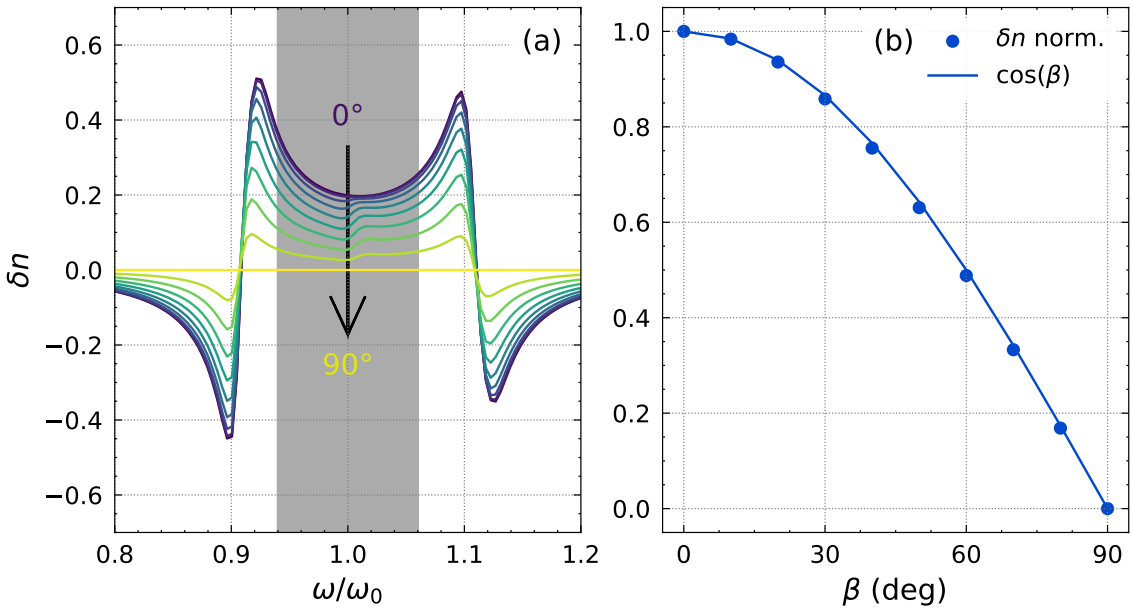

Figure 12: (a): Magneto-optic contrast in the polarization rotation θ, caused by a difference in the real part of the refractive index $\delta n = n_+ - n_-$ for different angles β between the magnetic field and the $\vec{k}$-vector of the light. Maximum contrast is achieved when $\vec{k} \parallel \vec{B}$. (b): The magneto-optic contrast reduces proportional to $\cos\beta$, so the magneto-optical signal is proportional to the projection of $\vec{B}$ onto $\vec{k}$. The data is taken by averaging δn in the gray shaded area in panel (a).

2.5.5 Element specific magneto-optics

The Lorentz oscillator model presented here is a very simplistic, yet useful model for understanding magneto-optical effects as shown in the previous subsection. However in real materials, the situation is much more complex. Typically, there are many different transitions between the energy bands, each of which corresponds to one Lorentz oscillator with a specific resonance frequency ω_0. If multiple elements are mixed, as in the $REFe_2$ compounds, each oscillator thus belongs to either the RE or the Fe. While this element specificity is most prominent in the x-ray regime (for example via x-ray magnetic circular dichroism, XMCD), it can also be achieved with all-optical methods, such as MOKE. Khorsand et al. [23] showed that by tuning the wavelength of the probe light in a trMOKE experiment on $TbFe_2$, they were either sensitive to the Tb sublattice below 610 nm and to the Fe sublattice above 610 nm. As the the two sublattices are coupled antiferromagnetically, they exhibit opposing trMOKE signals. They could also model the combined response of both sublattices by a linear superposition of the pure Tb and Fe signals. As the probe wavelength in our trMOKE setup is currently fixed at 400 nm, a strong sensitivity to the RE sublattice is expected.

3 Magneto-optical detection setups

Building on the magneto-optic theory presented in the previous chapter, this chapter describes the setups used for both static and time-resolved MOKE measurements. The discussion begins with the static MOKE setup, detailing the principles of the Kerr rotation detection using a Wollaston prism and a balanced photodiode. These principles are then extended into a pump-probe scheme, enabling ultrafast, time-resolved magnetization measurements. The different measurement modes, as well as the signal generation and processing are presented in the second part of this chapter.

3.1 Static MOKE setup

The static MOKE setup is the most basic magneto-optic experiment used for this thesis. Static MOKE experiments provide a straightforward method to measure the hysteresis loops of magnetic materials. Hysteresis parameters, such as the saturation field, can be important to understand and describe time-resolved data. A schematic of the setup is presented in Figure 13.

Electromagnet: A modified version of the commercially bought GMW Model 3480 electromagnet is used to provide variable fields up to 2200 mT. A pair of pole pieces in an extended self-built yoke focuses the magnetic field lines in the narrow gap between them. The width of this gap determines the maximum field the magnet can generate. The pole pieces are drilled in the center to allow light to enter parallel to the magnetic field, and perpendicular to the sample surface. These holes introduce minor inhomogeneities in the magnetic field, which are typically negligible.

Sample: The sample is mounted on an adjustable sample holder which allows for precise positioning and tilting inside the small gap between the pole pieces of the electromagnet. This is necessary to ensure that the reflected laser light can escape through the narrow hole in the pole piece again.

Laser: The static setup uses a continuous-wave (cw) laser, with three options available: blue (406 nm), green (544 nm) and red (633 nm), to measure magnetic hystereses at different wavelengths. Typically, the blue laser (Coherent Radius 405) with an output power of $P = 25\,\mathrm{mW}$ is preferred to match the wavelength used in the time-resolved experiments. Although the laser light should already be linearly polarized, a polarizer ensures a consistent polarization state. A set of ND-filters can be used to adjust the intensity of the laser beam as required.

Beam splitter: For polar MOKE measurements the light must strike the sample at normal incidence. This means that the reflected light returns on the same beam path

as the incident light. A beam splitter or a D-shaped half-mirror separates the reflected from the incident light. A beam splitter is easier to align, but 75% of the incident light is lost. With a D-shaped mirror the angle of incidence is not perfectly normal, so that the reflected light misses the mirror. This eliminates most losses, however it requires careful alignment and is more susceptible to instabilities. Thus, for most measurements, the beam splitter is preferred.

Detection: The Kerr rotation is detected using a Wollaston prism and a Thorlabs PDB210A/M large area balanced and amplified photodetector. The Wollaston prism splits the light into two orthogonal polarization components, with each intensity measured by one of the photodiodes. The balanced photodiode outputs the difference signal between the individual diodes. This difference signal can be tuned to zero using a $\lambda/2$-waveplate, which rotates the polarization by an arbitrary amount determined by its orientation. If the polarization of the incident light changes due to the magneto-optical Kerr effect, the intensity ratio of the two beams after the Wollaston prism also changes, resulting in a non-zero detector signal. To calibrate the photodiode, the detector signal for several rotation angles of the $\lambda/2$-waveplate is recorded. This gives a calibration curve that translates detector voltage to polarization rotation angle.

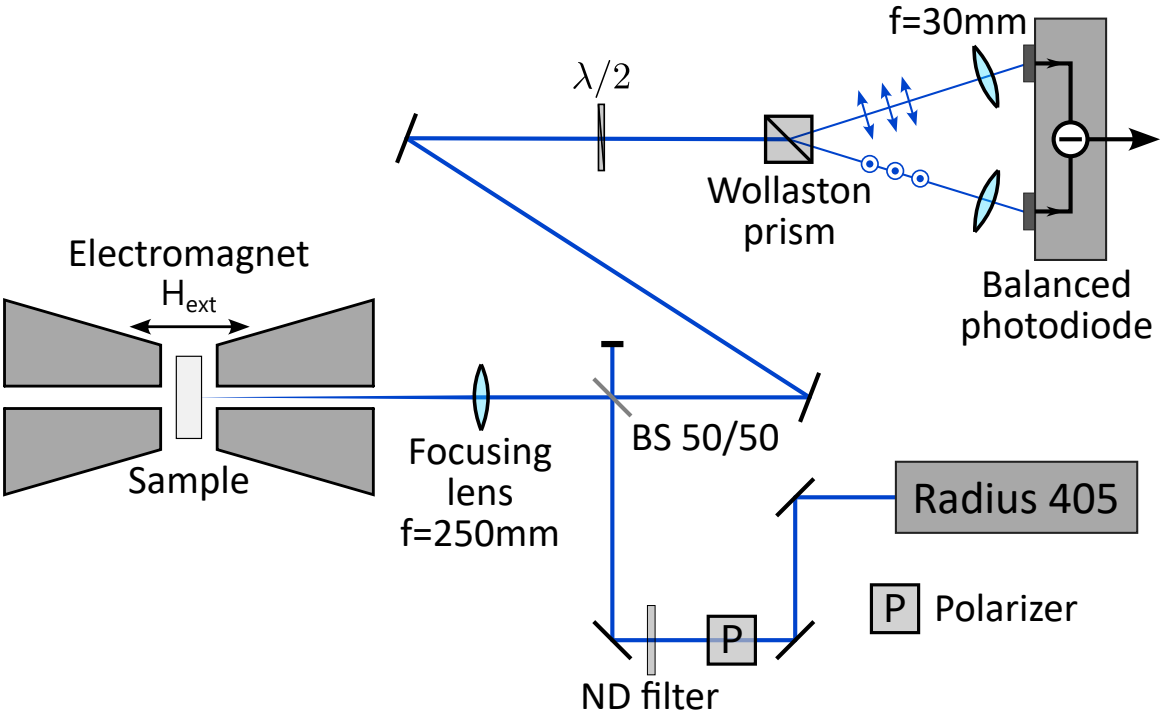

Figure 13: Sketch of the static polar MOKE setup.

3.2 Time-resolved MOKE setup

The trMOKE setup uses the same detection scheme as the static setup, but as part of a pump-probe experiment. Here, an ultrashort laser pulse (pump) excites the sample, and polar MOKE measures the magnetization using an ultrashort probe pulse at varying delays between the pump and probe. By systematically shifting this delay, the time-resolved MOKE (trMOKE) signal is recorded, achieving a temporal resolution of a few hundred femtoseconds. The magnetic field is generated either by an electromagnet, as in the static setup, or by a rotatable permanent magnet as shown in Figure 20. In addition to trMOKE, the transient reflectivity change can also be measured, offering additional insights into non-magnetic effects like electronic excitation and thermal energy transport.

3.2.1 General description of the setup

The MOKE probe detection is implemented similarly to the static setup (compare Figures 13 and 14). Instead of a cw-laser, a titanium-sapphire laser system with a wavelength of 800 nm is used. Ultrashort laser pulses are generated by the Mira oscillator, which outputs femtosecond pulses with a repetition rate of 80 MHz. A regenerative amplifier (Legend Elite) amplifies a fraction of these pulses, to an output power of 1 W at a repetition rate of 1 kHz. The light is distributed to several experiments, with about 500 mW remaining for the trMOKE setup. The pulse duration was measured via a commercial single shot autocorrelator to ≈ 150 fs.

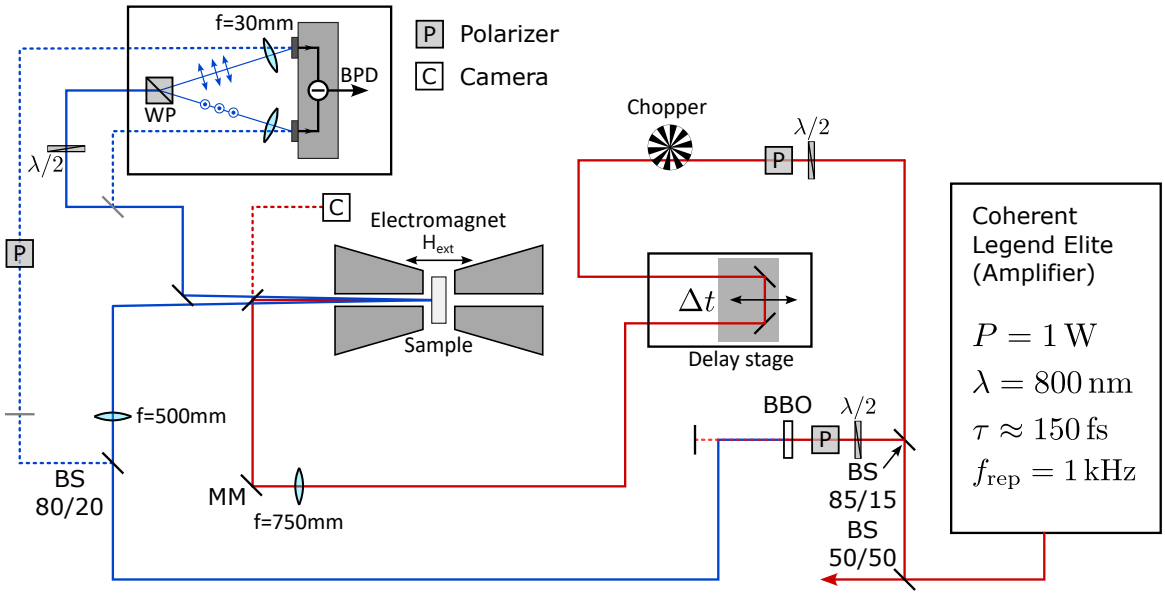

Figure 14: Simplified sketch of the time-resolved polar MOKE setup. The Wollaston prism is labeled with "WP", and the balanced photodiode with "BPD". The blue dashed beam paths are used for transient reflectivity measurements.

The probe beam is separated from the pump using a beam splitter, with 15% of the light being used for the probe. A Beta Barium Borate (BBO) crystal converts the 800 nm fundamental to 400 nm via second harmonic generation (SHG). The probe intensity is controlled by a combination of $\lambda/2$-waveplate and polarizer. The beam then passes through another beam splitter, which extracts a portion as a reference signal for transient reflectivity measurements. For trMOKE experiments, this reference beam path is blocked. The remaining probe beam is focused onto the sample at almost normal incidence, for a polar MOKE geometry. A third beam splitter directs the reflected light towards the detection setup, which is nearly identical to the static MOKE detection. For reflectivity measurements, a flip mirror redirects the probe before it reaches the $\lambda/2$-waveplate. This way, in transient reflectivity mode the upper diode measures the reference and the lower diode the reflected beam.
The pump intensity is adjusted with a motorized $\lambda/2$-waveplate and a polarizer to perform automatic fluence-dependent measurements. The pump beam is then chopped at half the repetition rate (500 Hz), to allow comparison between pumped and unpumped signals. The pump-probe-delay is set by a delay stage with a travel range of 15 cm, providing approximately 1 ns time span. For experiments with longer delays, an 8 ns stage is used. The pump beam is then focused by a lens and directed towards the sample, parallel to the probe beam, with a dichroic mirror, which is highly reflective for 800 nm and highly transmissive at 400 nm. This ensures that the probe is transmitted, while the pump is almost completely reflected towards the sample. A small fraction of the pump light passes through the mirror and is detected by a camera, positioned at the same distance as the sample. Combined with the mobile mirror (MM), this allows maintaining a constant pump position throughout an experiment, by compensating for any movement on the camera image with the mobile mirror.

3.2.2 Setup characterization

Calibrating the laser excitation fluence and field strength is essential for fluence- and field-dependent measurements. It is also important for comparison with reported results from other experimental setups in the literature, and between measurements with changed beam profiles or pole piece distances.

Fluence calibration: Fluence, defined as the pulse energy per area, is given by:

$$F = \frac{E}{A}, \tag{52}$$

where E is the pulse energy and A the area of the pump spot. The pulse energy calculated as:

$$E = \frac{P}{f_{\mathrm{rep}}}, \tag{53}$$

with the averaged power P and $f_{\mathrm{rep}} = 500\,\mathrm{Hz}$ the repetition rate of the chopped pump beam. The laser power is measured with with a thermopile head of a commercial

powermeter (Newport Power Meter Model 843-R-USB with thermopile head 919P-010-16 with 1mW noise). The area of the pump spot is calculated from a beam profiler image, taken with a camera at the sample position. Using a top-hat approximation, the fluence is then calculated as:

$$F = \frac{4 \ln 2}{\pi} \frac{P}{f_{\mathrm{rep}} x_{\mathrm{FWHM}} y_{\mathrm{FWHM}}}, \tag{54}$$

where x_{FWHM} and y_{FWHM} are the full-width at half-maximum beam diameters along the horizontal and vertical axes, respectively.
The fluence calibration has to be repeated whenever the pump path is changed. Three different beam profiles were recorded in December 2023, May 2024 and July 2024, as shown in Figure 15(a-c). It can be seen from these images, that the shape of the pump gradually deteriorated over time. Especially for the later measurements, the approximation with a Gaussian or a top-hat profile is not valid anymore, so the calculated fluence values only serve as approximate guidelines. This is is sufficient for the most experiments, as the focus lies on general trends rather than precise fluence dependencies. The size remained almost constant at $600 \times 600\,\mu\mathrm{m}$. The profile of the probe beam is shown for comparison in panel (d), with a much better shape and approximately six times smaller diameter ($70 \times 100\,\mu\mathrm{m}$).

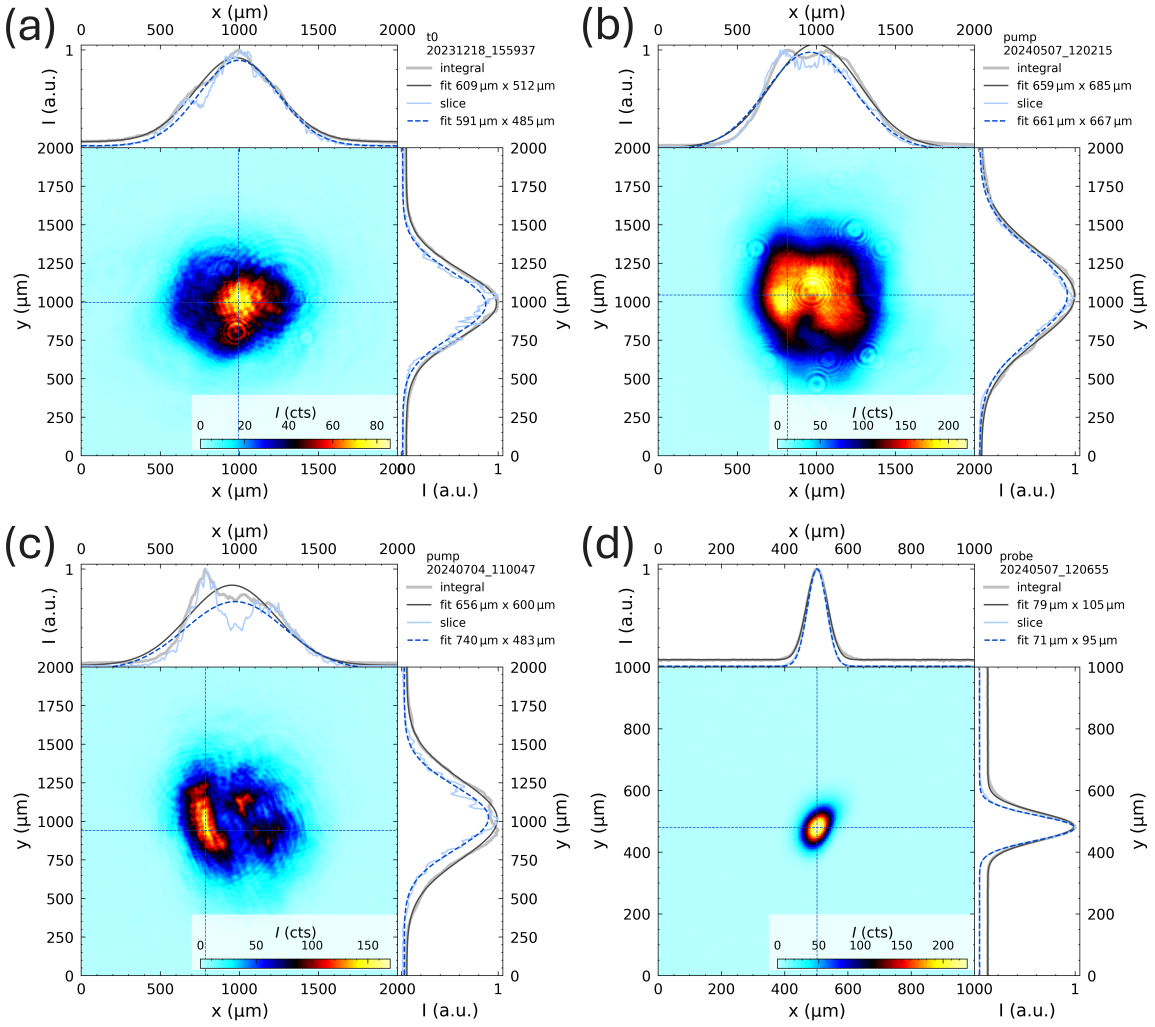

Figure 15: Pump beam profiles at different dates, showing the gradual deterioration over time (a-c). The probe beam profile (d) is shown for comparison. Note that the image of the probe beam is scaled twice as much as the pump images.

Field calibration: To convert the electromagnet current to the magnetic field strength, a commercial Hall effect sensor is placed between the pole pieces. The generated magnetic field is recorded for each current setting, producing a calibration curve like in Figure 16. The magnetic field strength in the time-resolved setup is limited to $\approx 1400\,\mathrm{mT}$, depending on the pole piece separation. Therefore, the calibration must be repeated every time the pole pieces are moved. The magnet exhibits a small hysteresis due to the nonzero remanent magnetization of the steel pole pieces, resulting in a residual magnetic field even with no applied current. The sign of the magnetic field signal also depends on the orientation of the Hall sensor.

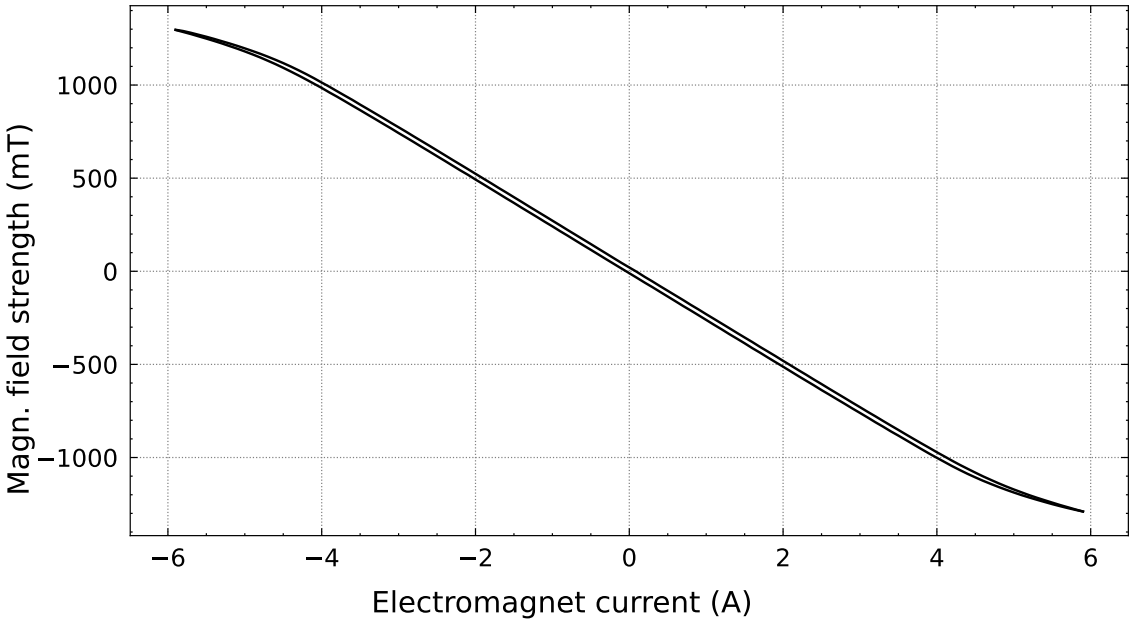

Figure 16: Exemplary calibration curve for the commercial electromagnet GMW 3470 with a bipolar powersupply Kepco BOP 36-6, used in the trMOKE setup.

3.2.3 Signal generation for trMOKE

Figure 18 illustrates the typical signal processing routine for a trMOKE experiment. At a specific external magnetic field, for each time delay, the pumped and the unpumped signals are recorded by measuring the balanced diode signal when the chopper is open or closed, respectively. This is indicated as the gray and white areas in Figure 17. This detector signal is integrated and amplified by a Stanford Instruments boxcar integrator over the gate interval, as shown in the inset plot. This creates a step-like signal, which is read by a National Instruments PCIe-6251 measurement card at regular intervals, indicated by the dashed vertical lines.

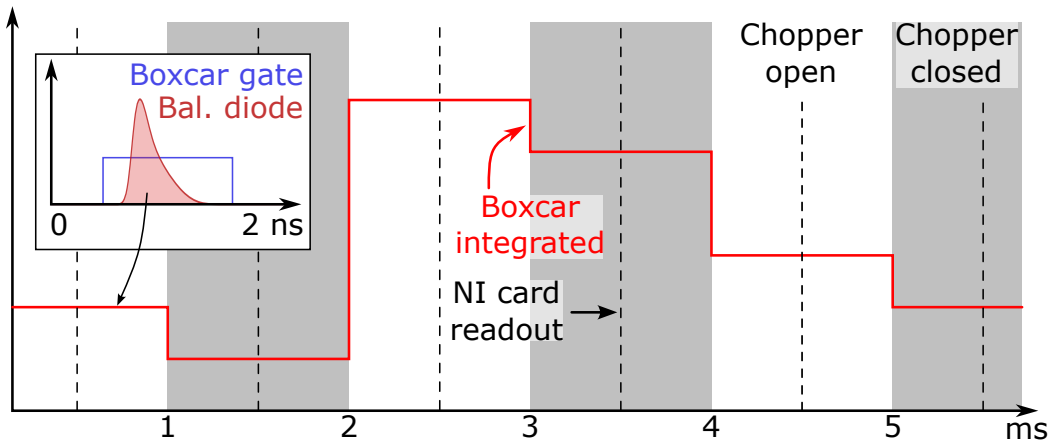

Figure 17: Sketch of the signal acquisition via the boxcar integrators.

The resulting curves for the pumped and unpumped signals are presented in Figure 18(a). This process is repeated for the opposing magnetic field to generate the curves in Figure 18(b). Shot-to-shot comparison between pumped and unpumped signals minimizes noise, improving signal quality.
To further increase the signal-to-noise ratio, the measurement is repeated over a user-specified number of loops. Data for "field up" and "field down" is averaged across loops, yielding much smoother curves, as presented in Figure 18(c). Additionally, because the setup sometimes produces outlier data points, a sigma-clipping routine is applied to remove these artifacts. For each time delay, the signals from all loops are compared: any value falling outside the interval $\pm\kappa\sigma$ around the mean is rejected. The parameter κ defines the width of this interval, given in units of the standard deviation σ. The width has to be adjusted manually, as a too high value κ allows outliers to persist, while a too low value risks removing valid data, increasing the noise. This is repeated until all values remain within the interval.
To isolate the field-dependent polarization rotation, i.e. the trMOKE signal, the difference between field up and field down is calculated. If measured at the saturation field $\pm B_{\mathrm{sat}}$, this difference corresponds to the total amplitude of the magnetic hysteresis. The sum signal, i.e. the field-independent polarization rotation, contains all non-magnetic birefringence contributions, some of which are explored in the following chapter. Both the field-dependent and field independent polarization rotation are shown in Figure 18(d). More details on the signal processing routines and the measurement software are found in the PhD thesis by Willig [60].

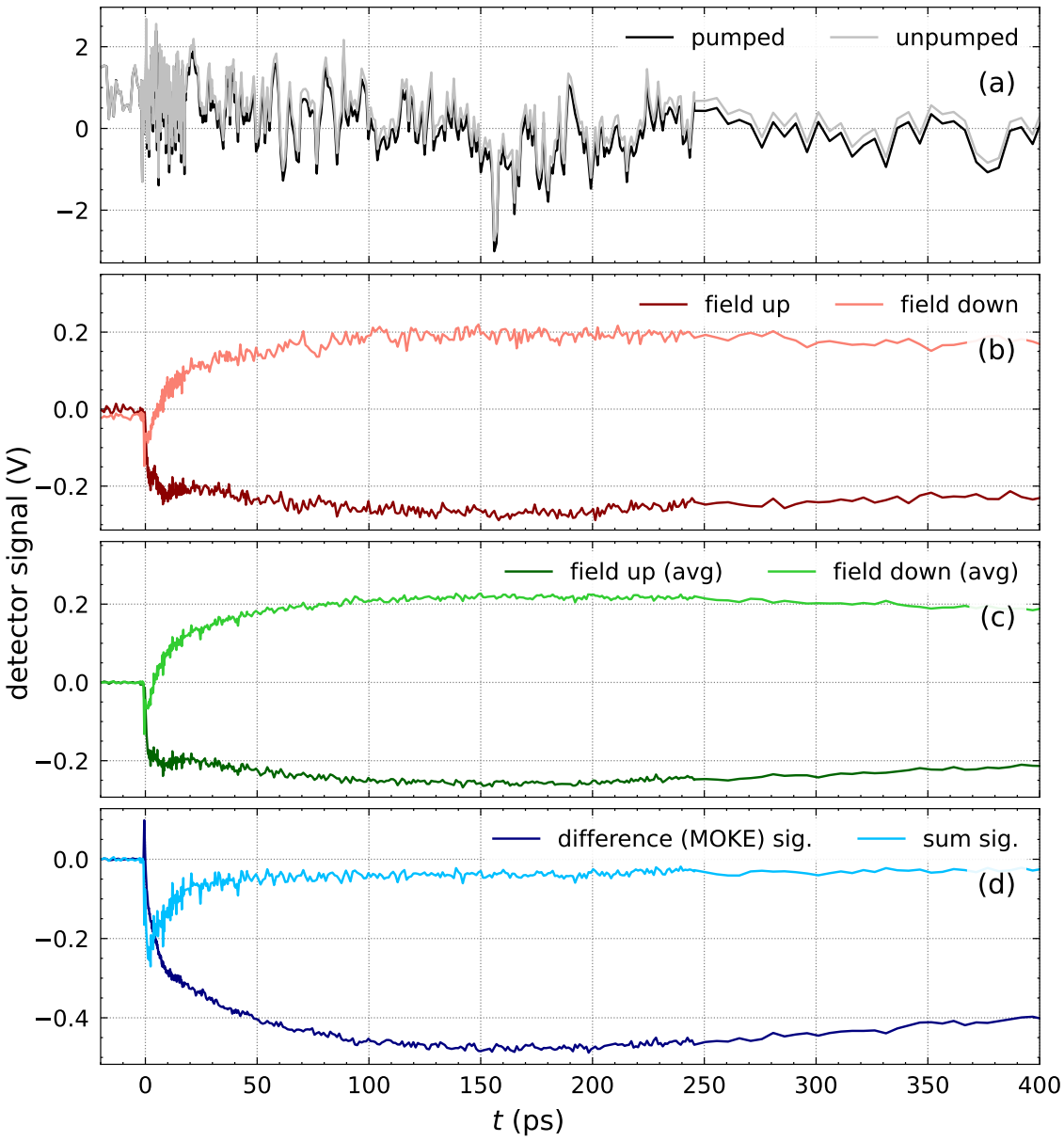

Figure 18: Overview of the main signal processing steps. The pumped and unpumped signals (a) are measured for opposing field directions (b) and averages over several loops with outlier rejection (c). Subtracting or adding the field up and field down signal generates the MOKE and field-independent polarization rotation signals (d).

3.2.4 Origins of non-magnetic contributions to the polarization rotation

As shown in Figure 18(d), a significant field-independent polarization rotation is observed in the measurements. These signals result from a temporary birefringence induced by the pump excitation. A key contributor is the rotational alignment of air molecules in the pump-probe overlap region in front of the sample. The intense electric field of the focused pump pulse aligns the molecular dipole moments. When the probe beam overlaps significantly with the pump beam in the air, as is common in frontside-excitation polar MOKE geometry, this temporary birefringence of air is detected as distinct, sharp features in the field-independent polarization rotation signal.
The short laser pulse ($\tau \approx 150\,\mathrm{fs}$) acts as an impulsive excitation, and the molecules continue rotating afterwards. With a characteristic revival time, they realign periodically, generating repeating signals in the field-independent polarization rotation. In Figure 19, some features from N_2 and O_2 molecules are identified, with revival periods of $\tau_R = 8.4\,\mathrm{ps}$ (i.e. $\tau_R/4$, $\tau_R/2$ and τ_R) and $\tau_R = 11.6\,\mathrm{ps}$ (i.e. $\tau_R/4$) respectively [33, 62]. As magnetic-field-independent signals, they do not appear in the trMOKE signal, but the sharp, prominent features significantly contribute to the field-independent polarization rotation. Notably, these contributions remain detectable even after 100 ps and provide a seemingly large "noise" on the field-independent polarization rotation. However they do not affect the time-resolved reflectivity change.

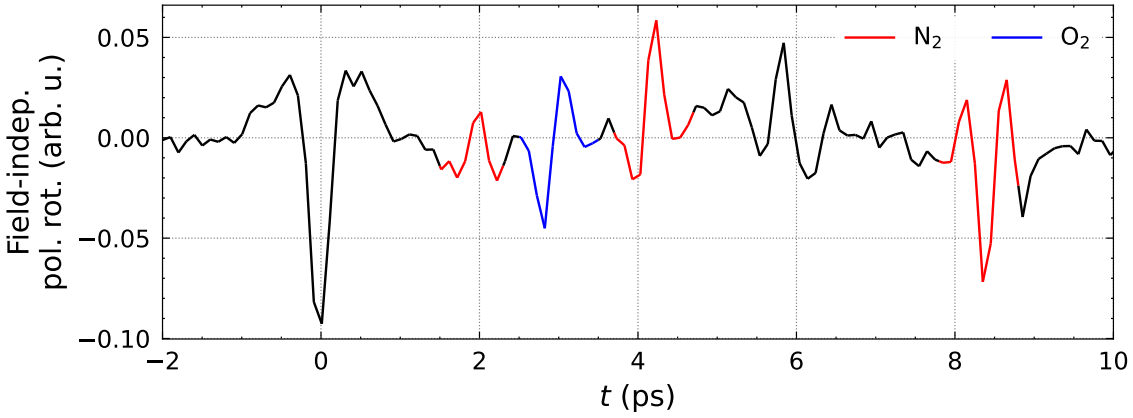

Figure 19: Rotational alignment of air molecules (N_2, O_2) in the first 10 ps following the laser excitation, observed in the field-independent polarization rotation signal.

3.2.5 Alternative measurement modes

Rotatable permanent magnet: For field-angle dependent measurements, the electromagnet is replaced by a NdFeB permanent magnet mounted on a rotation stage, allowing for tilting the external field relative to the sample surface, as sketched in Figure 20. However, the field strength at the probe spot location is limited to $\approx 400\,\mathrm{mT}$, depending on the distance to the magnet surface, in any case well below the saturation field for all samples. Another difficulty with this setup is to extract the field-dependent MOKE signals from the non-magnetic polarization rotation contributions, as the field cannot be inverted by reversing the current through the coils anymore. Thus, non-magnetic contributions to the polarization rotation, such as rotational alignment of air molecules, show up prominently in these signals. Instead of subtracting field up and field down, opposing field angle pairs where the field angle differs by 180° can be subtracted to extract the field-dependent MOKE signal. This requires a long-term stable laser alignment, as opposing angles are not measured consecutively for each loop. Any drift in the laser alignment over time diminishes the accuracy of the signal subtraction. Additionally, precise alignment of the permanent magnet with the sample surface and the probe beam is essential for a reliable interpretation of the field angle.

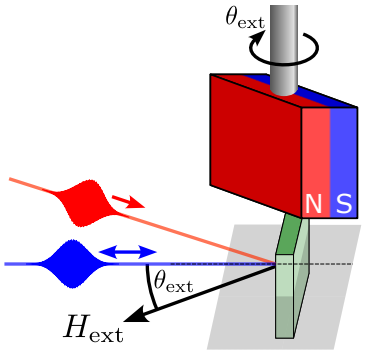

Figure 20: The rotatable permanent magnet setup.

Transient reflectivity: Another measurement mode is the transient reflectivity. It is usually measured without an external magnetic field, though some measurements were performed with an out-of-plane field, where a transversal MOKE signal was observed. The beam paths for reflectivity experiments are indicated as dashed blue lines in Figure 14. One diode of the balanced photodetector measures a reference beam, extracted from the probe before it interacts with the sample. The other beam is reflected from the sample surface and detected by the other diode. By comparing the intensity of the reflected beam to a reference beam, noise due to intensity fluctuations of the laser is effectively removed. A polarizer in the reference beam controls its intensity, and the detector signal is balanced before each measurement. This serves a similar function to the $\lambda/2$-waveplate in the trMOKE measurements. As the reflectivity is field-independent, the resulting curves for "field up" and "field down" must be added, contrary to trMOKE measurements where the difference signal is needed. Apart from that, the data processing routine is identical.

4 Sample characterization

This section introduces the rare-earth iron ($REFe_2$) samples used in the experiments. Following a general introduction to the samples and their structure, their static magnetic hystereses are analyzed to provide insight about important magnetic parameters, especially the saturation field. Finally, static x-ray diffraction data is presented and compared across the different specimen to eludicate differences and similarities in their crystalline structure.

4.1 Sample structure and general information

All samples were grown in the group of Karine Dumesnil at the Institut Jean Lamour (Nancy, France) using molecular beam epitaxy (MBE). The samples fall into two main categories: thin films with a $REFe_2$ thickness of $20 - 40\,\mathrm{nm}$ and thick films with a $REFe_2$ layer exceeding 335 nm. In each sample, the magnetic film is grown on a 50 nm niobium (Nb) layer, which is deposited on an Al_2O_3 (sapphire) substrate. The Nb buffer layer reduces the lattice mismatch to the sapphire substrate. The $REFe_2$ and Nb films are grown so that the (110)-direction of the cubic unit cell is perpendicular to the sample surface, as illustrated in Figure 21(a-c). The hexagonal sapphire substrate has a $(11\bar{2}0)$ orientation. Each sample is covered by a capping layer of varying thickness and composition, which provides protection, and in some cases, serves as a delay line for propagating strain pulses. The values for the layer thicknesses are adjusted in the udkm1dsim toolbox to provide the best agreement between simulations and trMOKE experiments. Figure 21 presents schematic structures of the samples with the resulting thicknesses.

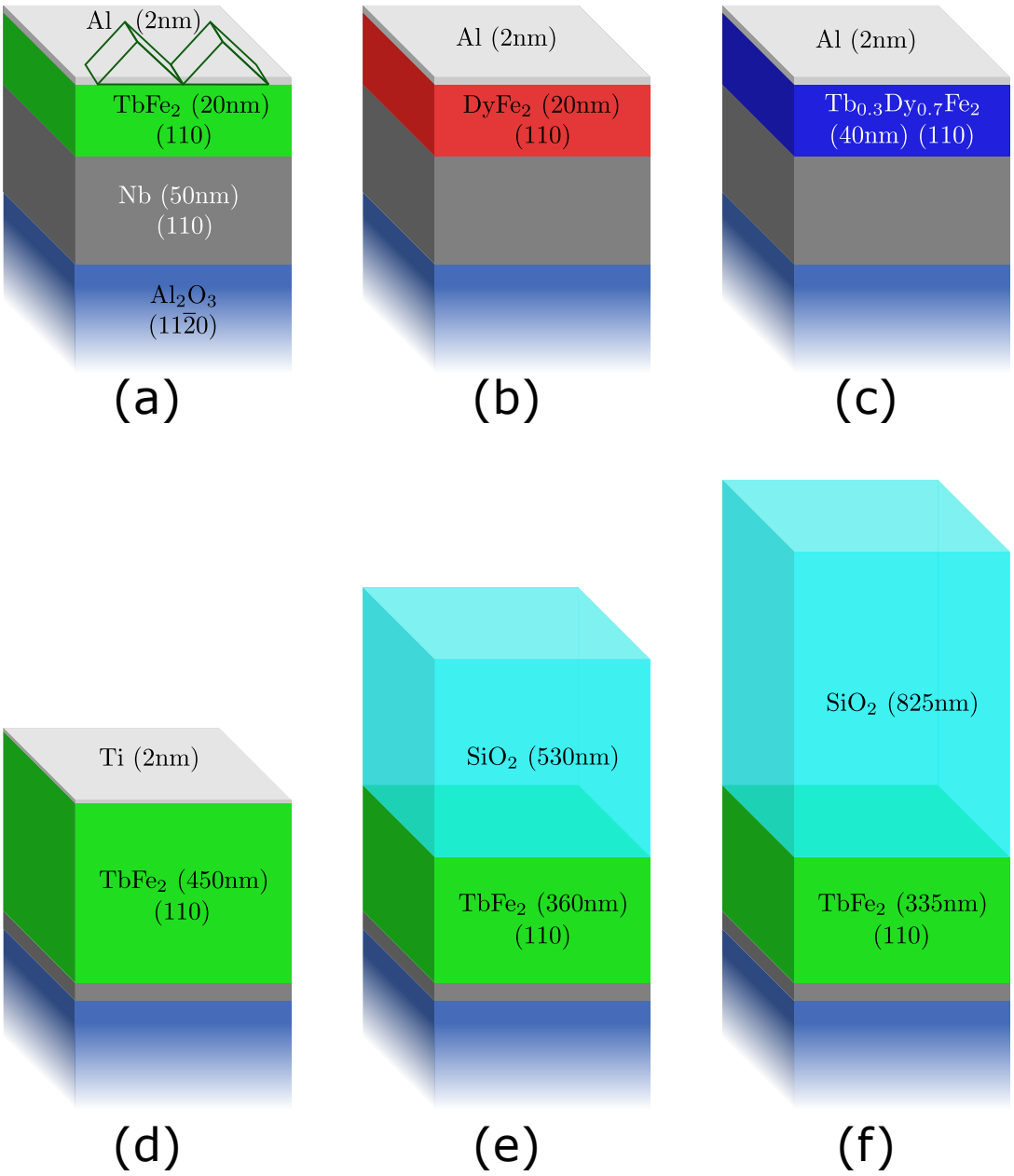

Figure 21: Schematic sketch of the different sample structures used in the experiments. Panels (a-c) show the structure of the thin $REFe_2$ films, while panels (d-f) show the composition of the thick $TbFe_2$ samples. All samples are grown on identical sapphire substrates and Nb buffer layers. Note that only the last 3 structures are drawn to scale. The orientation of cubic unit cell of the $REFe_2$, with the (110)-direction perpendicular to the sample surface, is also sketched in the first panel (a).

A list of important thermophysical parameters used for simulations and data analysis

is provided in Table 2. Figure 22 displays the differential absorption profile for 800 nm (pump) and 400 nm (probe) in the thin and thick $TbFe_2$ sample. While thin thin films are almost homogeneously excited and probed, only the surface layer is accessible for all-optical experiments in thick samples.

Table 2: List of material parameters. The sound velocity in SiO_2 (marked with *) was determined using time-domain Brillouin scattering experiments (Section 5.2.4). This value is significantly lower than the literature value $v = 5.9\,\mathrm{nm/ps}$ [46], but can be explained by inhomogeneous layer growth. The acoustic impedance is calculated by $Z = \rho v$.

	$TbFe_2$	SiO_2	Nb	Al_2O_3	Ti
out-of-plane lat. const. c $\left(\text{Å}\right)$	10.42 (110) [9]	—	4.66 (110) [16]	4.75 $\left(11\bar{2}0\right)$ [10]	—
density ρ $\left(\frac{\mathrm{kg}}{\mathrm{m}^3}\right)$	9170 [6]	2200 [46]	8580 [63]	3980 [3]	4507 [61]
sound vel. v $\left(\frac{\mathrm{nm}}{\mathrm{ps}}\right)$	3.94 [8]	5.35*	5.16 [63]	11.2 [3]	6.07 [30]
ac. imped. Z $\left(\frac{10^6\,\mathrm{kg}}{\mathrm{m}^2\,\mathrm{s}}\right)$	36.1	11.8	44.3	44.6	27.4
heat cap. C_p $\left(\frac{\mathrm{J}}{\mathrm{kg\,K}}\right)$	330 [14]	725 [1]	260 [16]	790 [3]	530 [61]
linear thermal exp. ζ $\left(\frac{10^{-6}}{\mathrm{K}}\right)$	23.7 [65]	0.49 [17]	6.89 [16]	5.38 [18]	8.6 [61]
thermal cond. κ $\left(\frac{\mathrm{W}}{\mathrm{m\,K}}\right)$	5 [64]	1.34 [1]	53.3 [16]	40 [3]	21.9 [61]
refractive index $\tilde{n}$ @800 nm	2.24 +4.47i [26]	1.45 +0.00i [31]	2.33 +3.24i [59]	1.76 +0.00i [32]	2.47 +2.53i [39]
refractive index $\tilde{n}$ @400 nm	1.76 +2.84i [26]	1.47 +0.00i [31]	2.53 +2.61i [59]	1.79 +0.00i [32]	2.09 +2.96i [39]

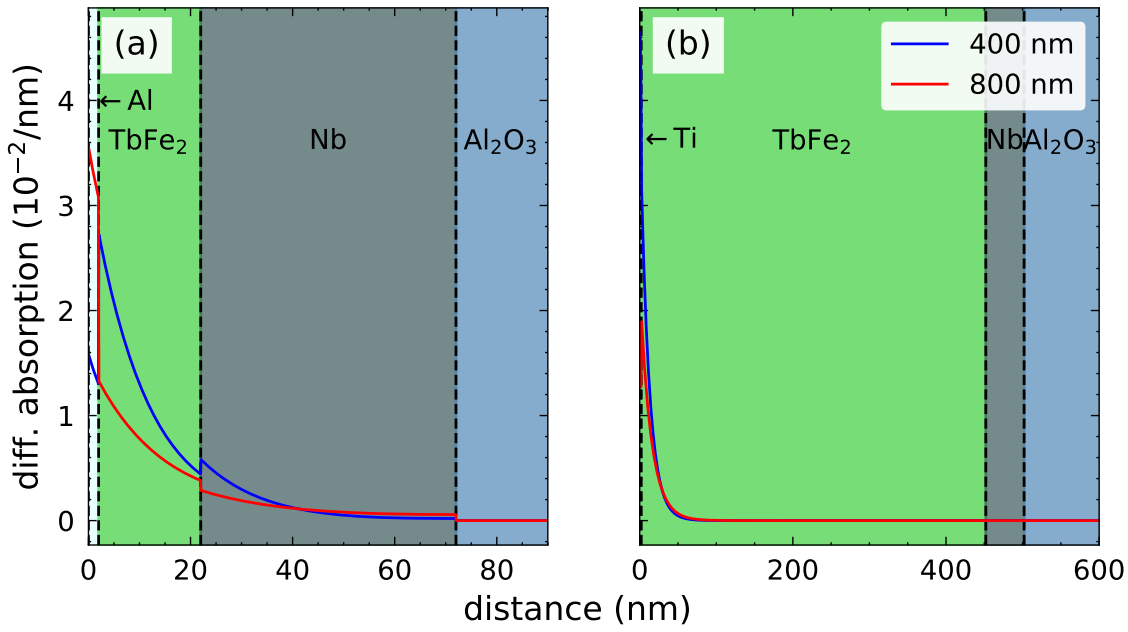

Figure 22: Differential absorption profiles for thin (a) and thick (b) $TbFe_2$ at 400 nm and 800 nm, calculated with the udkm1dsim toolbox using a multilayer approach [28]. Only the thin films are pumped and probed homogeneously, while for the thick films, only the near surface region is accessible to all-optical pumping and probing.

4.2 Simulations of the static free energy surfaces

As introduced in the section 2.2, the effective field H_{eff} and the free energy F are important quantities for describing the quasi static and dynamic evolution of the magnetization orientation of a magnetic material. The free energy in our case is a superposition of a Zeeman energy term, the shape anisotropy and the cubic magnetocrystalline anisotropy:

$$\begin{aligned} F =& F_{\text{Z}} + F_{\text{S}} + F_{\text{ani}} && (55)\\ =& -\mu_0 M_S \vec{m} \cdot \vec{H}_{\text{ext}} && (56)\\ &+ \frac{\mu_0}{2} M_S^2 m_z^2 && (57)\\ &+ K_1 \left(\mathfrak{m}_x^2\mathfrak{m}_y^2 + \mathfrak{m}_x^2\mathfrak{m}_z^2 + \mathfrak{m}_y^2\mathfrak{m}_z^2\right) + K_2 \left(\mathfrak{m}_x^2\mathfrak{m}_y^2\mathfrak{m}_z^2\right) && (58) \end{aligned}$$

Two variables are used to represent the magnetization in different coordinate systems, m in the "external frame" and $\mathfrak{m}$ in the crystallographic frame. The external frame is aligned so that the z-axis is perpendicular to the sample surface, while the crystallographic frame is aligned to the crystallographic axes, which are tilted due to the (110)-orientation. A rotation matrix describes the transformation between the two

coordinate systems. The transformation can be understood by a clockwise rotation around x by 90° and z by 45°:

$$\vec{\mathfrak{m}} = \underbrace{\begin{pmatrix} \cos(-45°) & -\sin(-45°) & 0 \\ \sin(-45°) & \cos(-45°) & 0 \\ 0 & 0 & 1 \end{pmatrix}}_{R_z(-45°)} \underbrace{\begin{pmatrix} 1 & 0 & 0 \\ 0 & \cos(-90°) & -\sin(-90°) \\ 0 & \sin(-90°) & \cos(-90°) \end{pmatrix}}_{R_x(-90°)} \vec{m} \tag{59}$$

$$= \begin{pmatrix} \frac{1}{\sqrt{2}} & 0 & \frac{1}{\sqrt{2}} \\ -\frac{1}{\sqrt{2}} & 0 & \frac{1}{\sqrt{2}} \\ 0 & -1 & 0 \end{pmatrix} \vec{m} \tag{60}$$

Calculating the free energy for each orientation of the magnetization yields a free energy surface. It can be used to find the equilibrium position of the magnetization under arbitrary external fields. This allows to estimate the saturation field and the precession frequency via the Smit-Beljers-formalism [5]. Figure 23 shows the angle-dependent free energy surfaces, generated using the magnetic parameters from Table 3, both as a 3d-surface and a 2d-colorplot. The large magnetocrystalline anisotropy in $TbFe_2$ and $DyFe_2$ results in complex free energy surfaces, while for Terfenol-D it can be almost completely described by the shape anisotropy. Note that the shape of the free energy surface of $TbFe_2$ and $DyFe_2$ appears inverted due to the opposing signs of the cubic anisotropy constants. Generally, the magnetization favors an in-plane orientation because of the shape anisotropy, but high magnetocrystalline anisotropies can also produce two additional metastable out-of-plane minima.

Table 3: Magnetic parameters of the various $REFe_2$ samples

	$TbFe_2$	$DyFe_2$	$Tb_{0.3}Dy_{0.7}Fe_2$
saturation magnetization M_S $\left(\frac{\mathrm{MA}}{\mathrm{m}}\right)$ [6]	0.80	0.80	0.80 [47]
cubic anisotropy const. K_1 $\left(\frac{\mathrm{MJ}}{\mathrm{m}^3}\right)$ [38]	−12.70	4.20	−0.66
cubic anisotropy const. K_2 $\left(\frac{\mathrm{MJ}}{\mathrm{m}^3}\right)$ [38]	2.08	−0.40	0.34
magnetoelastic const. b_2 $\left(\frac{\mathrm{MJ}}{\mathrm{m}^3}\right)$ [38]	−370	−180	−237
magnetostrictive param. $\frac{3}{2}\lambda_S$ (10^{-6}) [19]	2630	650	1640 [22]
Curie temperature T_C (°C) [19]	431	362	380 [47]

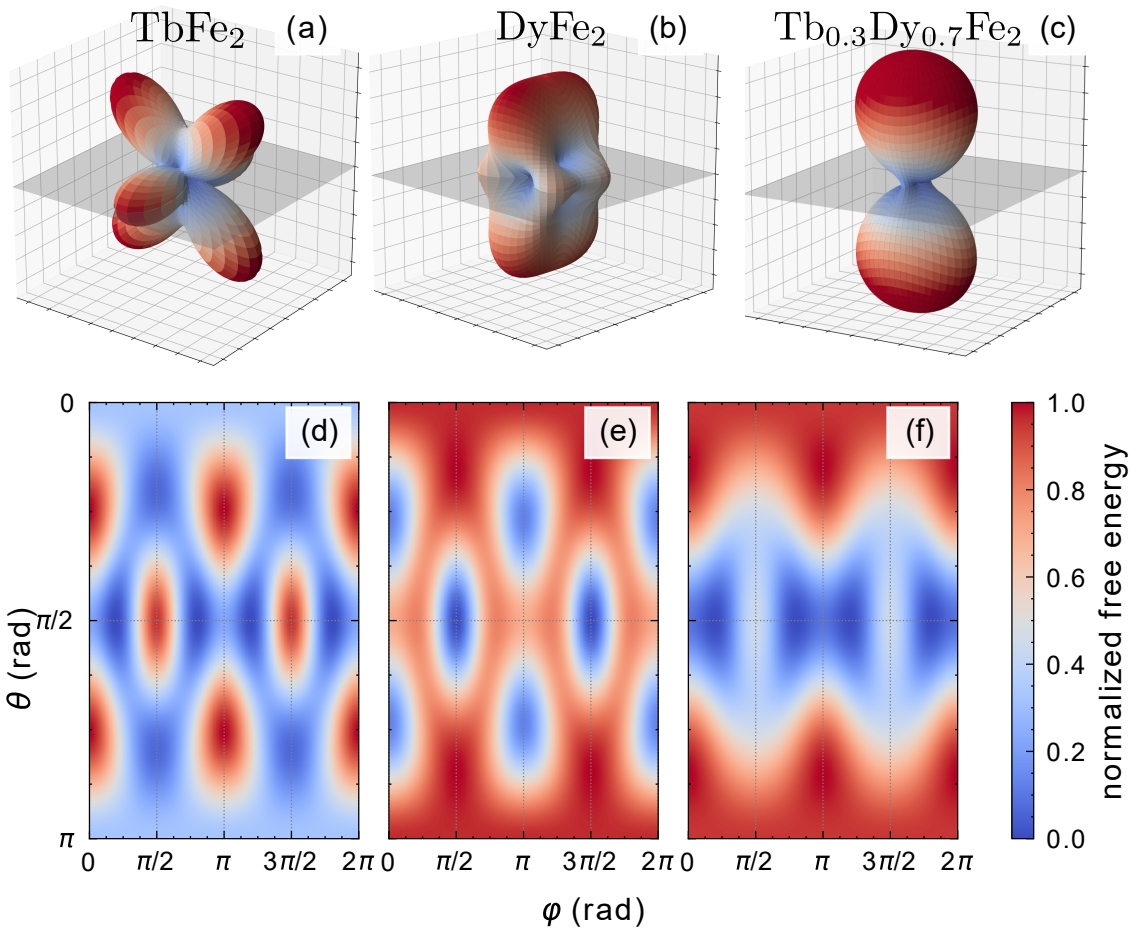

Figure 23: Calculated free energy surfaces for all three $REFe_2$ materials in absence of an external field. In panels (a-c), the distance to the coordinate origin (0,0,0) encodes the normalized free energy for every magnetization direction. This is further indicated by the color at each point. The gray plane represents the orientation of the sample surface. Panels (d-f) show a map-like 2d-projection with the same colormap as above. The inverse shape of the $TbFe_2$ (a, d) and $DyFe_2$ (b, e) anisotropy surfaces is clearly visible. Note that the amplitude of each surface is normalized, so the amplitudes are not comparable across the three panels. While $TbFe_2$ and $DyFe_2$ exhibit a complex shape due to the large contribution from the magnetocrystalline anisotropy, the free energy in $Tb_{0.3}Dy_{0.7}Fe_2$ (c, f) is dominated by the shape anisotropy which results in a dumbbell-like shape. In general the magnetic easy axes that originate from the minima of the free energy surface are expected to be in-plane.

4.3 Static hysteresis measurements

4.3.1 Polar MOKE

The static hysteresis of each sample is measured using a self-built static MOKE setup in polar geometry to extract key magnetic parameters, including the saturation and coercive fields. This setup uses a stronger electromagnet than the one used in time-resolved measurements, reaching field strengths of up to 2200 mT. Such high field strengths are necessary because the saturation magnetization is expected to be high due to the strong anisotropy in the out-of-plane direction.
Figure 24 compares the hysteresis loops of thin $TbFe_2$, $DyFe_2$, Terfenol-D, and thick uncapped $TbFe_2$. For the thick $TbFe_2$ sample, the recorded hysteresis is in good agreement with the data from Parpiiev et al. [41], confirming the high saturation fields exceeding the electromagnet's maximum field of 2200 mT.
Thin $TbFe_2$ and $DyFe_2$ (a, b) exhibit similar hystereses, an unexpected result given that the free energy surfaces suggest a significant out-of-plane difference. The saturation fields are also significantly lower than for thick $TbFe_2$ (c). Previous studies on the growth of $REFe_2$ layers have shown that the first few tens of nanometers exhibit a disordered island when grown on Niobium [37]. This can then lead to a reduced magnetocrystalline anisotropy, which would explain the lower saturation fields and the similarities between the thin samples. For sufficiently thick films, the crystallinity improves in the probed near-surface region, leading to a higher measured saturation field.
The hysteresis from Terfenol-D (d) displays a prominent background signal, which strongly distorts the shape of the hysteresis. It is partially subtracted using a linear fit in the saturation region, however some irregularities remain. The uncorrected hysteresis loops are presented in the Appendix for comparison.
In general the measurement results from this setup are less accurate at very high fields, because sample holder movement likely causes the bending of the hystereses observed at high positive and negative external B-fields. This additional signal distortion could explain the irregular shape of the $Tb_{0.3}Dy_{0.7}Fe_2$ hysteresis.

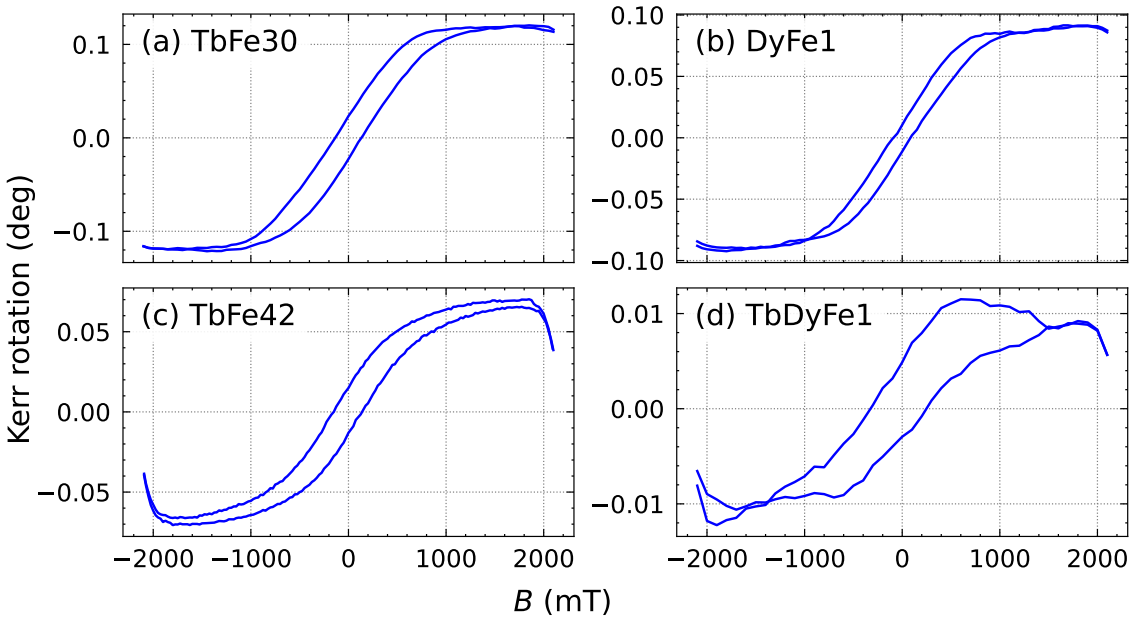

Figure 24: Static polar hystereses of the three thin $REFe_2$ samples (a, b, d) and the thick uncapped $TbFe_2$ sample (c). The hysteresis of Terfenol-D (d) is corrected by a background subtraction.

Table 4: Hysteresis parameters in polar geometry for the three thin $REFe_2$ samples and the thick uncapped $TbFe_2$ sample.

	$TbFe_2$ (20 nm)	$TbFe_2$ (450 nm)	$DyFe_2$	$Tb_{0.3}Dy_{0.7}Fe_2$
saturation field B_{sat} (mT)	1500	> 2200	1050	1450
coercive field B_c (mT)	130	150	90	290
saturation Kerr rot. θ_{sat} (deg)	0.118	0.071	0.084	0.009
remanence Kerr rot. θ_r (deg)	0.023	0.014	0.014	0.004

4.3.2 Longitudinal MOKE

Static longitudinal MOKE measurements are sensitive to the in-plane component of the magnetization. Thus, these measurements can be used to map the expected strong in-plane anisotropy in $TbFe_2$ and $DyFe_2$ by rotating the samples in-plane with respect to the magnetic field. Due to the strong shape and magnetocrystalline anisotropies, the in-plane directions are generally easier to saturate than the out-of-plane direction, so smaller field amplitudes are required. The results presented in Figure 25 again highlight the differences between thin and thick films. While thick $TbFe_2$ (c) exhibits a

characteristic switching behavior in one direction (labeled 0°), no switching is observed in the orthogonal direction (90°). This corresponds to easy and hard axes, as expected from shape of the free energy surface. In contrast, the LMOKE hystereses of the thin $TbFe_2$ and $DyFe_2$ films (a, b) are almost isotropic, indicating a significantly reduced anisotropy. The hysteresis of Terfenol-D (d) has an irregular shape again.

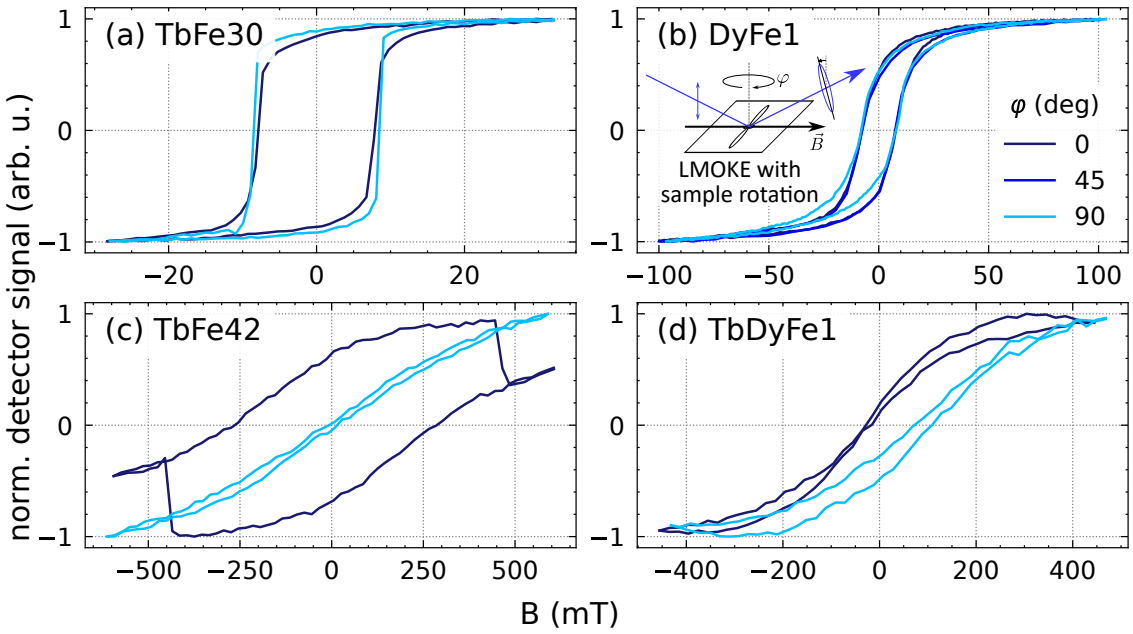

Figure 25: Static longitudinal hystereses of the three thin $REFe_2$ samples (a, b, d) and the thick uncapped $TbFe_2$ sample (c) without any background correction.

4.4 Static x-ray diffraction measurements

As suggested in the previous section, the significant differences in the magnetic hystereses between thin and thick $TbFe_2$ are likely linked to differences in their crystalline structure. X-ray diffraction (XRD) is used to characterize the crystal structure of the different samples. Constructive interference occurs under the Bragg condition:

$$n\lambda = 2d \sin\theta, \tag{61}$$

where n is the diffractive order, $\lambda = 1.54\,\text{Å}$ is the wavelength of the copper Kα-line, d is the spacing of a given set of crystal planes and θ is the Bragg angle. A more general formulation of the Bragg condition is the Laue condition:

$$\vec{Q} := \vec{k}_{\text{out}} - \vec{k}_{\text{in}} = \vec{G}. \tag{62}$$

Constructive interference occurs when the scattering vector $\vec{Q} := \vec{k}_{\text{out}} - \vec{k}_{\text{in}}$ matches a reciprocal lattice vector $\vec{G}$ of any set of lattice planes. The measurement geometry

for a setup with a fixed sample and rotatable x-ray source and detector is shown in Figure 26. In the following sections, one-dimensional XRD patterns, as well as two-dimensional reciprocal space maps (RSM) of different sample structures are compared.

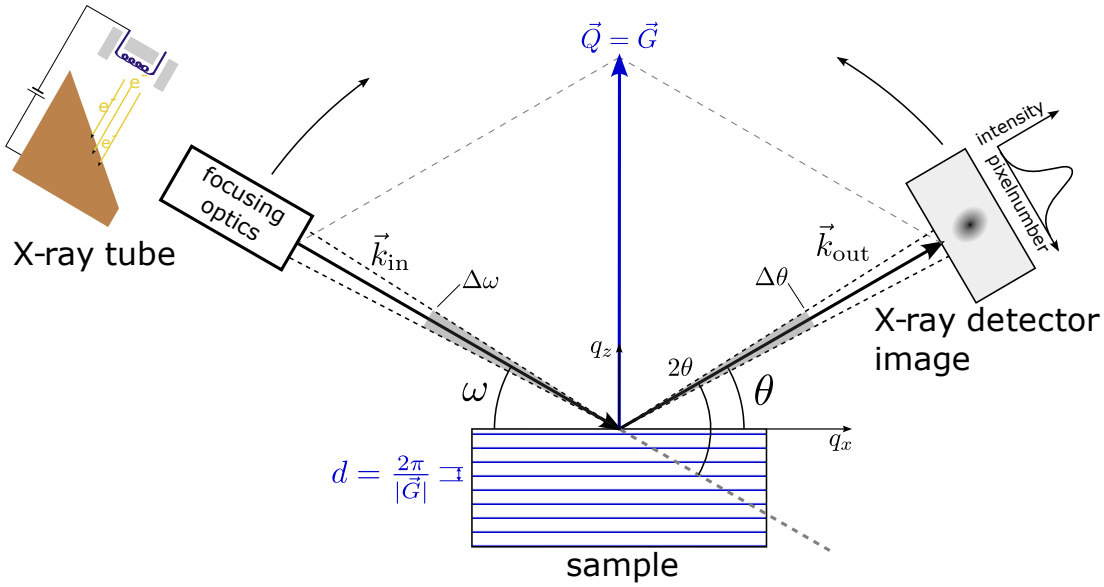

Figure 26: Schematic of a static x-ray diffraction setup. X-rays are generated by a Cu Kα tube and strike the sample at an incident angle ω. The diffracted beam is measured with an (area) detector at the angle θ. Both the x-ray tube and the detector are rotatable around the sample surface. Figure adapted from [58].

4.4.1 θ-2θ-scans measured with commercial XRD setup

The thick and thin samples are analyzed with a commercial XRD setup shown in Figure 27. The layout is similar to the setup sketched in Figure 26. The x-rays are generated by an x-ray ray tube with a copper anode that is monochromatized to the $K_{\alpha 1}$ and $K_{\alpha 2}$ lines around 8048 eV. The beam is collimated and parallelized by a combination of a 1/8 mm slit mask, a multilayer mirror and a 1 mm point mask. The diffracted x-rays are measured by an area detector, which is treated as a point detector in the available measurement modes, i.e. the intensity is integrated over all pixels.

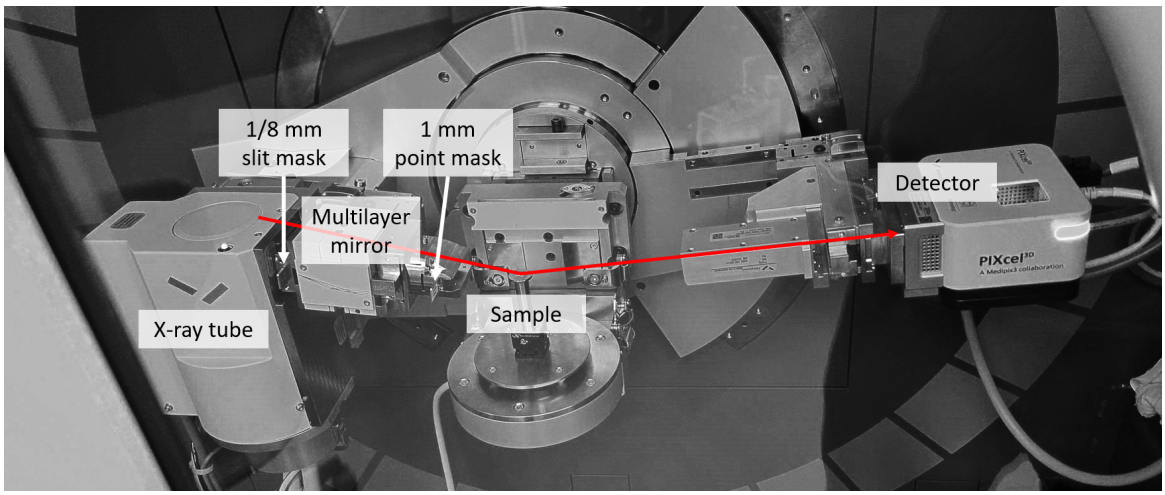

Figure 27: Image of the commercial x-ray diffraction setup. Both the x-ray source and the detector are mounted on a goniometer to perform θ-2θ scans. Point and slit masks can be inserted into the beam to aid collimation.

Figures 28 and 29 show the θ-2θ-scans obtained by a symmetric rotation of the x-ray source and the detector, as indicated by the arrows in Figure 26. The peaks in the diffraction patterns are identified by comparing their position with the prediction from the Bragg condition.
The thick $TbFe_2$ specimen exhibit a strong and sharp Al_2O_3 $(11\bar{2}0)$ substrate peak at 18.9°, a prominent $TbFe_2$ (220) reflection at 17.4° and a peak from the Nb buffer layer at 19.4° (110). Additional peaks mainly correspond to reflections from the SiO_2 capping, which are absent in the uncapped $TbFe_2$ sample. The similarity in $TbFe_2$ peak shapes suggests a consistent crystalline structure within this sample group.
For the thin samples, the substrate and Nb peaks remain unchanged, as only the $REFe_2$ thickness differs. A significantly smaller and broader (220)-reflection of $REFe_2$ is observed for all three samples in this category, due to the much smaller layer thickness. Among them, the Terfenol-D sample shows the largest Bragg peak amplitude, likely due to its larger layer thickness of 40 nm, compared to 20 nm for the others. The small peak at $\theta \approx 14.8°$ may be caused by the Al capping.

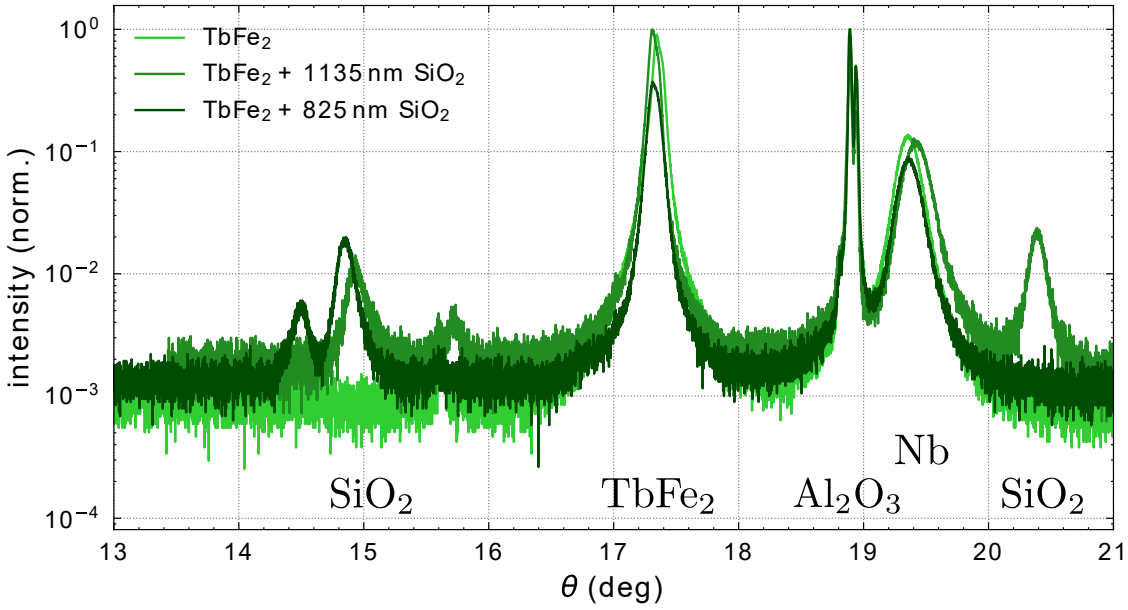

Figure 28: Bragg diffraction patterns of the thick $TbFe_2$ samples. Most features between the different samples are similar, besides the peaks from the glass capping which appear at different locations, or are entirely absent in case of the uncapped $TbFe_2$ sample.

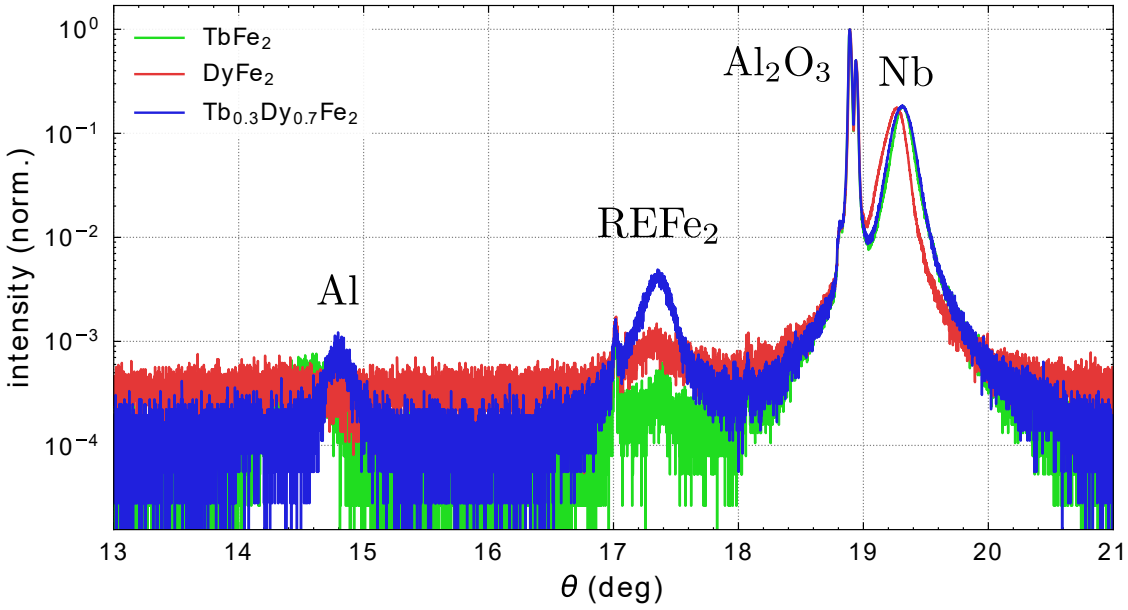

Figure 29: Bragg diffraction patterns of the thin $REFe_2$ samples. While the substrate and Nb buffer peaks remain unchanged, the intensity and width of the $REFe_2$ peak shows some variations. Especially in $Tb_{0.3}Dy_{0.7}Fe_2$, the peak is significantly sharper and more pronounced because of the thicker layer, but a better crystallinity could also contribute.

4.4.2 Reciprocal space maps measured using an area detector

As observed in the static MOKE measurements, the thin samples exhibit a smaller saturation field, that indicates a smaller magnetocrystalline anisotropy, which might originate from a larger mosaicity. The mosaicity is defined as the amount of spread of the crystal plane orientations in the crystallites. For a polycrystalline sample, the crystallites are randomly orientated and some of them fulfill the Bragg condition. This creates a ring-shaped diffraction pattern, compared to the point-like pattern for a monocrystalline sample. Thus by analyzing the shape of the diffraction patterns, information about the crystalline structure is obtained. This requires measuring a reciprocal space map (RSM), which shows the diffraction intensity for each scattering vector $\vec{Q} = (q_x, q_y, q_z)$. Scanning with θ-2θ-geometry results in a scan along q_z. Because an area detector is used, some slightly asymmetrical scattering events with $q_x \neq 0$ are also detected by the off-center pixels. Because the thin films are assumed isotropic in-plane, q_y is often omitted in the analysis. Thus, a sequence of detector images obtained from a θ-2θ-scan is converted into the reciprocal space (q_x, q_z). A more detailed description of this process is found in the PhD thesis of von Reppert [57].

Figure 30 compares the RSMs for thin $TbFe_2$ (a), thick $TbFe_2$ (b) and thick, glass capped $TbFe_2$ (c). These measurements were performed by Zeuschner and von Rep-

pert in 2018. The general trends from the θ-2θ scans (Figures 28, 29) are observed again, especially the variation of the $TbFe_2$ peak intensity with the corresponding layer thickness. To get information about the mosaicity, the width of the peaks along the q_x-axis is analyzed. As only a small part of the reciprocal space is mapped, the diffraction rings appear as line-like ring segments. The substrate (Al_2O_3) is almost perfectly monocrystalline, thus the peak width is limited by the instrument function of the plasma x-ray source (PXS). The other peaks are clearly broadened along q_x by some degree.

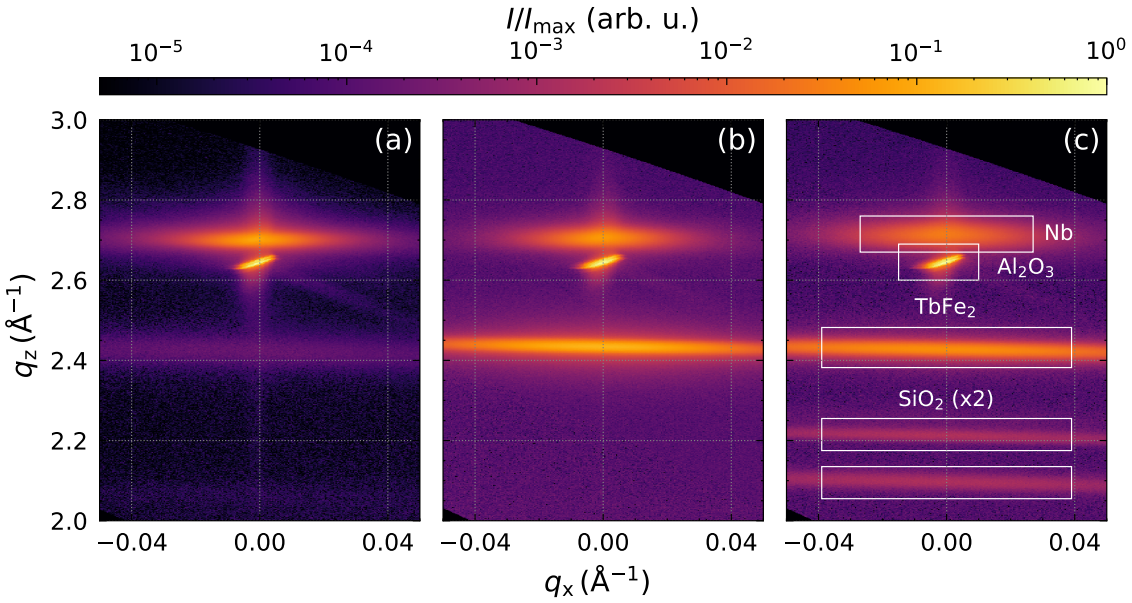

Figure 30: Reciprocal space maps of 20 nm $TbFe_2$ (a), 450 nm $TbFe_2$ (b) and glass-capped 335 nm $TbFe_2$ (c). Like in the θ-2θ-scans before, the intensity of the $TbFe_2$ peak changes significantly with the layer thickness. Note that the q_z-position of the peaks does not change for the different samples.

For a better comparison, the intensity is integrated along q_z in the respective areas indicated by the white rectangles. The resulting intensity profiles are presented in Figure 31. It is easily visible that thin $TbFe_2$ exhibits a significantly broadened Bragg peak (i.e. a diffraction ring), comparable to amorphous SiO_2. In comparison, the peak width is much smaller for thick $TbFe_2$, indicating a smaller mosaicity in the layer. These results confirm the observations from Mougin et al. [37], that initially the $TbFe_2$ films grow disordered in the first nanometers. As the thin films are affected much stronger by this, their Bragg peaks are much more broadened.

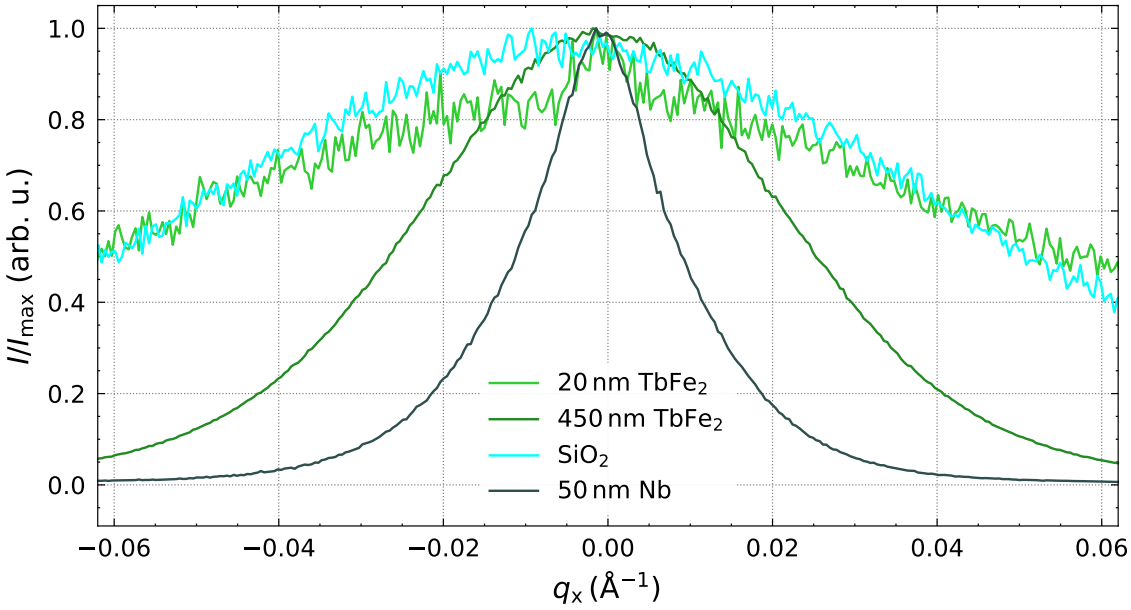

Figure 31: Slices of the RSM along q_x for several Bragg peaks. The integrated areas are indicated by the white rectangles in Figure 30. It can be seen that the Bragg peak in thin $TbFe_2$ is significantly broader compared to thick $TbFe_2$, likely due to differences in their mosaicity. Data for SiO_2 and Nb is shown for comparison with an amorphous and crystalline material, respectively.

4.5 Summary static sample characterization

Static hysteresis measurements of the different $REFe_2$ samples show significantly different saturation fields, especially when comparing thin (20 nm) and thick (450 nm) $TbFe_2$ films. Inhomogeneous growth of the $REFe_2$ layer in the first nanometers likely leads to a reduced magnetocrystalline anisotropy and thus saturation field. The reduced anisotropy also explains why the hysteresis loops of thin $TbFe_2$ and $DyFe_2$ are similar, as their main difference is their anisotropy. This is further supported by static XRD characterization, where the thin $REFe_2$ layer exhibits a significantly broadened Bragg peak in the q_x-direction, typical for a polycrystalline sample with larger mosaicity. These differences also impact the time-resolved MOKE measurements, as discussed in more detail in Sections 5 and 6.

5 Measurements with out-of-plane field

In this section, results from trMOKE measurements obtained with the electromagnet setup that provides a tuneable out-of-plane field are presented. As explained in Chapter 3, this allows for magnetic field strengths up to 1400 mT, and the field can be easily reversed by inverting the current through the coils. However, the field angle is fixed to 90°, i.e. perpendicular to the sample surface. This measurement series aims to explore and compare the demagnetization timescales for the different $REFe_2$ materials and sample structures, starting with the thin samples, where all three materials are available ($TbFe_2$, $DyFe_2$, $Tb_{0.3}Dy_{0.7}Fe_2$). They provide an overview of the intrinsic magnetization response upon direct laser excitation that is probed almost homogeneously.
The second part of this chapter presents the trMOKE measurements of thick $TbFe_2$ samples with and without glass capping. Here, especially the effects of strain on the MOKE signal are investigated. Thick structures lead to a delayed arrival of picosecond strain pulses that travel within the sample structure in the probed sample region. This allows separating the non-equilibrium magnetization dynamics that happens upon femtosecond laser-excitation from potential inverse magnetostriction effects in the time domain.

5.1 Probing the intrinsic magnetization response in thin $REFe_2$ films

To explore the intrinsic magnetization response of $REFe_2$ thin films upon laser excitation, two trMOKE measurement protocols are compared to the time resolved reflectivity. For each sample, the measurement series begins with a pump fluence series from $F = 2\,\mathrm{mJ/cm^2}$ to $10\,\mathrm{mJ/cm^2}$ at the maximum available external B-field $B_{\mathrm{ext}} = 1400\,\mathrm{mT}$ to see how the magnetization dynamics change with the strength of the optical excitation. The signals for various fields B_{ext} up to 1400 mT are also compared for a fixed fluence value. Transient reflectivity provides additional insights into the concomitant non-magnetic effects such as electronic excitation, picosecond strain pulse propagation and thermal energy transfer.

5.1.1 Fluence-dependent MOKE response

Figure 32 compiles the fluence-dependent trMOKE results for the thin $REFe_2$ specimen. Because of the damage threshold of the samples at $\approx 15\,\mathrm{mJ/cm^2}$, a maximum fluence of $F = 10\,\mathrm{mJ/cm^2}$ is chosen for the measurement series to avoid irreversible

damage to the sample. The resulting signal amplitudes increase with excitation fluence for each sample, but the overall signal shape depends on the material.

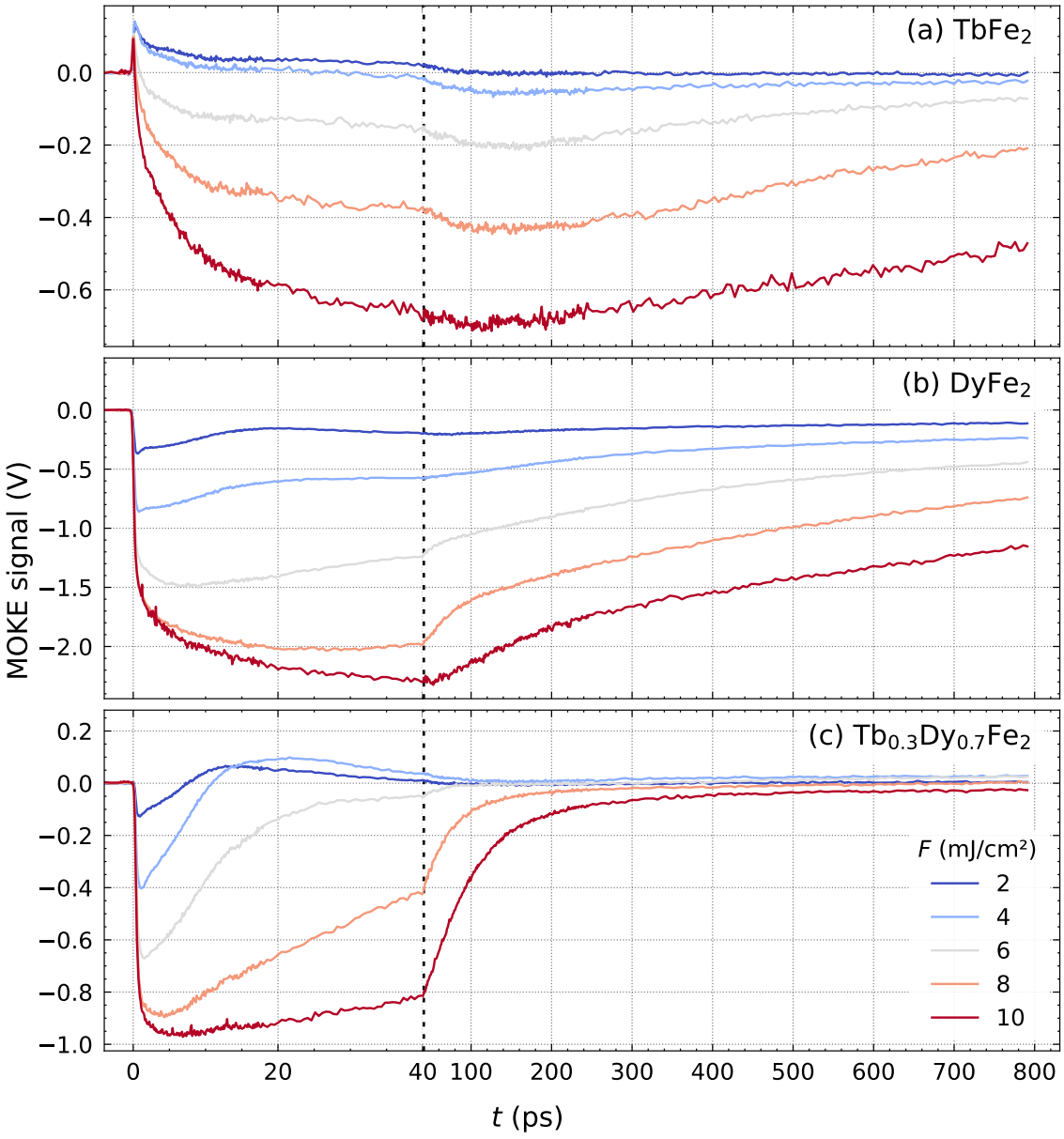

Figure 32: Excitation fluence dependent trMOKE response of 20 nm $REFe_2$ specimen at the maximum external field $B_{ext} = 1400\,mT$. Note that the x-Axis is broken at 40 ps in order to display the fast initial magnetization response and long time recovery in one graph. All samples exhibit a non trivial, fluence dependent magnetization response with multiple timescales in the initial 40 ps prior to the recovery. It is striking that Terfenol-D shows a much faster recovery of the trMOKE response in comparison to the TbFe2 and DyFe2.

All three specimen exhibit a sub-picosecond magnetization response and a second response on the timescale of 10s of picoseconds. In general, the signal shapes are quite complex, which makes it difficult to directly identify the demagnetization timescale. Depending on the fluence and the material up to four different timescales are observed. By fitting the trMOKE curves with a combination of exponential decay terms convoluted by a step function (Gaussian error function), the different timescales of the magnetization response and their fluence dependence are extracted.

$$f(t) = \frac{1}{2}\left[1 + \mathrm{erf}\left(\frac{t - t_1}{\tau_1}\right)\right] \cdot \left[A_2 \mathrm{e}^{-t/\tau_2} + A_3 \mathrm{e}^{-t/\tau_3} + A_4 \mathrm{e}^{-t/\tau_4}\right] \tag{63}$$

Because of the complex magnetization response, that might be superimposed by the onset of a magnetization precession that is discussed in chapter 6.1.1, the fits are only performed for the measurements above $6\,\mathrm{mJ/cm^2}$. The results are summarized in Table 5.

Table 5: Fitted timescales in ps for the magnetization response of the 20 nm $REFe_2$ films at different fluences. Timescale τ_1 is the width of the step function, representing the initial decay or increase. The other values correspond to the time constants of the different exponential decays used to fit the signal, including the remagnetization. Some parameters change strongly with the fluence, while others only fluctuate within a small interval.

	$TbFe_2$				$DyFe_2$				$Tb_{0.3}Dy_{0.7}Fe_2$			
$F\ \left(\frac{\mathrm{mJ}}{\mathrm{cm^2}}\right)$	τ_1	τ_2	τ_3	τ_4	τ_1	τ_2	τ_3	τ_4	τ_1	τ_2	τ_3	τ_4
6	0.1	1.7	78	506	0.3	3.3	29	749	0.3	4.9	5.0	38
8	0.1	2.5	77	795	0.4	14	38	919	0.3	2.1	41	381
10	0.1	1.4	17	2119	0.4	15	163	1769	0.4	38	39	458

The timescale of the initial sub-picosecond feature (τ_1), which is most likely caused by ultrafast demagnetization, does not strongly depend on the laser excitation fluence. The typical values stay within 0.1 to 0.4 ps under all tested conditions. The observed timescale in the experiment is probably somewhat overestimated, because the pump pulse duration of ≈ 150 fs limits the temporal resolution. Interestingly, this feature is positive for $TbFe_2$, which is contrary to a pure ultrafast demagnetization response. This hints towards different ultrafast sublattice magnetization dynamics.
The second feature (τ_2) corresponds to a slower decrease, following the initial excitation. For $TbFe_2$ it remains between 1 to 3 ps, while for $DyFe_2$ and Terfenol-D it increases with fluence from 2 to 38 ps. $TbFe_2$ exhibits a third decrease (τ_3) which drops from 78 to 17 ps.
All samples exhibit a delayed recovery, as heat is transferred away from the probed layer into the substrate, leading to a remagnetization. This effect is expected to be strongly fluence dependent, because as more energy is deposited in the sample, it takes longer to dissipate. However, there are also significant differences observed

between the three materials. In $TbFe_2$ the remagnetization can be described by a single exponential decay (τ_4), whereas in the other materials a bi-exponential decay (τ_3 and τ_4) is required to accurately fit the data. While $TbFe_2$ and $DyFe_2$ show a remagnetization timescale on the order of several 100s of picoseconds, $Tb_{0.3}Dy_{0.7}Fe_2$ recovers much faster in just a few 10s of picoseconds. The longer τ_4 timescale there usually has only a very small amplitude, so the majority of the remagnetization is described by the faster τ_3. This can also be seen in Figure 32, there is little trMOKE signal amplitude for Terfenol-D, whereas the other samples show a strong signal even after 800 ps.

5.1.2 Field-dependent trMOKE response

The field dependence of the trMOKE signal is investigated to eludicate, which applied field yields the intrinsic demagnetization. The measurements are repeated at a low fluence $F = 1\,\mathrm{mJ/cm^2}$ (Figure 33) and an intermediate value of $F = 6\,\mathrm{mJ/cm^2}$ (Figure 34). The most interesting feature in these measurements is a second peak after the initial spike at $\approx 120\,\mathrm{ps}$, which appears at low fluences and fields, but only for $TbFe_2$ and $DyFe_2$. In the first case one even observes a strongly damped oscillation with a frequency of $\approx 2\,\mathrm{GHz}$ for an external field of $B_{\mathrm{ext}} = 800\,\mathrm{mT}$. Chapter 6.1.1 discusses that a rotatable field can prove these features to be in fact the beginning of a precession. In contrast, $Tb_{0.3}Dy_{0.7}Fe_2$ does not exhibit any signs of precession, and the field mostly scales the signal. Lower external fields cause larger precession amplitudes, which is fortunate for the measurements in rotated fields where the field strength of the permanent magnet is limited to 400 mT.

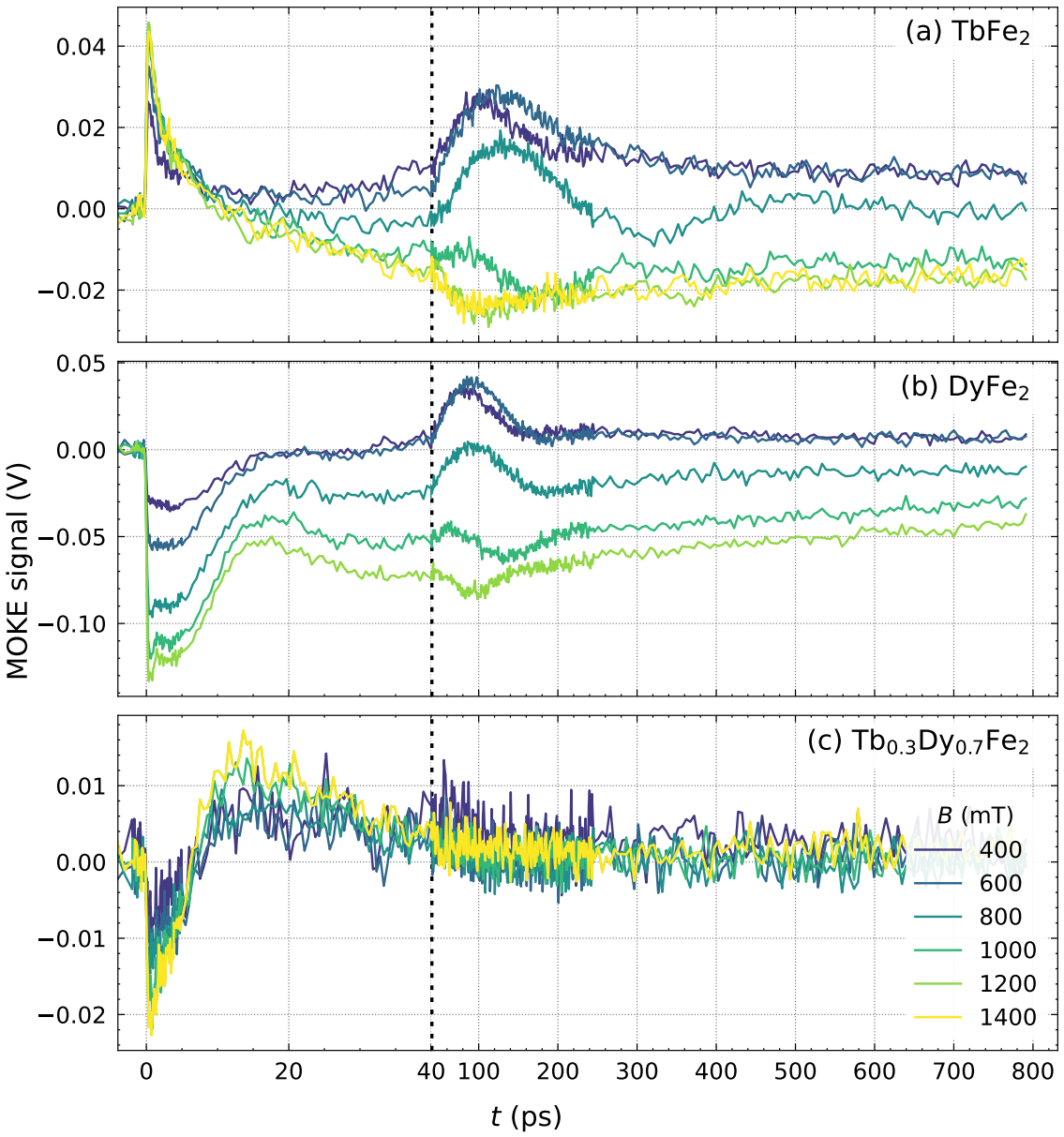

Figure 33: Field series for 20 nm $REFe_2$ at a low excitation fluence $F = 1\,\mathrm{mJ/cm^2}$. The onset of a precession can be observed in $TbFe_2$ (a) and $DyFe_2$ (b) at $\approx 120\,\mathrm{ps}$, with larger signals for lower fields. Terfenol-D (c) shows no precession and only minimal scaling of the trMOKE response with the external field.

At higher fluences, the precession in $TbFe_2$ and $DyFe_2$ is superimposed by a much stronger demagnetization, and shows up only at low fields as a shoulder at roughly the same position as the peak before ($\approx 120\,\mathrm{ps}$). A minor oscillation is present in the $DyFe_2$ signal at fields between 400 mT and 600 mT. Other than that, the external field mostly scales the signal and does not affect the timescales observed in

the magnetization response. Saturation is observed for $TbFe_2$ and $Tb_{0.3}Dy_{0.7}Fe_2$ at 1000 mT and 1200 mT respectively, but not for $DyFe_2$, likely due to the harder out-of-plane axis for this material. These values are slightly smaller than the saturation fields measured in the static experiments (Table 4), likely because of a reduced anisotropy at higher temperatures following the excitation.

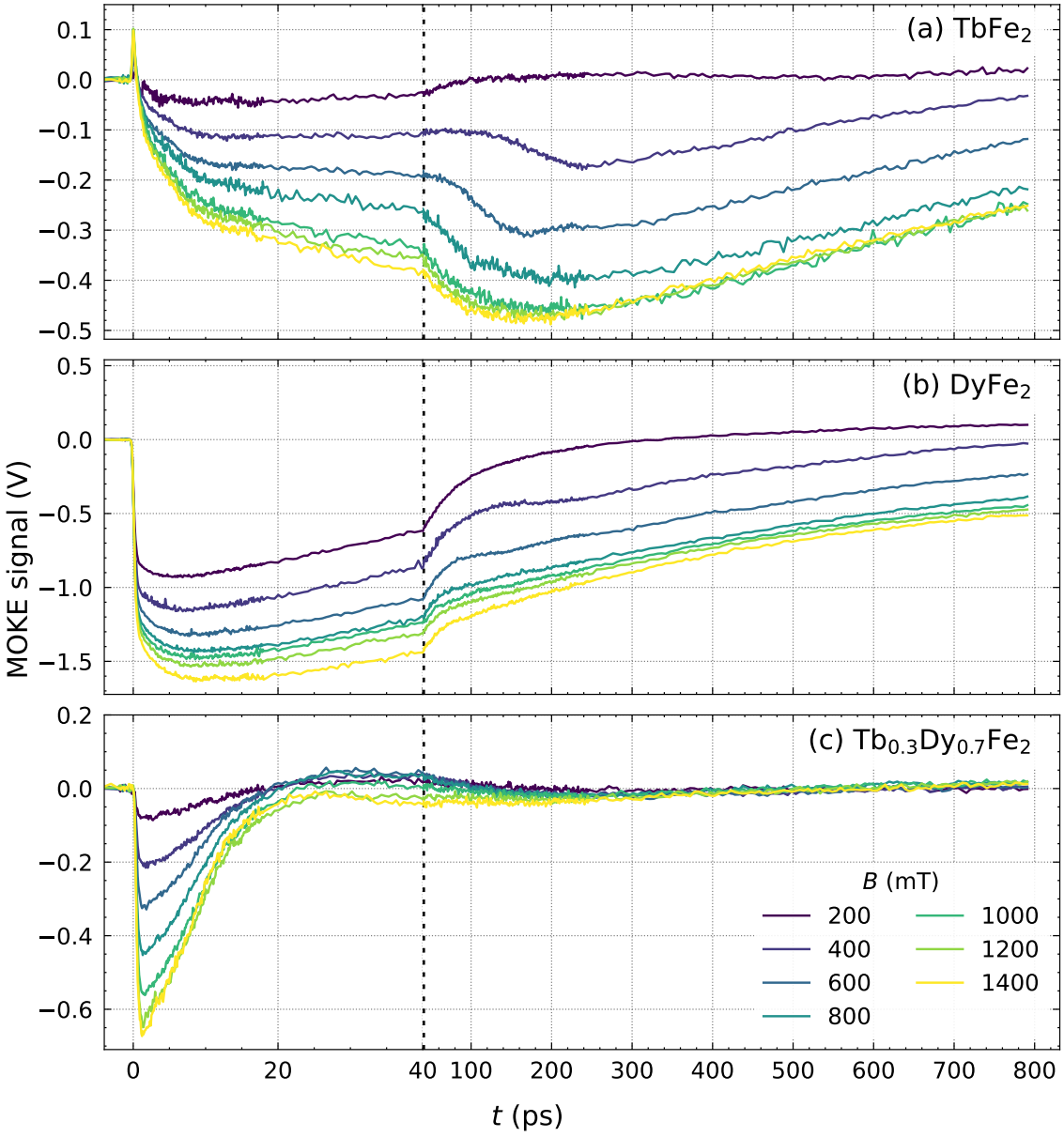

Figure 34: Field series for 20 nm $REFe_2$ samples in intermediate fluence regime at $F = 6\,\mathrm{mJ/cm^2}$. Precessions are strongly suppressed by a much larger demagnetization signal, though some traces can still be observed at field values around 600 mT in $TbFe_2$ and $DyFe_2$. In general, the external field scales the MOKE signals, until a saturation value is reached.

The field dependent trMOKE measurements demonstrate that there is no single set of optimal conditions for the experiment. While large fluences and fields generally create the largest trMOKE signals, some features like precession are enhanced at lower fluences and fields. However, the overall decrease of the signal to noise ratio requires longer integration times to obtain the observables with reasonable accuracy.

5.1.3 Transient reflectivity

In addition the thin samples are investigated with two field-independent measurement methods: transient reflectivity and the field-independent contribution to the polarization rotation, as introduced in section 3. This allows for probing and exploring the laser-induced non-magnetic processes in the same specimen in the same setup under similar excitation conditions. In Figure 35, these results are compared for all three materials, along with a comparison of trMOKE measurements at the same pump fluence. Although many processes change the reflectivity signal, they can be distinguished by considering their relevant timescales. The reflectivity signal consists of a sub-picosecond feature, which is caused by electronic excitations immediately after the pump pulse excites the sample. Interestingly, this signal is positive for $TbFe_2$, whereas the other samples show a negative initial signal.
The initial electronic response is followed by a pronounced oscillation, that is likely caused by a strain wave exiting the probed near surface sample region. The following slow relaxation on a nanosecond timescale can be understood as thermal energy transfer away from the probed sample region. It is notable that unlike the trMOKE signals, the reflectivity exhibits very similar timescales for all three samples. Especially in $Tb_{0.3}Dy_{0.7}Fe_2$ a strong discrepancy between the trMOKE and reflectivity signals observed, with the trMOKE signal recovering significantly faster than the reflectivity. So even though the sample is still hot, as indicated by the large transient reflectivity signal, the magnetization has apparently already fully recovered. A possible explanation for this might be the opposing magnetocrystalline anisotropy contributions of the Tb and Dy contents within the $Tb_{0.3}Dy_{0.7}Fe_2$ layer, causing opposing trMOKE signals that cancel each other. This is not the case for the other two materials, where the relaxation of trMOKE and reflectivity signals happens over similar timescales.
The field-independent polarization rotation shows the signatures of rotational alignment of molecules in strong light fields that induce a birefringence of the air, known from chapter 3.2.4. Because these features are very sharp they look similar to noise, but actually appear only at well defined delays. Furthermore a slowly varying background signal can be observed, most prominently in $TbFe_2$ and $Tb_{0.3}Dy_{0.7}Fe_2$ which is caused by a transient birefringence of the sample following the excitation. This background signal shows characteristic oscillations for $Tb_{0.3}Dy_{0.7}Fe_2$ at $f = 10\,\mathrm{GHz}$. These oscillations could be caused by echoes of shear waves. The lack of in-plane anisotropy in Terfenol-D allows in-plane alignment of the magnetization by even a small field component. This is almost always the case, as even the out-of-plane fields are probably slightly tilted. Demagnetization after excitation then launches a shear wave via in-plane magnetostriction, which then propagates through the material. Be-

cause of the similar densities and shear wave velocities in $Tb_{0.3}Dy_{0.7}Fe_2$ and Nb, the shear wave is only reflected at the Nb-sapphire interface. With a shear wave velocity of $v_S = 1.98\,\mathrm{nm/ps}$ and a layer thickness of 40 nm of the $Tb_{0.3}Dy_{0.7}Fe_2$ layer [8], and $v_S = 2.09\,\mathrm{nm/ps}$ in the 50 nm niobium layer [63], a frequency of 11.3 GHz is obtained, close to the measured frequency.

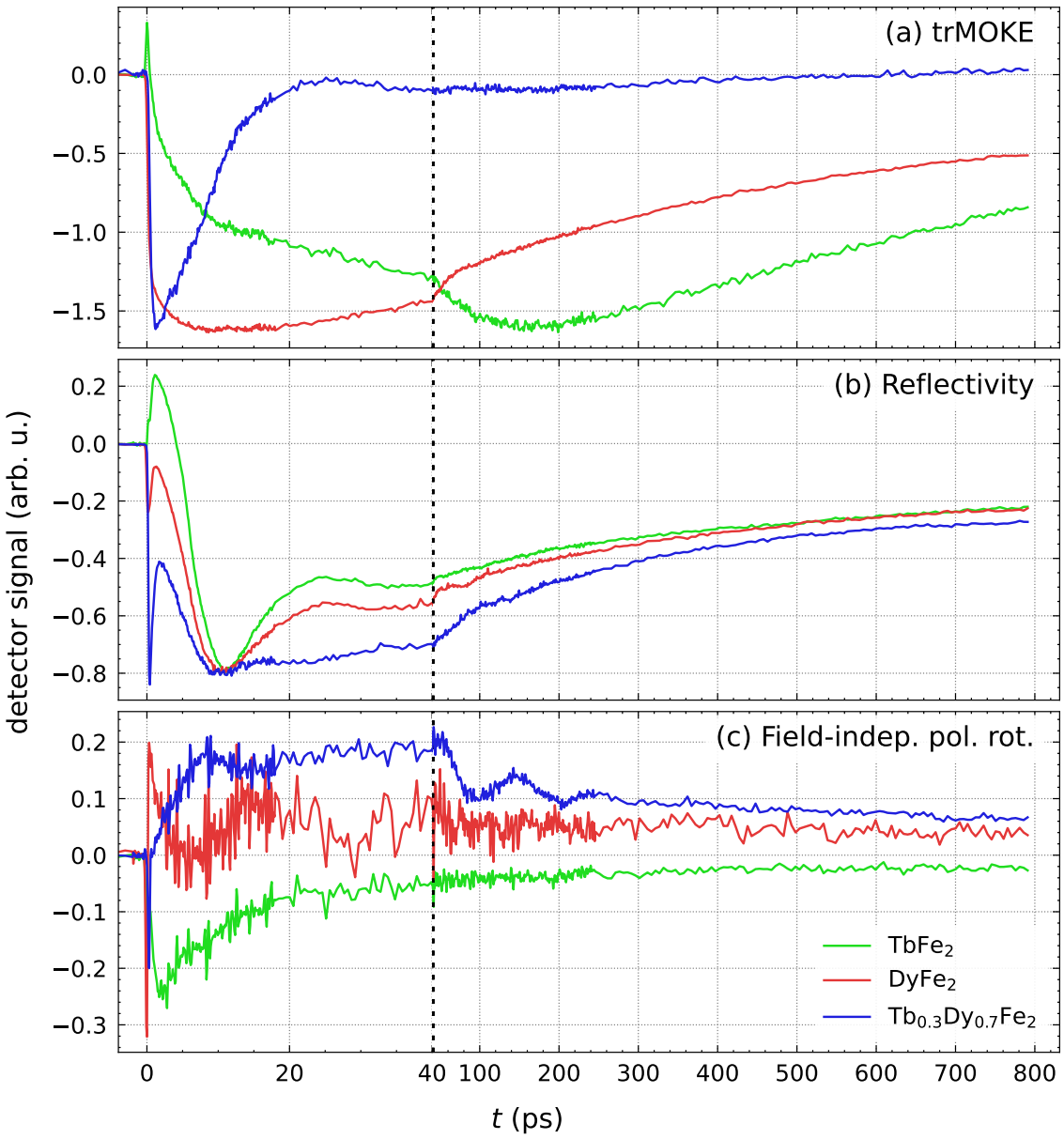

Figure 35: Comparison of trMOKE (a), transient reflectivity (b), and the field-independent polarization rotation (c) for under identical excitation conditions ($F = 6\,\mathrm{mJ/cm^2}$ and $B_{\mathrm{ext}} = 1400\,\mathrm{mT}$) for all three samples. In comparison to the trMOKE signals, the transient reflectivity explicitly contains electronic excitations as well as contributions from strain and thermal transport. Note that all three specimen exhibit the same timescales in the transient reflectivity response despite their notable differences in trMOKE measurements. The discrepancy is especially prominent in $Tb_{0.3}Dy_{0.7}Fe_2$. The field-independent polarization rotation shows the transient birefringence of non-magnetic origin. The signal of $Tb_{0.3}Dy_{0.7}Fe_2$ contains characteristic oscillations, which might be attributed to shear wave echoes.

An interesting observation is the field-dependence of the reflectivity signal, as it is expected it to look the same, regardless of the applied field. However if the field-dependent signal contribution is extracted by subtracting field-up and field-down measurements ($B_{\mathrm{ext}} = \pm 1400\,\mathrm{mT}$), a non-zero signal as shown in Figure 36 can be observed for all three samples. A possible explanation is the transversal magneto-optical Kerr effect (TMOKE), which causes a small difference of the reflectivity when switching the magnetization [2]. Ignoring the higher noise, the general shape of the signal actually looks very similar to the polar MOKE signal, further indicating a magnetic origin of this effect. Again the relaxation time is much faster for $Tb_{0.3}Dy_{0.7}Fe_2$, compared to the other other materials, consistent with the PMOKE measurements. However, the sharp peak at $t = 0\,\mathrm{ps}$ for $TbFe_2$ in the PMOKE response is not reproduced in the TMOKE measurements. It is known that the magnetization response is often mixed in the visible spectral range due to the overlap of the probed bands. This can be circumvented by TMOKE measurements with XUV light, which allows for element specific probing of the magnetization response [43].

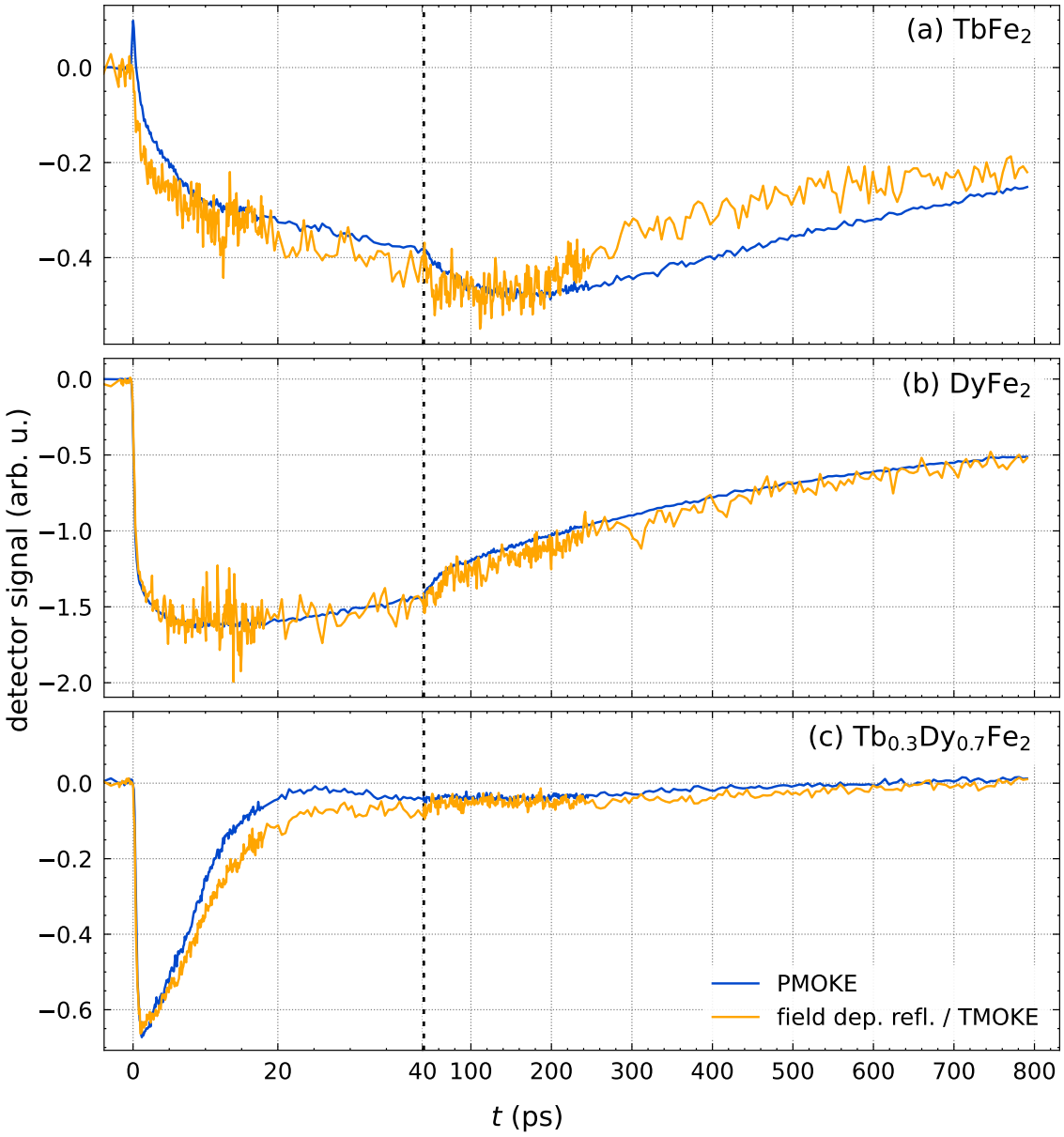

Figure 36: Field-dependent reflectivity displaying a pronounced transversal MOKE signal in direct comparison to a scaled polar MOKE response for all three 20 nm $REFe_2$ films. PMOKE and TMOKE signals are almost identical for each sample, because both methods measure the magnetization. The only notable difference between the two measurements is the absence of the peak at $t = 0$ in the TMOKE signal of $TbFe_2$ that might be obscured by the higher noise level of the TMOKE measurement.

5.2 Strain effects in thick $TbFe_2$ films

So far thin films were examined where demagnetization, change of the anisotropy parameters and strain dynamics all occur on similar timescales. In thick samples, delayed echoes of laser-induced strain pulses arrive at the probed near surface region, which allow for investigating the strain contribution to the trMOKE signal in the highly magnetostrictive specimen. Previous measurements for thick $TbFe_2$ films with and without SiO_2 glass capping by Zeuschner et al. [64] and Parpiiev et al. [41] have found significant strain pulse contributions to the trMOKE response. This subsection confirms this finding and provides further analysis.

5.2.1 Influence of the capping thickness

Figures 37 to 39 display the MOKE and reflectivity signals alongside the modelled strain response for three thick $TbFe_2$ samples. Surprisingly, the MOKE signal of thick $TbFe_2$ seems to be inverted, compared to thin $TbFe_2$ (comp. Figure 32). The initial feature is much more pronounced for SiO_2 capped samples, compared to the uncapped, as well as the thin sample. The signals show characteristic peaks caused by echoes of propagating strain pulses. Their timing depends on the layer thicknesses and their sound velocities. This can be rationalized by an analysis of the strain simulations obtained with the udkm1Dsim-toolbox [48, 49]. The resulting spatiotemporal strain maps (panel a-c) for the different samples always show that there are two main components to the total strain: quasi-static strain caused by thermal expansion ($\eta > 0$) of the uppermost layers after the laser excitation, and coherent strain pulses generated by the ultrafast thermal expansion. The local expansion in the excited near-surface region of the $TbFe_2$ causes a compression in the glass layer on top, and the $TbFe_2$ below, launching two compressive ($\eta < 0$) strain pulses in opposite directions. These pulses propagate through the sample layers with their corresponding sound velocities (compare the slopes in the strain maps) until they reach an interface. There the waves are transmitted and reflected according to the acoustic impedances Z on both sides (the product of density and sound velocity of the material, $Z_i = \rho_i v_i$), similar to the Fresnel equation for light:

$$R = \frac{Z_1 - Z_2}{Z_1 + Z_2}. \tag{64}$$

When the reflected strain echoes arrive in the probed near-surface region of the $TbFe_2$ layer, they can be detected with MOKE and reflectivity through magneto-acoustic coupling or strain-dependent changes of the refractive index respectively.
In the first sample, with a thick 825 nm SiO_2 (glass) capping, two distinct sets of strain pulses can be identified, causing two sets of peaks to appear in the MOKE signal. First, there are strong echoes from pulses propagating in the glass layer, arriving with a period of $\approx 310\,\mathrm{ps}$ ($f \approx 3.2\,\mathrm{GHz}$). The sign of the strain pulse changes upon each reflection off the glass-air interface because air has a lower acoustic impedance, again analogous to the 180° phase shift when light reflects off a medium with higher refractive index. So each of the echoes that arrives at the $TbFe_2$-SiO_2 interface exhibits

the opposite sign of the previous one. This is visible in the trMOKE signal as well. These strain pulses are so strong that even the fourth peak at 1235 ps can still be detected. Because the reflection coefficient at the glass-$TbFe_2$ interface is smaller than 1, the echoes are partially transmitted into the $TbFe_2$ layer. This creates a second set of strain pulses, propagating inside the $TbFe_2$. In contrast to the glass echoes, these pulses do not shift their phase upon reflection from the $TbFe_2$-Nb interface, as the Nb layer has a higher acoustic impedance. So these echoes always have the same sign as the previous glass echo. They also arrive with the same frequency, but they are delayed by the propagation time through the $TbFe_2$ layer, in this case ≈ 165 ps.
The reflectivity of the glass capped samples looks significantly different compared to the reflectivity of the uncapped samples discussed in the previous subsection. It exhibits strong oscillations that are caused by time-domain Brillouin scattering, as explained in Section 5.2.4. Phase shifts of these oscillations occur when the sign of the strain pulse propagating through the glass changes, upon each reflection off the glass-air interface. While the position of the peaks in the MOKE signal matches the strain simulation results (vertical dashed lines), the reflectivity phase changes are consistently shifted towards earlier delays. This could indicate a general trend that the trMOKE signal lags behind the reflectivity (compare Chapter 6.2.3). However in this case the shift is most likely caused by differences in the glass thickness across different probe spots, as the discrepancy is significantly smaller in the other samples (comp. Figure 38). Compared to the thin sample, the initial electronic feature appears inverted. This might be caused by the same mechanism that inverted the MOKE signals.

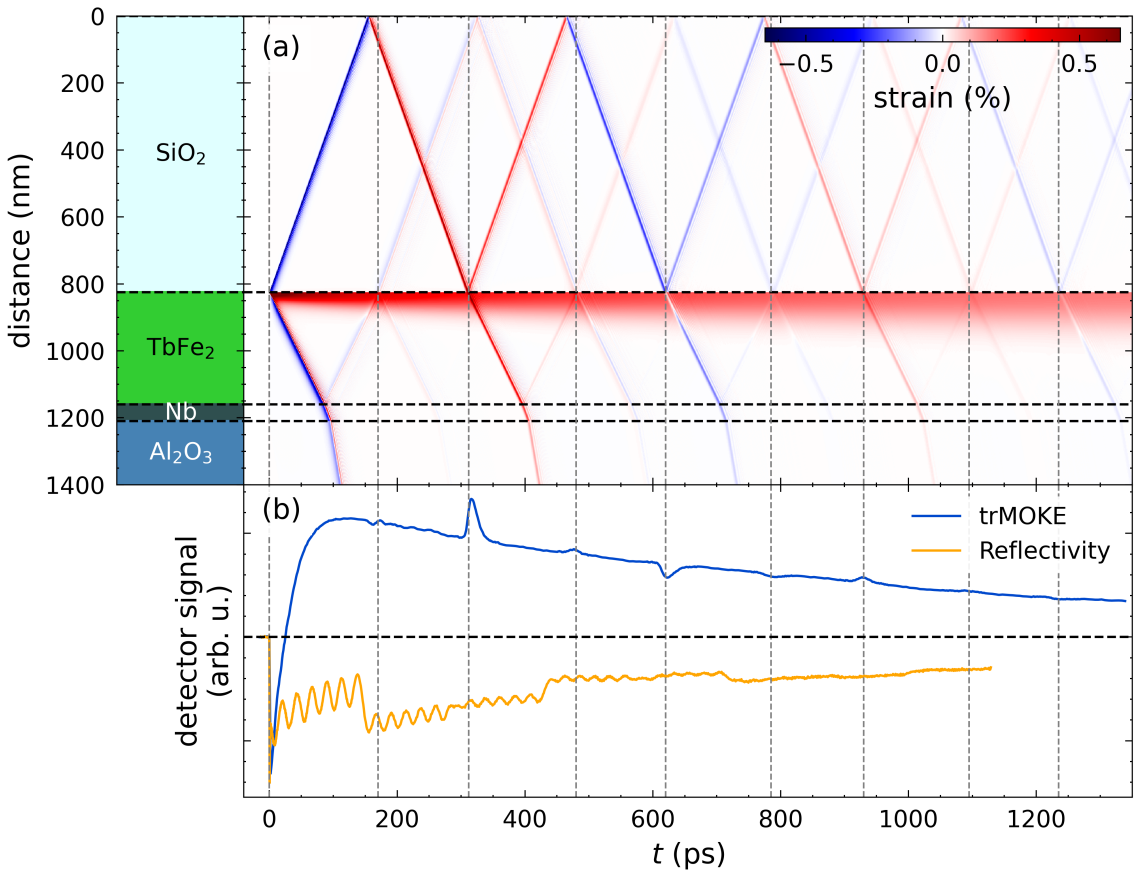

Figure 37: Strain map (a) and MOKE and reflectivity signals (b) for the 825 nm glass-capped $TbFe_2$ sample, measured at $F = 8\,\mathrm{mJ/cm^2}$ and $B_{\mathrm{ext}} = 1100\,\mathrm{mT}$. A schematic of the sample structure is added next to the strain map to guide the interpretation. The strain map shows both propagating coherent strain waves (red and blue lines) and quasi-static strain (diffuse red area near the $TbFe_2$ surface). Strain echoes from the glass and $TbFe_2$ layer show up in the MOKE and reflectivity signals. The reflectivity response consists of strong Brillouin oscillations, with phase jumps occurring every time the strain wave in the glass layer changes its sign.

Choosing a thinner glass capping of 530 nm changes the timings of the strain echoes. Now the propagation times through the glass layer and the $TbFe_2$ layer are almost equal, causing the peaks in the MOKE signal to overlap. The arrival period of the pulses is now much shorter at $\approx 195\,\mathrm{ps}$ ($f = 5.1\,\mathrm{GHz}$), while the delay to the second set of pulses is roughly the same at $\approx 175\,\mathrm{ps}$ (because the $TbFe_2$ thickness is the same). So the $TbFe_2$ echoes arrive just 20 ps before the next glass echo. This creates bipolar-like looking features in the MOKE signal, but they are still created by two separate echoes.

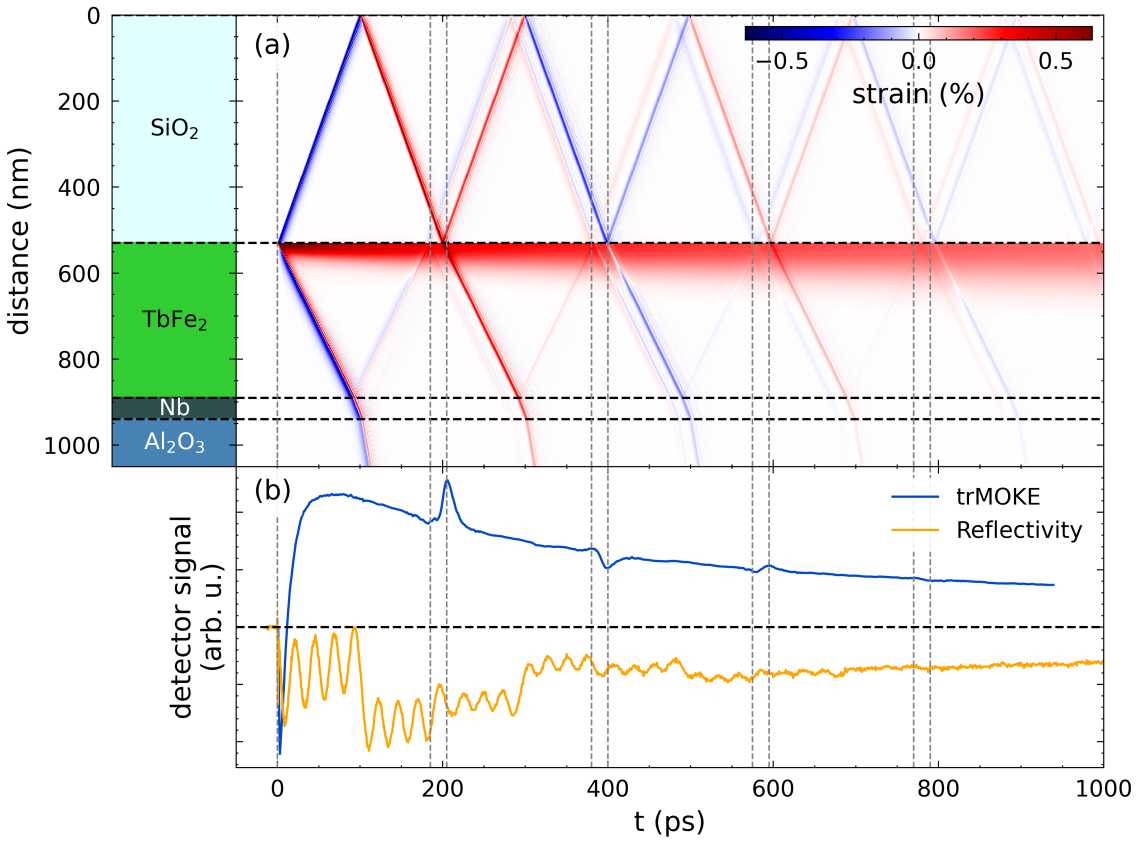

Figure 38: Strain map (a) and MOKE and reflectivity signals (b) for the 530 nm glass-capped $TbFe_2$ sample at $F = 8\,\mathrm{mJ/cm^2}$ and $B_{\mathrm{ext}} = 1300\,\mathrm{mT}$. A thinner capping increases the frequency at which the strain echoes arrive at the $TbFe_2$ surface.

Without the glass capping only the echoes in the $TbFe_2$ layer are observed. Because the reflection at the $TbFe_2$-Nb interface is relatively weak, only the first echo is strong enough to be observed. Here the upwards-propagating pulse is immediately reflected at the air interface, causing a 180° phase shift, and follows the compressive pulse as an expansive pulse, creating a bipolar strain profile. The thicker $TbFe_2$ layer in this sample leads to a longer propagation time of $\approx 230\,\mathrm{ps}$. Looking again at the strain map, there is a second echo from the Nb-sapphire interface, arriving shortly after the first echo, which might explain the small second bipolar feature at 255 ps. As this sample is uncapped, the reflectivity signal is not superimposed by Brillouin oscillations and shows a response that is very comparable to the reflectivity change observed in the thin $REFe_2$ specimen discussed in the previous subsection. The first strain echo at $\approx 230\,\mathrm{ps}$ can be observed too, however it appears slightly shifted. Already here one can speculate that the MOKE signal is a response of the magnetization driven by the strain with a little delay. This is discussed in more detail in Section 6.2.3.

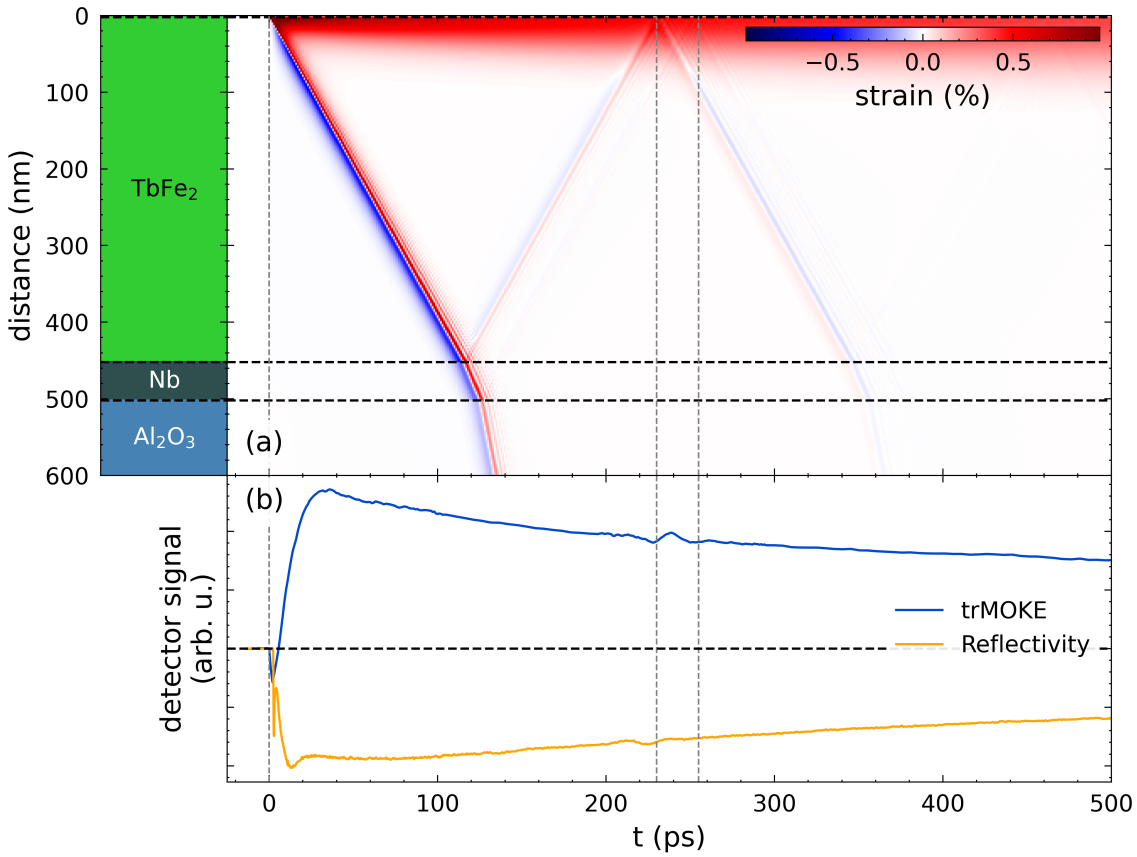

Figure 39: Strain map (a) and MOKE and reflectivity signals (b) for the uncapped $TbFe_2$ sample at $F = 8\,\mathrm{mJ/cm^2}$ and $B_{\mathrm{ext}} = 1300\,\mathrm{mT}$. Without the transparent SiO_2 capping, only the first echo from the $TbFe_2$-Nb interface is detected. The reflectivity signal does not exhibit Brillouin oscillations anymore, but an echo of the strain pulse that arrives in the near surface region of the $TbFe_2$ layer is visible both in the trMOKE response and the reflectivity signal.

5.2.2 Fluence-dependent trMOKE response

Having rationalized the overall shape of the trMOKE signals for the capped and uncapped samples it is interesting to investigate how they depend on the excitation fluence. As there is only one magnetic material available in this sample class, the fluence dependence of the trMOKE response is comparable for the three introduced sample structures. Figure 40 exemplifies the fluence dependence. The signal consists of a fast demagnetization in the first 1 to 2 ps, followed by a large positive signal that remains well beyond 1000 ps. Possible mechanism for this positive signal is either the competing demagnetization of the Tb and Fe sublattices, or a reduction of the magnetocrystalline anisotropy due to higher temperatures after the excitation, causing the magnetization to tilt outwards. The first negative demagnetization fea-

ture only changes in amplitude when increasing the fluence, until it saturates above $\approx 8\,\mathrm{mJ/cm^2}$. The positive signal is strongly fluence dependent, both in amplitude and speed. Surprisingly, the demagnetization amplitude seems to saturate already at $6\,\mathrm{mJ/cm^2}$, with even a slight drop towards higher fluences. The dynamics slow down significantly, the maximum signal is reached at $\approx 10\,\mathrm{ps}$ for $F = 3\,\mathrm{mJ/cm^2}$, but at $14\,\mathrm{mJ/cm^2}$, the maximum occurs only after 400 ps. The amplitude of the strain features scales with fluence, until a saturation value of $\approx 8\,\mathrm{mJ/cm^2}$ is reached.

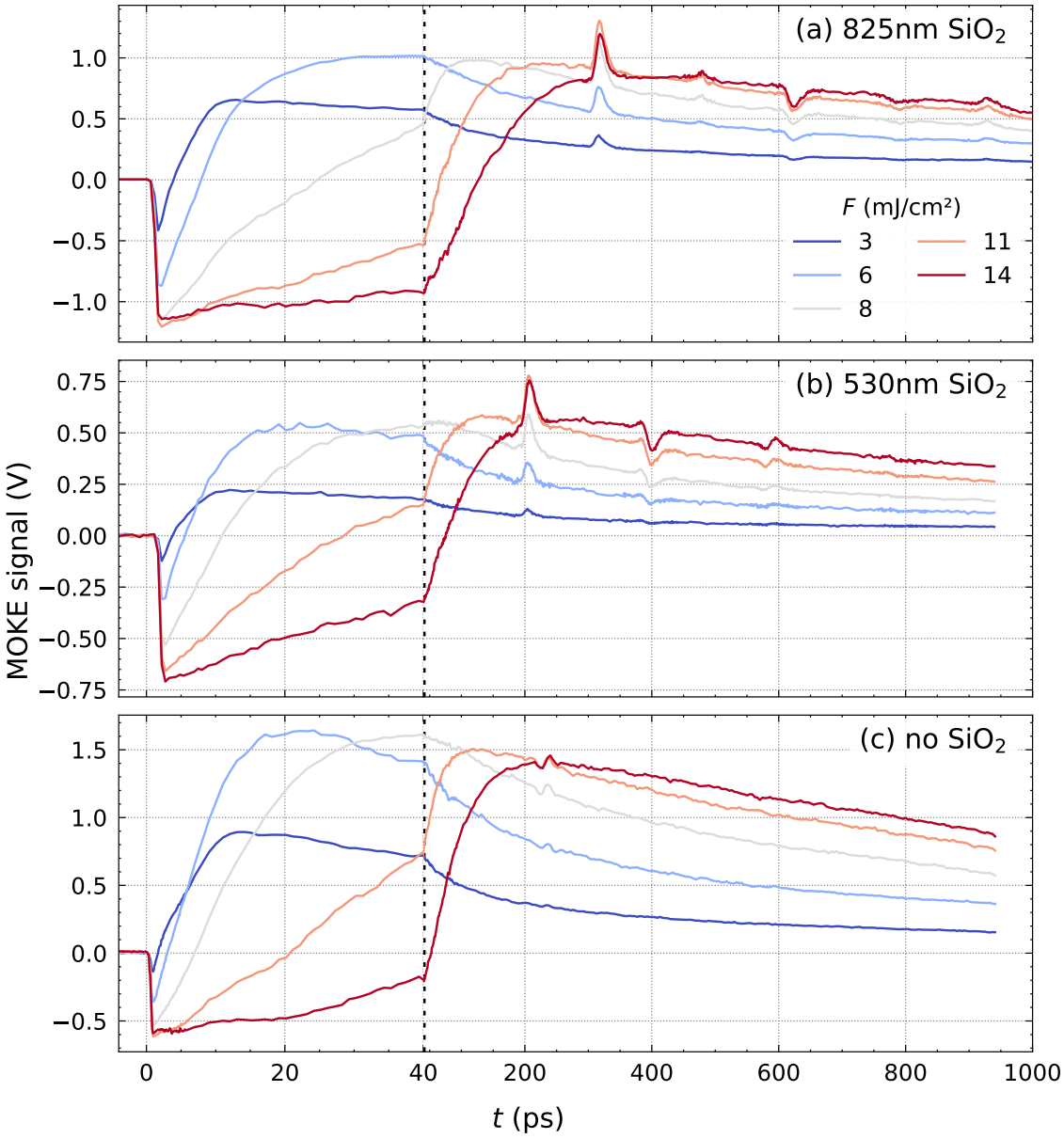

Figure 40: Fluence series for capped (a, b) and uncapped (c) $TbFe_2$ at maximum external field $B_{ext} = 1300\,\mathrm{mT}$. Higher pump fluences significantly slow down the dynamics, while the signal amplitude saturates between 6 to $8\,\mathrm{mJ/cm^2}$.

5.2.3 Field-dependent trMOKE response

Similar to the thin $TbFe_2$ sample, the external field mostly scales the signal as shown in Figure 41. While the saturation for the initial demagnetization is only reached above 1100 mT, the positive signal saturates at much lower fields of $\approx 700\,\mathrm{mT}$, even lower than for the thin sample. The saturation of the positive signal is also different

for each specimen. Similar to the thin samples, these saturation values are much lower than the saturation fields measured with the static MOKE setup. This is again attributed to a reduced anisotropy due to the laser excitation.

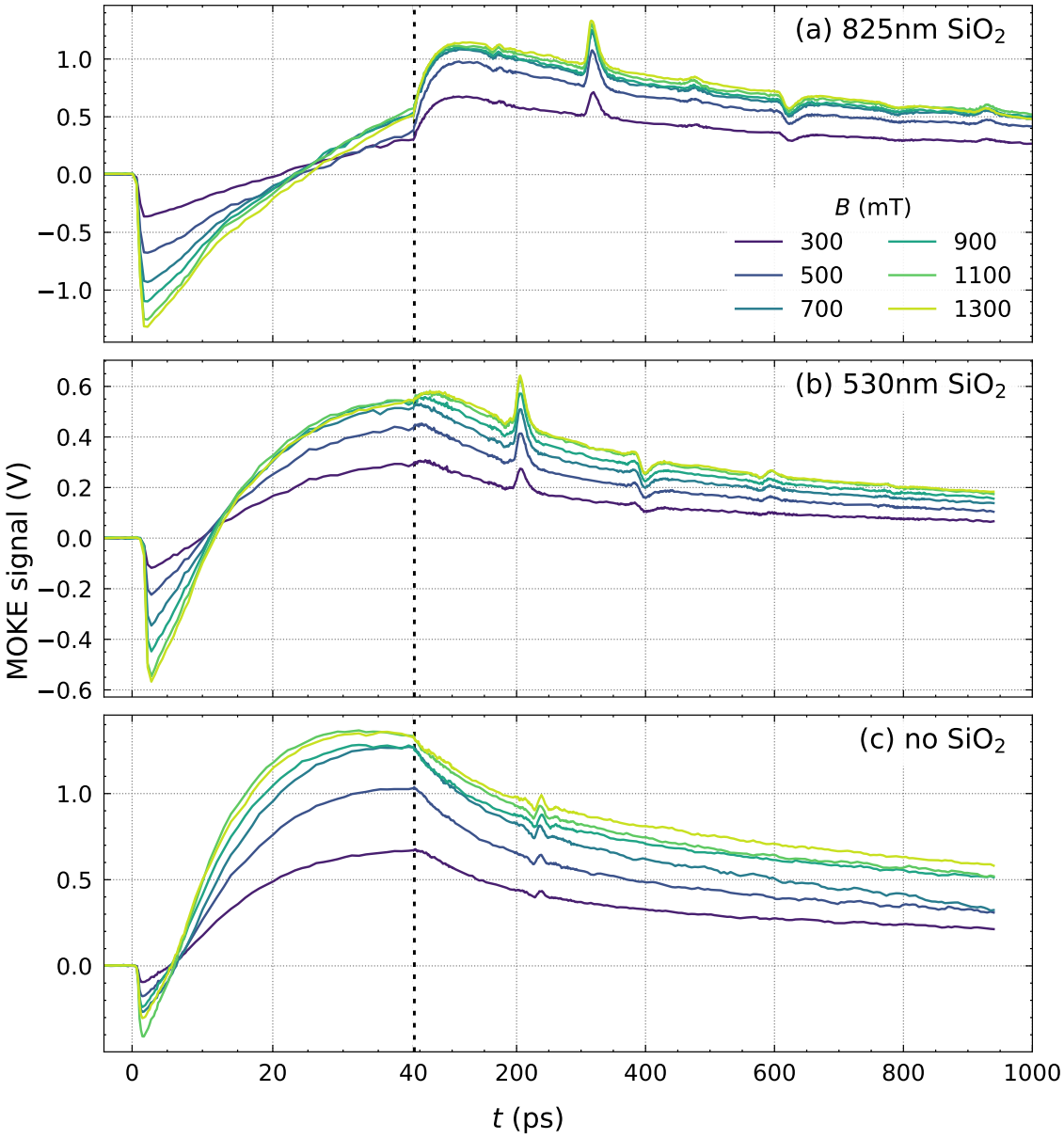

Figure 41: Field series for capped (a, b) and uncapped (c) $TbFe_2$ at $F = 8\,\mathrm{mJ/cm^2}$. Like for the thin samples, the external field scales the MOKE signals until the saturation field is reached. Interestingly, the required fields to saturate the trMOKE signal are different for each specimen, despite their similar composition.

5.2.4 Brillouin oscillations in the transient reflectivity

The strain dynamics is also observed in transient reflectivity measurements. In the transparent glass capping, the propagating strain pulses cause strong Brillouin oscillations, which dominate the signal. The reflectivity signals and their FFT are shown in Figure 42. In the FFT, there is a strong peak at 40.5 GHz and 38.5 GHz for the 825 nm and 530 nm capping respectively, corresponding to the frequency of the Brillouin oscillations. They are caused by the constructive and destructive interference of the probe light ($\lambda = 400\,\mathrm{nm}$), reflected from the sample surface, the glass-$TbFe_2$ interface and laser-induced propagating strain pulse within the glass capping. The strain wave locally changes the index of refraction n, creating an additional interface which allows for reflection. Depending on the distance between the surface and the strain wave, constructive interference occurs when

$$\lambda = 2nd = 2nv\Delta t = 2\frac{nv}{f}. \tag{65}$$

Because the strain wave propagates with the sound velocity v, d changes over time which leads to the oscillation in the reflectivity signal. For every delay Δt, where the condition is fulfilled, the constructive interference causes a maximum in the signal. From the observed frequency $f = 40.5\,\mathrm{GHz}$ with the thick capping the sound velocity in the glass layer (SiO_2) can be calculated, using $n = 1.47$ at $\lambda = 400\,\mathrm{nm}$ [31]:

$$v = \frac{\lambda f}{2n} = 5.5\,\frac{\mathrm{nm}}{\mathrm{ps}}. \tag{66}$$

For the thin capping the Brillouin oscillation frequency of $f = 38.5\,\mathrm{GHz}$ results in a sound velocity of $v = 5.2\,\mathrm{nm/ps}$. This is somewhat lower than the the literature value $v = 5.9\,\mathrm{nm/ps}$ [46], but the discrepancy can be explained by inhomogeneous growth of the SiO_2. For the strain simulations, the average of the experimentally derived sound velocity $v = 5.35\,\mathrm{nm/ps}$ is used. The uncapped sample exhibits no Brillouin oscillations and the reflectivity signal resembles that of the thin samples. The strain echo from the $TbFe_2$-Nb interface is visible at 220 ps.

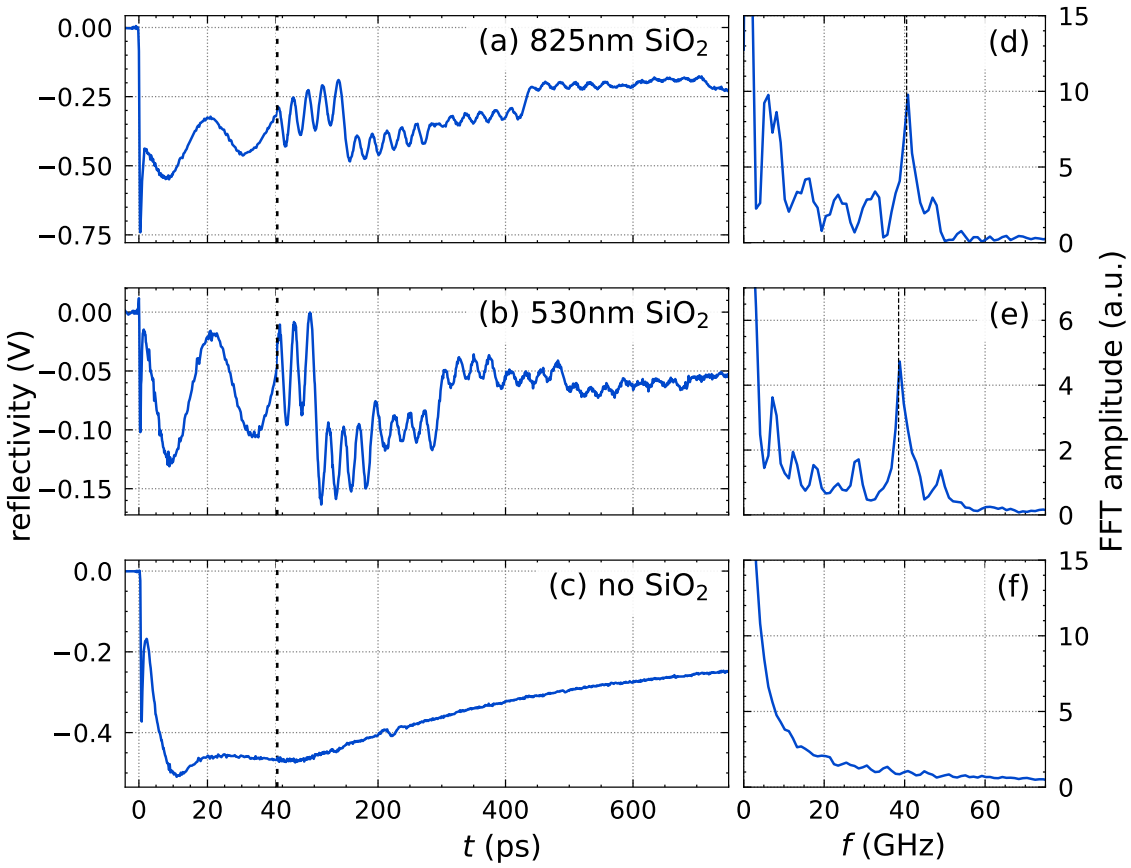

Figure 42: Transient reflectivity (a-c) and their FFT (d-f) for all three thick $TbFe_2$ samples at $F = 10\,\mathrm{mJ/cm^2}$.

5.2.5 Extracting the strain contribution to the trMOKE signal

In highly magnetostrictive materials, one expects a significant contribution of the strain to the trMOKE signal via inverse magnetostriction, i.e. a change of the magnetization by strain. If propagating strain pulses affect the trMOKE response it is expected that the quasi static strain that arises due to a near surface expansion of the thin film also contributes to the signal. However, this effect occurs at the same time as the laser-induced demagnetization and following remagnetization. By calibrating the strain amplitude using the peaks in the trMOKE response, which are a pure strain signal, the quasi-static strain contribution can also be estimated.
Modelling the amplitude of the propagating strain pulses using the udkm1dsim toolbox allows to infer the quasi static strain amplitude in the near surface region. For this the observed strain $\eta(t)$ is extracted from the strain map $\eta(z,t)$,by averaging the strain within the probed sample region. If an exponential decay profile for the probe beam is assumed, the observed strain can be calculated as the weighted average in

the $TbFe_2$ layer between d_1 and d_2:

$$\eta(t) = \int_{d_1}^{d_2} \eta(z,t) \mathrm{e}^{-z/z_0} \, \mathrm{d}z. \tag{67}$$

The penetration depth z_0 of the probe beam determines the shape of the strain signal, a higher value causes a smoother curve as the strain is averaged over a larger area. A value of $z_0 = 30\,\mathrm{nm}$ was found to produce the best fitting results to the MOKE signal. For the capped samples, the averaged strain is now scaled so that the peaks in the signals match. For this, the background signal for MOKE and strain is removed first by subtracting a strongly smoothed version of the same signal. That way only the strain peaks are present in the two signals and they can be directly compared. The `differential_evolution` algorithm from the `scipy` package is used to minimize the squared absolute difference between MOKE and strain:

$$\min_x \left\{ \sum_t \left| [\mathrm{MOKE} - \mathrm{MOKE}_{\mathrm{bkg}}](t) - x \cdot [\eta - \eta_{\mathrm{bkg}}](t) \right|^2 \right\}. \tag{68}$$

When the resulting signals are compared, the strain peaks still appear sharper than the peaks in the MOKE signal, so the signal is smoothed to attenuate high frequencies. This frequency dependent damping of strain waves follows a power law $\propto \omega^n$ ($n = 2$ to 4) [21]. A slow magneto-acoustic response would also broaden the strain peaks in the trMOKE signal. For simplicity a simple Gaussian filter is used here which still gives the desired result. Its standard deviation σ is also optimized through the `differential_evolution` algorithm, so the minimization returns the two parameters x (scaling factor for η) and σ (broadening of η). For the 825 nm and 530 nm capping thickness samples the following values were obtained:

$$\begin{aligned} x &= 13.4, \\ \sigma &= 4.5\,\mathrm{ps} \text{ and} \\ x &= 6.0, \\ \sigma &= 3.9\,\mathrm{ps}. \end{aligned}$$

The results of the optimizations can be seen in Figure 43 and 44. After 200 ps, the signals are almost completely described by the quasi-static strain, however there is still a small negative signal present. This is expected, as the quasi-static strain is caused by a high temperature in the magnetic layer, which should also cause some amount of demagnetization. The initial dynamics are dominated by ultrafast demagnetization and following remagnetization, which can be fitted with a single exponential decay with a time constant $\tau = 33\,\mathrm{ps}$ and $\tau = 16\,\mathrm{ps}$ for the 825 nm and 530 nm capping. This value is strongly fluence dependent, as the corresponding feature in the trMOKE signal slows down significantly with higher excitation fluences (compare Figure 40). Interestingly, the strain-subtracted signals now looks very similar to the $Tb_{0.3}Dy_{0.7}Fe_2$ signal, especially regarding the remagnetization timescale (compare Figure 32 and Table 5). This hints at a strong connection between magnetostriction and magnetocrystalline

anisotropy, as the signal without strain looks like the signal of the sample with the lowest anisotropy.

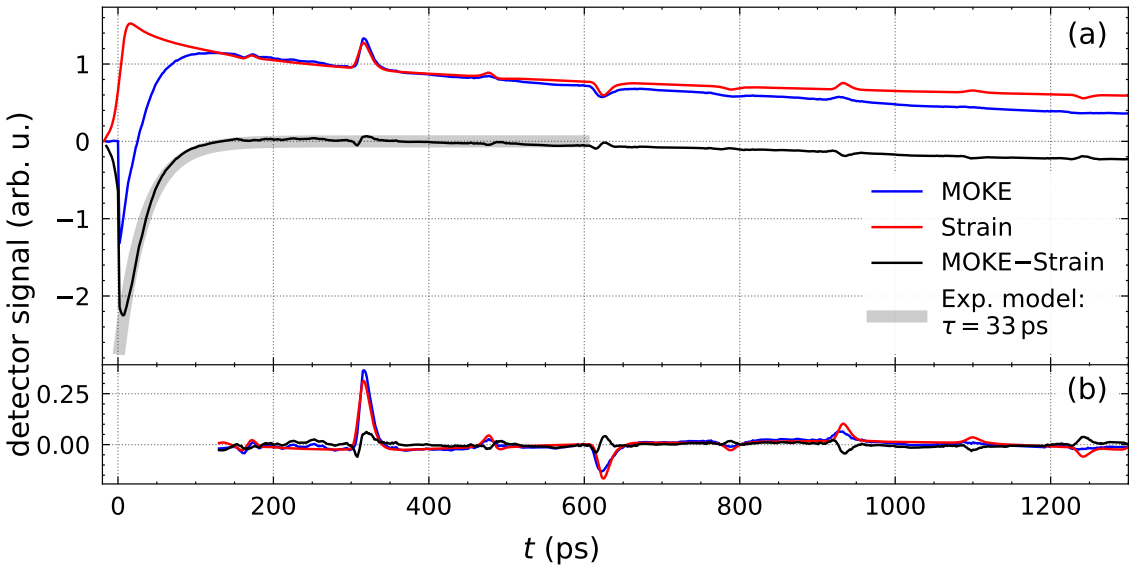

Figure 43: Extracted strain contribution to the MOKE signal of 825 nm glass-capped $TbFe_2$. The upper panel shows the MOKE and scaled+smoothed strain signals and their difference. The lower panel shows the same, but for the background subtracted signals. The remaining difference can be fitted with a single exponential decay ($\tau = 33\,\mathrm{ps}$).

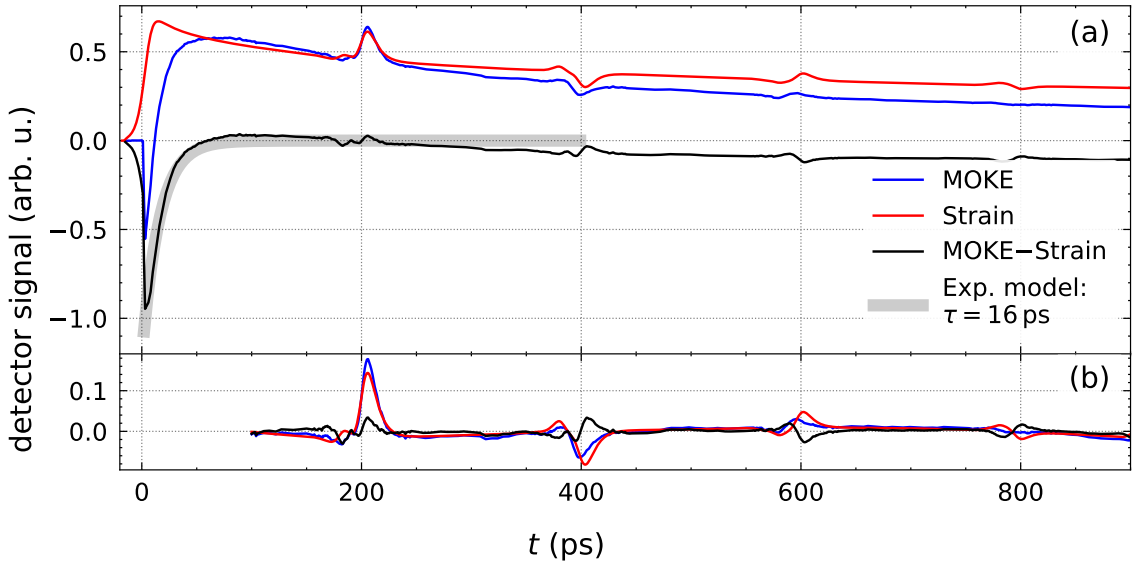

Figure 44: Extracted strain contribution to the MOKE signal of 530 nm glass-capped $TbFe_2$. Like before, the remaining difference between strain and MOKE can be fitted with a single exponential decay ($\tau = 16$ ps).

5.3 Summary out-of-plane field measurements

The main goal of this measurement series, finding the demagnetization timescales for the different $REFe_2$ compounds, is more complicated than expected. Oftentimes multiple features occur within the first few picoseconds, with varying timescales, making it difficult to unequivocally identify the demagnetization timescale. A possible explanation could be different demagnetization timescales for the RE and Fe sublattices, leading to complex behavior when one sublattice demagnetizes faster than the other. This principle is for example used in the all-optical switching of GdFeCo [45]. Different probe wavelengths to tune the MOKE sensitivity to either the RE or the Fe sublattice, or element-specific measurement techniques such as XMCD could be used in the future to better understand the observed dynamics. Also alternate MOKE geometries like LMOKE could lead to further insights, because of the lower saturation fields along the in-plane easy axes. This would simplify the interpretation of the signals by a well defined initial state of the magnetization direction.
At low fluences the thin $TbFe_2$ and $DyFe_2$ samples show opposing signs, likely due to their different magnetocrystalline anisotropies. In $Tb_{0.3}Dy_{0.7}Fe_2$, where the Tb and Dy anisotropy contributions compensate each other, the magnetization response recovers much faster. This is contradicted by reflectivity measurements showing that thermal energy transport and its concomitant remagnetization should happen over similar timescales for all three materials. So it is likely that the faster remagnetization is just a compensation effect of the two opposing rare earth element signals.
The MOKE signals for the thick $TbFe_2$ samples show the same initial dynamics as the

thin samples, but much more pronounced and with an opposing sign. Especially for the capped samples, the echoes of strain pulses at the $TbFe_2$ surface appear prominently in the MOKE signal, and their timing, shape and sign can be explained from strain simulations. By scaling the strain peaks to the peaks in the MOKE signal, it is shown that a significant part of the total MOKE signal is caused by both coherent strain waves and quasi-static strain. The remaining signal is almost completely described by a single exponential decay with a strongly fluence dependent time constant that is on the order of $\tau = 33\,\mathrm{ps}$ and $\tau = 16\,\mathrm{ps}$ for the 825 nm and 530 nm capping respectively.

6 Measurements with varying external field direction

The large magnetostriction of the Rare Earth Iron compounds motivates the search for strain induced magnetization precession. This chapter investigates the conditions for observing precession and the angle dependence of the precession frequency using a rotatable permanent magnet setup. When the external field is tilted, the effective magnetic field and the magnetization vector are no longer collinear upon ultrafast excitation. This misalignment is necessary for precession, as dictated by the mathematical structure of the Landau-Lifshitz-Gilbert (LLG) equation, specifically the cross product $\vec{M} \times \vec{H}_{\text{eff}}$. In the cases of purely out-of-plane or in-plane fields ($\theta_{\text{ext}} = 0°$ or 90°) this condition is not always met. Beginnings of a precession were already observed in the previous chapter 5 with the electromagnet (external field at 0°) in thin $TbFe_2$ and $DyFe_2$ films. This effect may have arisen from imperfect alignment, where the magnetic field was not perfectly normal to the sample surface, or from the contribution of a cubic magnetocrystalline anisotropy that introduces a non-normal component to the effective field. For the thick samples, it is first tested whether precession can be observed at all under rotated external fields and then examined if strain echoes can be used to resonantly enhance the precession at certain external field angles. However, this is more challenging due to the higher magnetocrystalline anisotropy in the thick samples, which requires significantly higher saturation fields.

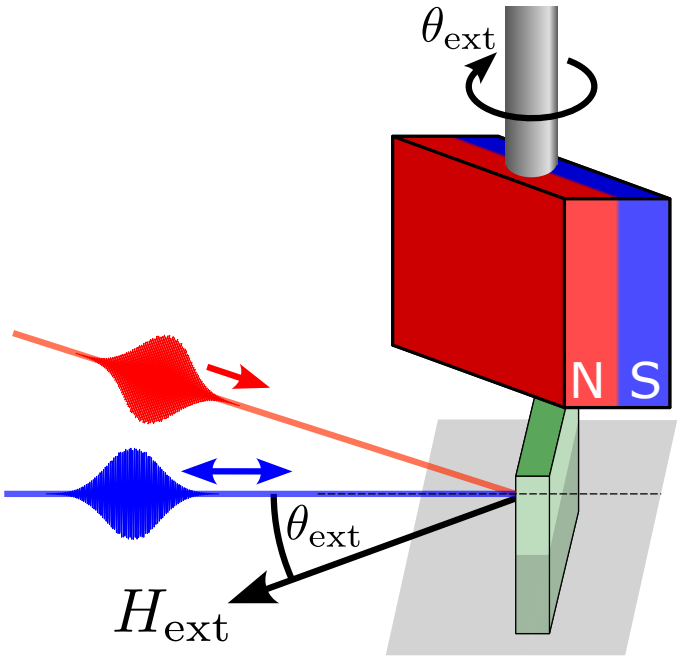

Figure 45: Schematic of the measurement geometry when using the rotatable permanent magnet setup. The angle of the external field θ_{ext} is set by rotating the permanent magnet.

6.1 Thin $REFe_2$ films under varying field directions

As in the previous chapter, the thin specimen are used to explore the intrinsic magnetization response of the three available materials, with a focus on the precession dynamics, if present.

6.1.1 Comparison between different $REFe_2$ materials

To identify the optimal conditions for precession in the three thin samples, their trMOKE response for several field angle directions is measured. Based on the electromagnet measurements, low fluences are necessary to observe any precession, so a value of $F = 3\,\text{mJ/cm}^2$ is used for all measurements. Typically, a full rotation series spanning 360° is measured in 10° steps, and opposite angle pairs (e.g. 20° and 200°) are subtracted to extract the field-dependent trMOKE signal. The remaining datasets cover the field angle range from 0° to 180° and exhibit a symmetry around 90°, so for example the signals for 20° and 160° differ only in their sign. For simplicity, only data for 0° to 90° are presented here.
Applying a tilted external field causes a clear precession in the thin $TbFe_2$ and $DyFe_2$ samples, but not in $Tb_{0.3}Dy_{0.7}Fe_2$, as shown in Figure 46. Noticeably, the signal signs of $TbFe_2$ and $DyFe_2$ are inverted, and while the precession frequencies are similar,

they are approximately 180° out of phase. This supports the hypothesis that the signal of $Tb_{0.3}Dy_{0.7}Fe_2$ consists of opposing contributions from Tb and Dy, resulting in a trMOKE signal without any observable precession.

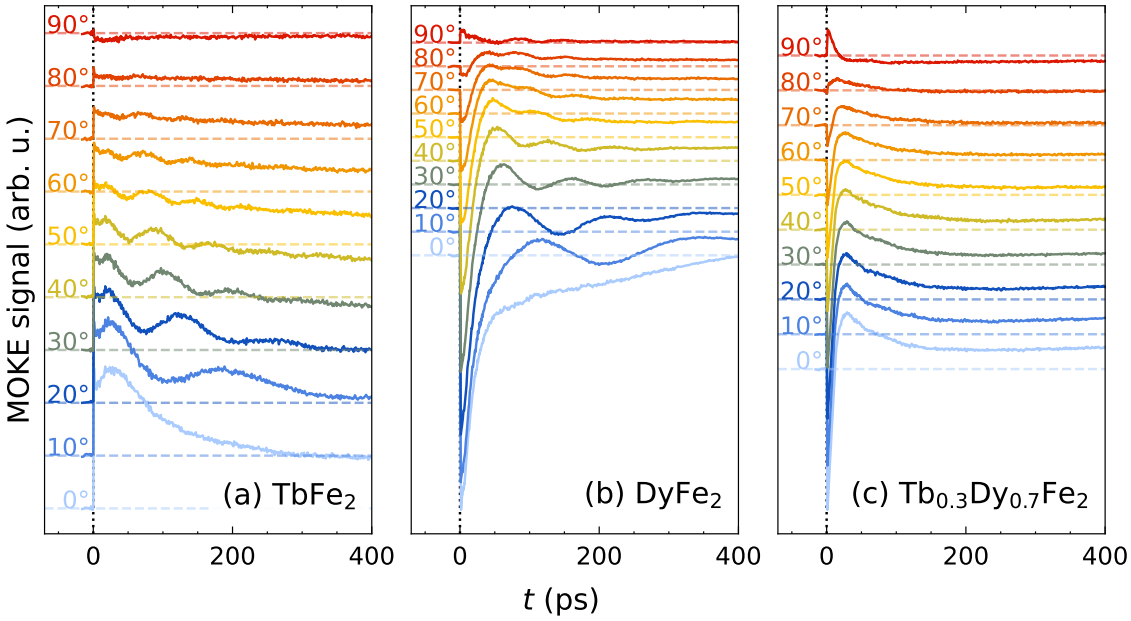

Figure 46: Comparison of the field angle dependent trMOKE measurements for the thin $REFe_2$ samples, showing that only $TbFe_2$ (a) and $DyFe_2$ (b) exhibit a precession. The measurements were performed with a pump fluence of $F = 3\,\mathrm{mJ/cm^2}$ and an external field of $\approx 350\,\mathrm{mT}$ at varying rotational angles. The displayed data is cut to 400 ps.

The Fourier transform of the trMOKE signals (Figure 59 in the Appendix) clearly shows the already discussed symmetry around 90°. The angle dependence of the precession frequency is also observed for $TbFe_2$ and $DyFe_2$, with frequencies increasing from 5 GHz to 15 GHz as the external field is rotated towards the in-plane direction. The peak of the precession in the FFT can be fitted to provide more precise values for the precession frequency and amplitude, as presented in Figure 47. This fitted peak consists of a Gaussian on a split-Lorentzian background (a Lorentzian with different widths on each side of the peak) and a Gaussian fixed at 0 GHz. The positions of the first two fitting functions are constrained to be identical. The total peak amplitude is the sum of the individual amplitudes of the Gaussian and split-Lorentzian. The third Gaussian accounts for the strong background signal at low frequencies, improving the accuracy of the fit.

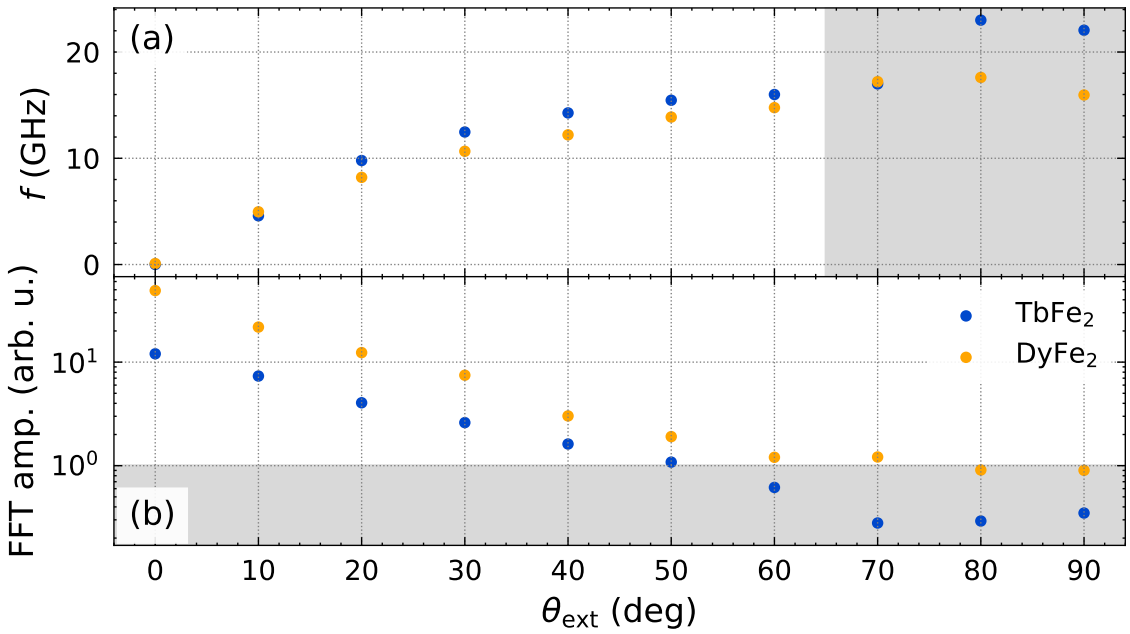

Figure 47: Extracted precession frequencies (a) and amplitudes (b) for $TbFe_2$ and $DyFe_2$, plotted against the external field angle. As the external field is tilted further towards the in-plane direction, the precession frequency increases and the precession amplitude drops. The gray shaded area marks the sensitivity limit where the peak amplitude is too small for an accurate fit.

The precession frequencies of both materials change similarly with the external field angle, with $DyFe_2$ showing a slightly lower frequency. At high field angles approaching 90°, the values differ significantly, likely because the field precession amplitude is below the sensitivity limit. The peak amplitudes drop by almost two orders of magnitude with increasing external field angles. For an out-of-plane field, no precession is observed, and the peak in the FFT is due to the superimposed slow background signal.
In conclusion, precession is only observed in $TbFe_2$ and $DyFe_2$ at low fluences. Larger external field angles result in higher precession frequencies but lower amplitudes, with angles between 10° and 30° showing the largest precession amplitude.

6.1.2 Fluence dependence of the precession

In this section, the fluence dependence of the precession is examined. A regular fluence series is measured with the external field fixed at an angle of 20° for the $DyFe_2$ sample and the resulting data are displayed in Figure 48. This corroborates the finding that precession only occurs in the low fluence regime below $7\,\mathrm{mJ/cm^2}$ that was seen with an out-of-plane field. Higher pump fluences eventually damage the pumped sample region, as evident from the reduced signal amplitude at $F = 11\,\mathrm{mJ/cm^2}$.

Unfortunately this measurement series suffers from a double excitation, causing a second demagnetization feature after 10 ps, only observed in this experiment series. However, since the delay between the excitations is significantly shorter than the precession timescales, this does not affect the general trend.

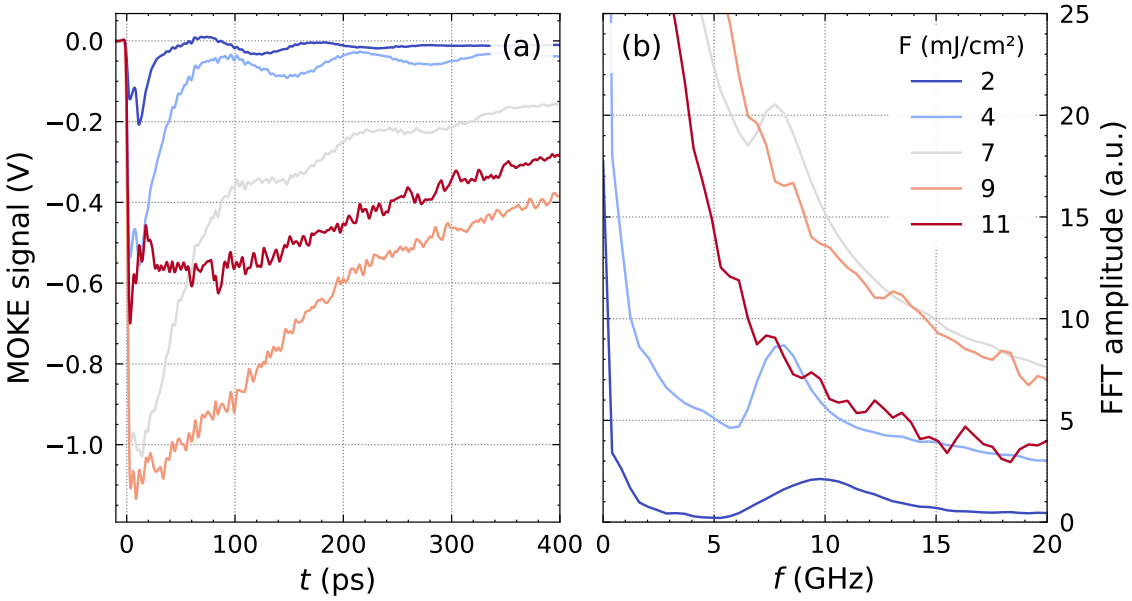

Figure 48: Fluence dependence of the precession in the trMOKE signal of $DyFe_2$, measured at an external field angle of 20°. The precession frequency and amplitude drop as the fluence is increased, with demagnetization getting more and more dominant. At the highest fluence $F = 11\,\mathrm{mJ/cm^2}$, the sample starts to degrade, causing a lower signal amplitude.

6.1.3 Modeling the FMR precession in $TbFe_2$ and $DyFe_2$

The results of the fluence series can be rationalized using a simple model. In classical electrodynamics, the torque $\vec{\tau}$ acting on the magnetization $\vec{M}$ in an external field $\vec{B}$ is given by:

$$\vec{\tau} \propto \vec{M} \times \vec{B}. \tag{69}$$

Therefore, a smaller magnetization results in a lower torque and, consequently, a lower precession frequency [11, 15]. This is inline with the observation that higher fluences lead to a reduction in precession frequency because the magnitude of the magnetization vector shrinks. At high fluences, the demagnetization dominates the signal, and no precession is observed above $F = 9\,\mathrm{mJ/cm^2}$.

A standard approach to model the ferromagnetic resonance (FMR) precession frequency from the free energy is through the Smit-Beljers-formalism. This is achieved by linearizing the LLG in spherical coordinates around the equilibrium position for a given external field [54, 5]. With this approach, the precession frequency mainly

depends on the curvature of the free energy surface:

$$f = \frac{1}{2\pi}\sqrt{\frac{\gamma^2}{M_S^2 \sin^2\theta}\left[\frac{\partial^2 F}{\partial\theta^2}\frac{\partial^2 F}{\partial\varphi^2} - \left(\frac{\partial^2 F}{\partial\theta\partial\varphi}\right)^2\right]}, \tag{70}$$

where $\gamma = 28\,\mathrm{GHz/T}$ is the electron gyromagnetic ratio. This method provides insights into magnetization dynamics without explicitly solving the full time-dependent LLG equation. Numerical methods are employed to determine the equilibrium magnetization and the free energy curvature.
The partial derivatives are evaluated at the eqilibrium position of the magnetization, which corresponds to the free energy minimum. The complexity increases if the free energy surface has multiple minima, as in the $REFe_2$ samples with their strong cubic magnetocrystalline anisotropies. Simulation results can vary based on the initial conditions, specifically the chosen minimum as the initial equilibrium state. For the simulations presented here, one of the in-plane minima of the free energy is selected and the simulation applies an external field in the in-plane direction. In an iterative process, the external field is now incrementally tilted out-of plane, and the new equilibrium magnetization is calculated by minimizing the free energy, using the previous equilibrium position as the starting point. With Equation 70, the precession frequency is then calculated for each equilibrium magnetization orientation. Using the literature values for $TbFe_2$ from Table 2, the results shown in Figure 49 are obtained. Due to the large magnetocrystalline anisotropy, the magnetization always stays close to the global in-plane minimum, regardless of the angle of the external field. The resulting frequencies above 500 GHz from the Smit-Beljers-formalism do not match the experimental data, as they are almost two orders of magnitude too high. Similar results are obtained for $DyFe_2$, despite the different magnetocrystalline anisotropy, which are presented in the Appendix.

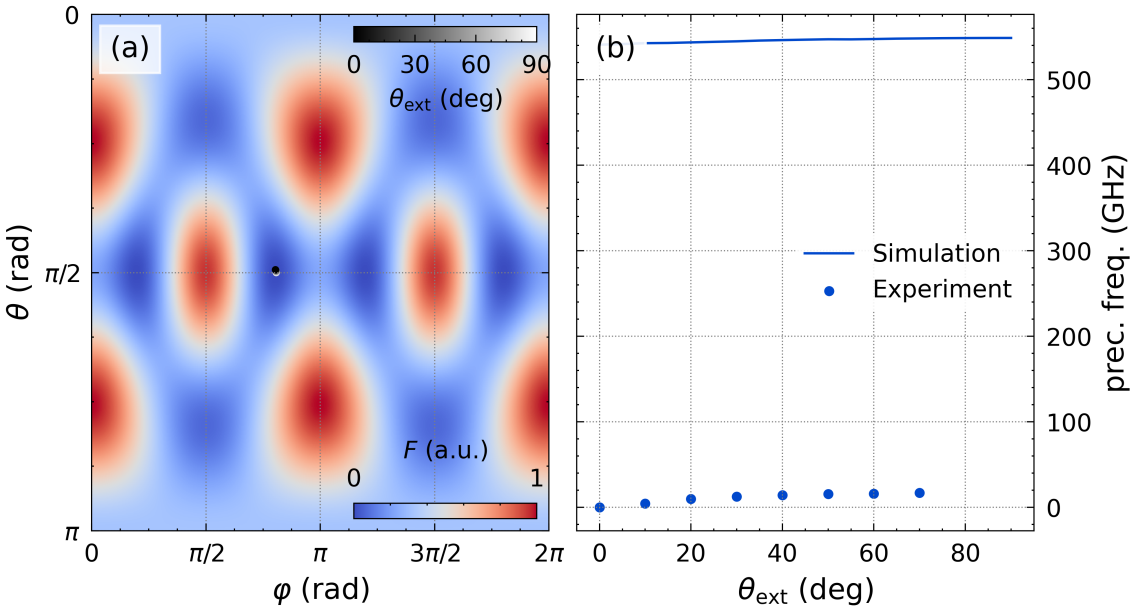

Figure 49: (a): Simulation results for the free energy surface of $TbFe_2$ without an external field, plotted here as a 2D map. The theta and phi coordinates of the equlibrium magnetization for different external field angles between 0° and 90° at a field strength of 350 mT are indicated as greyscale dots. From the simulation follows that with the available external field the magnetization always stays close to the initial equilibrium position. (b): This results in very high frequencies above 500 GHz, which were not observed during the experiments.

However, the experimental results can be modeled accurately if the cubic magnetocrystalline anisotropy parameters K_1 and K_2 are drastically reduced. With a reduction by a factor of $\lesssim 10^{-3}$ ($K_1 = 1.1 \cdot 10^4\,\mathrm{J/m^3}$, $K_2 = 1.9 \cdot 10^3\,\mathrm{J/m^3}$), the precession frequencies calculated using the Smit-Beljers formalism match the measured values, as presented in Figure 50. In this case, the shape anisotropy $F_S = 4.0 \cdot 10^5\,\mathrm{J/m^3}$ dominates the free energy, and the remaining magnetocrystalline anisotropy serves as only a minor perturbation. This reduction also explains why $TbFe_2$ and $DyFe_2$ have such similar precession frequencies, as their key difference lies in their magnetocrystalline anisotropy. The reduction of the anisotropy parameters is justified by the assumption that poor crystallinity in the $REFe_2$ layer grown on niobium causes a lower magnetocrystalline anisotropy [37]. Static MOKE data (Section 4.3) supports this for the thin $TbFe_2$ and $DyFe_2$ samples. Based on the magnitude of the reduced anisotropy parameters, Terfenol-D should also exhibit a precession, albeit at higher frequencies due to slightly larger K_1 and K_2 values. However, this is not observed in the experiment, likely due to the assumed compensation effect between Tb and Dy contents.

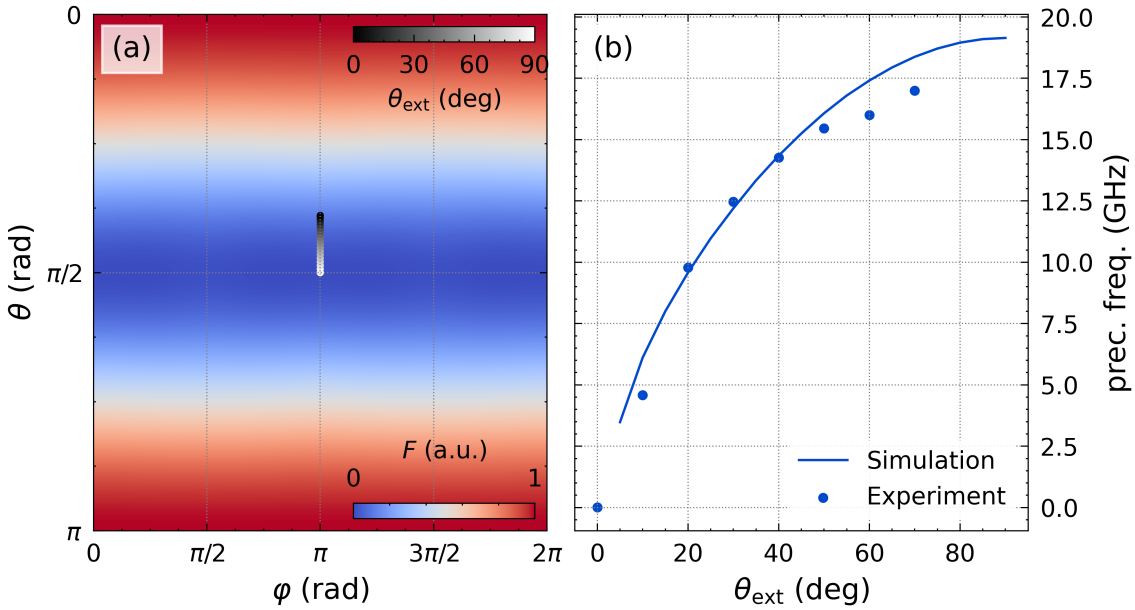

Figure 50: (a): Simulation results for the free energy surface of $TbFe_2$, but this time the cubic magnetocrystalline anisotropy parameters $K_{1,2}$ were scaled down by a factor of 1/1000. (b): The resulting precession frequencies are in agreement with the measured values.

6.2 Thick $TbFe_2$ films under varying field directions

As in the previous section, the trMOKE response of the thick samples is also measured under rotated external fields. In addition to the ultrafast demagnetization and the creation of quasi-static strain, the periodic arrival of strain echoes could serve as an additional mechanism driving the precession. All these processes are characterized by an ultrafast change of the effective field, initiating the magnetic precession around the new field direction. But while the first two mechanisms only provide an initial torque, the strain echoes deliver multiple torques over time, which may overcome the damping and thus sustain the precession for much longer. When the frequency of the strain pulses matches the precession frequency, a resonant enhancement of the precession is expected. Since the strain pulse frequency is fixed by the capping thickness, the angle of the external field can be used to set the matching precession frequency.

6.2.1 Fluence and angle dependent measurements of the uncapped sample

The trMOKE response of the uncapped $TbFe_2$ sample under rotated external fields should represent the intrinsic precession pattern in the thick films, without the influence of strain echoes. A pump fluence series is measured at external field angles of 20°,

45° and 80° (Figure 51). Unlike the thin specimen, no precession is observed under any experimental condition. At ≈ 230 ps, the strain signal already measured with the out-of-plane field appears in the magnetization response. The angle of the external field mainly changes the signal amplitude, as the magnetization is forced in-plane for higher angles.
The absence of precession may be explained by the higher magnetocrystalline anisotropy in the thick samples. It is known for this type of sample growth, that the probed surface region in thick $TbFe_2$, far away from the Nb layer, has a much better crystallinity [37], potentially leading to increased anisotropy parameters and stronger damping. As indicated by the simulations presented in Figure 49, larger anisotropy results in very high precession frequencies, which are likely to be strongly damped.

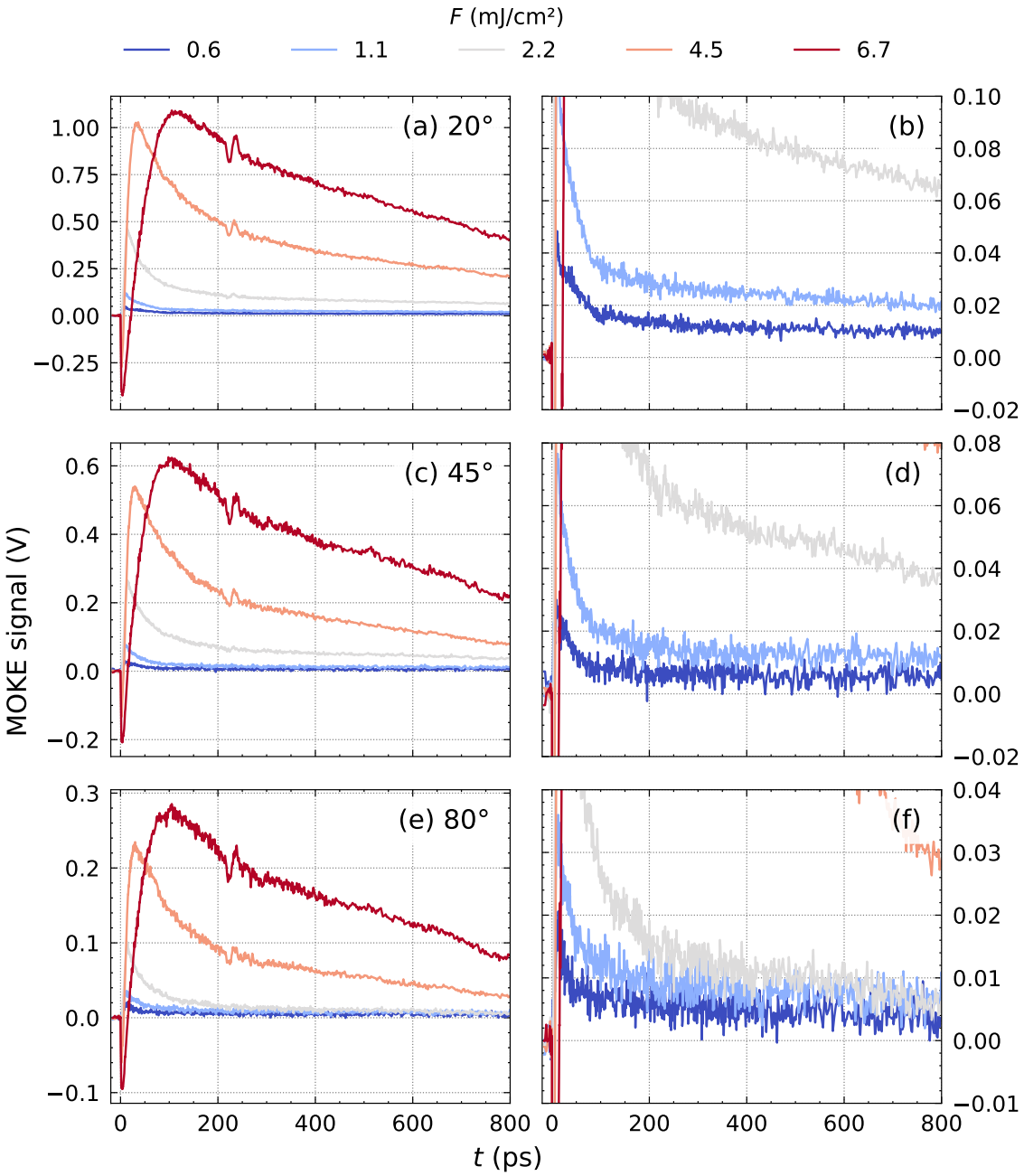

Figure 51: Fluence series of uncapped $TbFe_2$ with the external field of $\approx 350\,\mathrm{mT}$ at 20° (a, b), 45° (c, d) and 80° (e, f). The right column (b, d, f) shows an enlarged view of the small signals at low fluences. No precession is observed under any condition tested here.

6.2.2 Fluence dependent measurements of the capped samples

Based on the measurements with the thin samples, the expected precession frequencies range from 5 to 15 GHz. Thus, the 530 nm capped sample, with a strain pulse repetition rate of 5.1 GHz, is best suited for this experiment. Figure 47(a) indicates that for $TbFe_2$, the corresponding external field angle lies between 10° and 20°. The trMOKE signal continues to display the strong strain pulses previously observed with a normal external field (see Section 5.2), but once again, no precession is detected with the external field at 20° (Figure 52).
This suggests two possible explanations: either the strain pulses cause a fast and strongly damped precession, where the magnetization merely follows the change of the effective field due to the strain, or the strain signatures in the trMOKE signal are just a result of of the strain modifying the magneto-optical constants. In the latter case, the magnetization vector remains unchanged, and only the amount of magneto-optical signal, i.e. polarization rotation, varies. These effects are discussed in more detail in the next section.

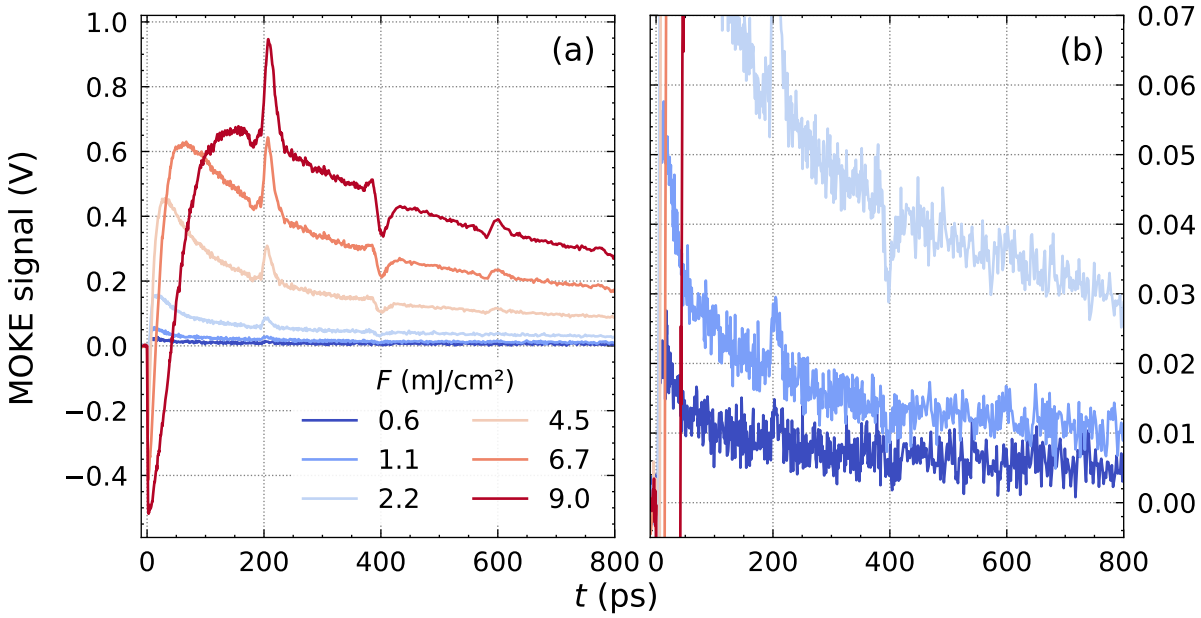

Figure 52: Fluence series of 530 nm glass capped $TbFe_2$ with the external field of ≈ 350 mT at 20°. The right panel (b) is an enlarged version of the left panel (a) to enhance the visibility of the small fluence measurements. Like with the uncapped sample no precession is observed under any condition, despite the strong strain pulse signatures.

6.2.3 Magneto-acoustic vs magneto-optic origin of the strain signals

The absence of any precession in the thick $TbFe_2$ samples raises the question of whether the observed strain signatures in the trMOKE signal S_{MOKE} are actually caused by a changing magnetization m_z (magneto-acoustic) or by a modification of the magneto-optical constants C_{MO} due to strain [51]:

$$S_{\mathrm{MOKE}}(\eta) = C_{\mathrm{MO}}(\eta) \cdot m_z(\eta). \tag{71}$$

If only the magneto-optical constants were changing, this would explain why no precession is observed. One way to distinguish between these two possibilities is by comparing their respective timescales. The modification of the magneto-optical constants should instantly follow the strain, while the rate of change of the magnetization is limited by the LLG equation. Therefore, a magneto-acoustic response should in principle exhibit a longer timescale than a purely magneto-optical one.
The transient reflectivity measures the instantaneous change of the refractive index n due to strain. By comparing the strain features in the transient reflectivity with trMOKE, a magneto-optic origin can be ruled out if the strain features in trMOKE are significantly longer. This comparison is only possible for the uncapped $TbFe_2$ sample, as the glass capping introduces strong Brillouin oscillations in the reflectivity signal, making it challenging to extract the strain pulses. The results are presented in Figure 53(a-b), showing two bipolar strain pulses, that arrive from the $TbFe_2$-Nb and Nb-Al_2O_3 interfaces, with a separation of $\approx 30\,\mathrm{ps}$ (compare with the strain map in Figure 39(a)).
To improve the comparison between both strain signals, several processing steps are performed: First, their time-zero is aligned and the background is subtracted to extract the strain pulses. The reflectivity signal is then inverted and scaled to match the MOKE signal. The signals are then smoothed with a 2 ps Gaussian filter to reduce noise. The two resulting signals are almost identical, but shifted by 5 ps. The shift is determined by finding the maximum position of the cross-correlation of the two signals. These findings suggest a magneto-acoustic origin of the strain signals, as the shift can be explained by a delayed response of the magnetization to a quasi-instantaneous change of the effective field, governed by the LLG equation. The very high anisotropy in thick $TbFe_2$ might also cause strong damping of the precession, which suppresses any fast oscillation.

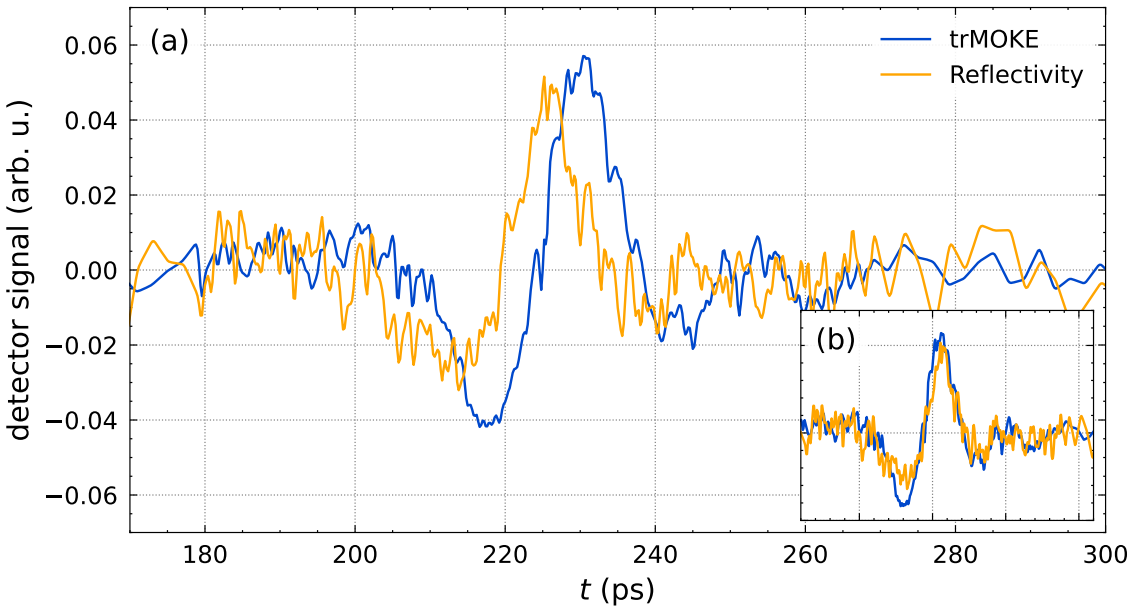

Figure 53: Comparison of the strain pulse in background-subtracted MOKE and reflectivity signals, both measured with a pump fluence of $F = 10\,\mathrm{mJ/cm^2}$. The reflectivity signal was inverted and scaled to match the MOKE signal, and both signals were smoothed with a 2 ps Gaussian filter. A shift in time by about 5 ps between the two signals is observed (a). The inset (b) shows that both signals are almost identical if the shift is removed. This can be explained by a magneto-acoustic driving mechanism below resonance.

6.3 Summary rotated field measurements

This measurement series confirms that a precession is present in the thin $TbFe_2$ and $DyFe_2$. The precession patterns are very similar for the two materials, with frequencies ranging from 5 to 15 GHz. While the precession frequency rises with the external field angle, the amplitude significantly decreases. Another observation is the opposing signal signs of the two materials, and their almost 180° shifted precession phases. In contrast, Terfenol-D exhibits no precession, and its trMOKE response resembles a superposition of the $TbFe_2$ and $DyFe_2$ signals. This supports the hypothesis that the opposing signal contributions from Tb and Dy cancel out the precession in the resulting trMOKE signal.
The precession frequencies are also calculated from the free energy with the Smit-Beljers-formalism. Using the literature values for the cubic magnetocrystalline anisotropy constants, very high frequencies above 500 GHz are predicted. This discrepancy is resolved by drastically reducing the magnitude of the anisotropy parameters by a factor of 10^{-3}. It is assumed that observed poor monocrystalline growth of the $REFe_2$ layer directly above the Nb causes this reduction of magnetocrystalline anisotropy. This

effect is particularly relevant in the thin specimen as the entire 20 nm film is affected by the poor crystallinity.
In the thick samples, this region is far away from the probed surface layer, so better crystallinity and higher magnetcrystalline anisotropy are expected. This may explain why no precession is observed for the thick $TbFe_2$ samples, as higher anisotropy could lead to higher damping. Additionally, even if the precession would not be strongly damped, the simulated frequencies above 500 GHz cannot be resolved with the 1 ps sampling rate used in most experiments. In the capped specimen, strain pulse signatures were detected again. However, no precession is observed again, as the strain pulses drive the magnetization well below the resonance frequency. The resulting magnetization dynamics follow the strain dynamics with a small delay. A comparison of reflectivity and trMOKE data suggests a shift of 5 ps, which is explained as an intrinsic delay set by the LLG equation.

7 Conclusion and outlook

7.1 Conclusion

Transient MOKE measurements were performed on the three highly magnetostrictive rare earth-iron compounds $TbFe_2$, $DyFe_2$ and $Tb_{0.3}Dy_{0.7}Fe_2$. These experiments encompassed:

- Quasi-static precharacterization with MOKE and XRD,
- Exploration of the intrinsic demagnetization timescale in thin $REFe_2$ films upon femtosecond laser excitation,
- Observation of inverse magnetostriction effects in the time-domain in thick $TbFe_2$ structures, and
- External field angle dependence of the precession in thin and thick $REFe_2$ samples.

Thin $REFe_2$ films allow almost homogeneous probing of the intrinsic magnetization response upon ultrafast laser excitation. The trMOKE signals displayed distinct differences among the three materials, with multiple features and timescales within the first few picoseconds. Each sample exhibits an initial ultrafast demagnetization response on a sub-picosecond timescale, followed by a delayed and slower second and sometimes third response. This behavior likely arises from the interplay between different demagnetization timescales of the RE and Fe sublattices and temperature-dependent anisotropies. Notably, the trMOKE signal signs for $TbFe_2$ and $DyFe_2$ are opposite at low fluences, which I linked to their opposing magnetocrystalline anisotropies. I also observed a large difference in the remagnetization timescales, where Terfenol-D recovers more than three times faster than $TbFe_2$ and $DyFe_2$. This was attributed to a compensation effect in $Tb_{0.3}Dy_{0.7}Fe_2$, where the opposing anisotropies of the Tb and Dy contents lead to canceling signal contribution and thus an apparently faster recovery. Transient reflectivity measurements support this conclusion, as they show that thermal transport takes place on similar timescales in all three materials.
For thick, glass-capped $TbFe_2$ samples, the delayed arrival of strain echoes enabled the separation of strain responses from the initial non-equilibrium magnetization dynamics following laser excitation. I identified characteristic peaks in the trMOKE signal as unipolar strain pulses propagating through the glass capping and the $TbFe_2$ layer. The timing, shape and sign of these strain echoes was rationalized with strain simulations obtained from the udkm1dsim toolbox. By scaling the strain simulation signal to the strain peaks in the trMOKE signal, the total contribution of both coherent strain pulses and quasi-static strain to the magnetization response was quantified. I demonstrated that the trMOKE signal beyond 200 ps can be rationalized by the

magneto-elastic contribution thar arises from quasi-static strain in the probed sample region.
Under oblique external fields, strong precession signals were observed in thin $TbFe_2$ and $DyFe_2$ films, but not in thin Terfenol-D and thick $TbFe_2$. The precession frequencies range between 5 to 15 GHz, increasing with the external field angle. $TbFe_2$ and $DyFe_2$ exhibit similar frequency responses, but the signals are almost 180° out of phase and their signs are inversed. This suggests, similar to the demagnetization measurements, that the opposing Tb and Dy contributions cancel out the precession signal in Terfenol-D.
I demonstrated that reproducing the angle-dependent frequency response through the Smit-Beljers formalism requires a significant reduction the magnetocrystalline anisotropy constants by three orders of magnitude. This reduction is attributed to an inhomogeneous growth of the first 100 nm of the $REFe_2$ layer, which therefore affects the thin films much stronger. Static MOKE and XRD measurements further indicated structural differences between the thin and thick films, for example by the in-plane angle-dependence of the LMOKE hystereses, or broadened Bragg peaks.
The thick $TbFe_2$ samples exhibit the same unipolar strain signatures, however they neither initiate nor enhance the precession under any experimental condition tested. A larger anisotropy is expected in the probed near-surface region of the thick films due to the higher degree of crystallinity there. Simulations with the Smit-Beljers formalism using literature values for the magnetocrystalline anisotropy yielded high frequencies of several 100 GHz, which I did not observe in the experiments. If present, these high frequencies are likely strongly damped and thus difficult to measure. A comparison between trMOKE and transient reflectivity showed that the magnetization response follows the strain response with a delay of 5 ps. I attribute this delay to an intrinsic timescale of the magnetization response governed by the LLG equation.

7.2 Outlook

The experimental results obtained in this thesis highlight the important role of the large anisotropy for the magnetization dynamics in $REFe_2$ compounds. While the systematic variation of the magnetocrystalline anisotropy by changing the material and the sample structure revealed interesting trends, further investigations are required for a more complete understanding.
First of all, the current set of investigated sample structures is not exhaustive, lacking thick $DyFe_2$ and $Tb_{0.3}Dy_{0.7}Fe_2$ specimens comparable to thick $TbFe_2$ samples available. Including these samples would enable a direct comparison of trends related to thickness and thus crystallinity across all three materials. This would clarify whether the observed effects are specific to $TbFe_2$, or arise systematically from structural differences. Also some of the samples have been prepared many years ago and show significant damage, so measuring with fresh new samples would increase confidence in the reproducibility of the results.
All trMOKE experiments in this thesis were conducted in a polar geometry below

saturation, as the out-of-plane direction is a hard axis in [110]-orientated $REFe_2$ materials. This limits the informative value of the demagnetization measurements, as both a change of the angle and the length of the magnetization vector influences the trMOKE signal. Thus, by switching to a longitudinal geometry, where the saturation field is significantly lower, a clearer picture of the intrinsic demagnetization time of rare earth thin films is expected. Additionally, it was already shown that through an in-plane rotation of the sample, in-plane anisotropy can be mapped (comp. Figures 23 and 25). While limited to static experiments for now, extending these experiments into the time-resolved setup could provide further insight on how the anisotropy influences the ultrafast magnetization dynamics. With an LMOKE geometry, the suggested strain-driven in-plane switching in Terfenol-D by Kovalenko et al. [27] could also be observed, although the required strain pulse properties are idealized and might not be achievable in the experiment.
An alternative approach to changing the measurement geometry is to change the crystalline orientation of the sample. One possibility would be the use of [111]-oriented samples where the out-of-plane axis is an easy axis. Thus saturation might be achievable even in a PMOKE geometry.
Another promising approach are element-specific experiments. Based on Khorsand et al. [23], the current trMOKE setup with a 400 nm probe is primarily sensitive to the RE sublattice magnetization. With a longer wavelength, for example by switching pump and probe wavelengths, a sensitivity to the Fe sublattice would be achieved. Comparing the RE and Fe magnetization responses would help attributing some of the features observed in trMOKE to competing demagnetization between the two sublattices. More precise element specificity is achieved in the x-ray regime, for example in an XMCD experiment. There, even a selection between Tb and Dy is possible, and allows observing the potentially element-specific de- and remagnetization dynamics. This helps understanding the mechanisms behind the suggested compensation effects in Terfenol-D.
Finally, the idea of the glass capped sample structures, that allows to separate the effect of strain and heat in the time-domain could be extended to other magnetically ordered materials. While the absence of precession in thick $TbFe_2$ prevented a potential resonant amplification through periodic strain echoes in the glass capping, the same principle can be applied to the thin specimen, where a strong precession was observed. For example, with a capping thickness of ≈ 135 nm the strain pulse repetition rate matches the 10 GHz precession frequency observed under an external field angle of 20° to 25°. The general principle of resonant amplification of precession by unipolar strain echoes in a capping layer can also be extended to other magnetic materials. Ferromagnets like nickel, while lacking the giant magnetostriction of $REFe_2$ compounds, are better understood and exhibit a lower magnetocrystalline anisotropy. This would greatly simplify both modelling and measurements.

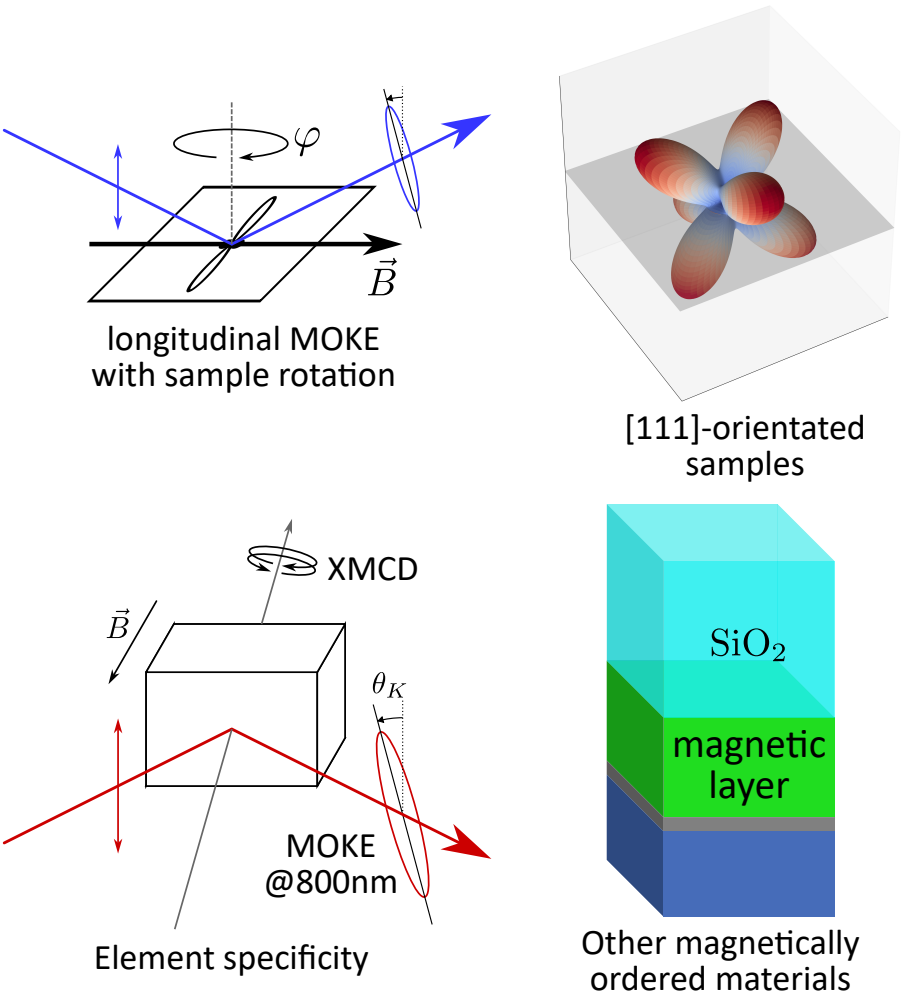

Figure 54: Overview of the ideas for future experiments, as discussed in the Outlook.

Bibliography

[1] S. Andersson and L. Dzhavadov. "Thermal Conductivity and Heat Capacity of Amorphous SiO_2: Pressure and Volume Dependence." In: *Journal of Physics: Condensed Matter* 4.29 (1992), p. 6209. DOI: 10.1088/0953-8984/4/29/005.

[2] S. D. Bader. "SMOKE." In: *Journal of Magnetism and Magnetic Materials* 100.1 (1991), pp. 440–454. DOI: 10.1016/0304-8853(91)90833-V.

[3] St. Burghartz and B. Schulz. "Thermophysical Properties of Sapphire, AlN and $MgAl_2O_4$ down to 70 K." In: *Journal of Nuclear Materials*. Fusion Reactor Materials 212–215 (1994), pp. 1065–1068. DOI: 10.1016/0022-3115(94)90996-2.

[4] E. Callen and H. B. Callen. "Magnetostriction, Forced Magnetostriction, and Anomalous Thermal Expansion in Ferromagnets." In: *Physical Review* 139 (2A 1965), A455–A471. DOI: 10.1103/PhysRev.139.A455.

[5] M. Cherkasskii et al. "Theory of Inertial Spin Dynamics in Anisotropic Ferromagnets." In: *Physical Review B* 106.5 (2022), p. 054428. DOI: 10.1103/PhysRevB.106.054428.

[6] A. Clark, R. Abbundi, and W. Gillmor. "Magnetization and Magnetic Anisotropy of $TbFe_2$, $DyFe_2$, $Tb_{0.27}Dy_{0.73}Fe_2$ and $TmFe_2$." In: *IEEE Transactions on Magnetics* 14.5 (1978), pp. 542–544. DOI: 10.1109/TMAG.1978.1059879.

[7] A. E. Clark and H. S. Belson. "Giant Room-Temperature Magnetostrictions in $TbFe_2$ and $DyFe_2$." In: *Physical Review B* 5.9 (1972), pp. 3642–3644. DOI: 10.1103/PhysRevB.5.3642.

[8] A. E. Clark, H. S. Belson, and R. E. Strakna. "Elastic Properties of Rare-earth-iron Compounds." In: *Journal of Applied Physics* 44.6 (1973), pp. 2913–2914. DOI: 10.1063/1.1662676.

[9] J. M. D. Coey. *Magnetism and Magnetic Materials*. Repr. Cambridge: Cambridge Univ. Press, 2013. 614 pp. ISBN: 978-0-521-81614-4.

[10] A. S. Cooper. "Precise Lattice Constants of Germanium, Aluminum, Gallium Arsenide, Uranium, Sulphur, Quartz and Sapphire." In: *Acta Crystallographica* 15.6 (1962), pp. 578–582. DOI: 10.1107/S0365110X62001474.

[11] W. Demtröder. *Experimentalphysik 1: Mechanik und Wärme*. Springer-Lehrbuch. Berlin, Heidelberg: Springer, 2015. ISBN: 978-3-662-46414-4 978-3-662-46415-1. DOI: 10.1007/978-3-662-46415-1.

[12] G. Engdahl. *Handbook of Giant Magnetostrictive Materials*. Electromagnetism. San Diego, CA: Academic Press, 2000. ISBN: 978-0-12-238640-4.

[13] P. Fumagalli and J. Schoenes. *Magneto-Optics*. De Gruyter, 2021. ISBN: 978-3-11-063530-0. DOI: 10.1515/9783110635300-202.

[14] D. J. Germano and R. A. Butera. "Heat Capacity of, and Crystal-Field Effects in, the $R\mathrm{Fe}_2$ Intermetallic Compounds (R =Gd, Tb, Dy, Ho, Er, Tm, and Lu)." In: *Physical Review B* 24.7 (1981), pp. 3912–3927. DOI: 10.1103/PhysRevB.24.3912.

[15] R. Gross and A. Marx. *Festkörperphysik*. De Gruyter Oldenbourg, 2014. ISBN: 978-3-11-035870-4. DOI: 10.1524/9783110358704.

[16] F. Habashi. "Niobium, Physical and Chemical Properties." In: *Encyclopedia of Metalloproteins*. Ed. by R. H. Kretsinger, V. N. Uversky, and E. A. Permyakov. New York, NY: Springer, 2013, pp. 1552–1554. ISBN: 978-1-4614-1533-6. DOI: 10.1007/978-1-4614-1533-6_384.

[17] T. A. Hahn et al. "Thermal Expansion of Fused Silica from 80 to 1000 K - Standard Reference Material 739." In: Proceedings of the 1971 Thermal Expansion Symposium. Corning, New York (USA), 1972, pp. 13–24. DOI: 10.1063/1.2948551.

[18] T. A. Hahn. "Thermal Expansion of Single Crystal Sapphire from 293 to 2000 K Standard Reference Material 732." In: *Thermal Expansion 6*. Ed. by I. D. Peggs. Boston, MA: Springer US, 1978, pp. 191–201. ISBN: 978-1-4615-9086-6. DOI: 10.1007/978-1-4615-9086-6_18.

[19] K. B. Hathaway and A. E. Clark. "Magnetostrictive Materials." In: *MRS Bulletin* 18.4 (1993), pp. 34–41. DOI: 10.1557/S0883769400037337.

[20] S. Hunklinger. *Festkörperphysik*. De Gruyter Oldenbourg, 2017. ISBN: 978-3-11-056775-5. DOI: 10.1515/9783110567755.

[21] A. Huynh et al. "Temperature Dependence of Hypersound Attenuation in Silica Films via Picosecond Acoustics." In: *Physical Review B* 96.17 (2017), p. 174206. DOI: 10.1103/PhysRevB.96.174206.

[22] D. C. Jiles and J. B. Thoelke. "Theoretical Modelling of the Effects of Anisotropy and Stress on the Magnetization and Magnetostriction of $\mathrm{Tb}_{0.3}\mathrm{Dy}_{0.7}\mathrm{Fe}_2$." In: *Journal of Magnetism and Magnetic Materials* 134.1 (1994), pp. 143–160. DOI: 10.1016/0304-8853(94)90086-8.

[23] A. R. Khorsand et al. "Element-Specific Probing of Ultrafast Spin Dynamics in Multisublattice Magnets with Visible Light." In: *Physical Review Letters* 110.10 (2013), p. 107205. DOI: 10.1103/PhysRevLett.110.107205.

[24] C. Kittel. "Model of Exchange-Inversion Magnetization." In: *Physical Review* 120.2 (1960), pp. 335–342. DOI: 10.1103/PhysRev.120.335.

[25] C. Kittel. "Physical Theory of Ferromagnetic Domains." In: *Reviews of Modern Physics* 21.4 (1949), pp. 541–583. DOI: 10.1103/RevModPhys.21.541.

[26] Yu. V. Knyazev and Yu. I. Kuz'min. "Optical Properties of YFe_2 and TbFe_2 Compounds." In: *Physics of the Solid State* 62.7 (2020), pp. 1132–1135. DOI: 10.1134/S1063783420070094.

[27] O. Kovalenko, T. Pezeril, and V. V. Temnov. "New Concept for Magnetization Switching by Ultrafast Acoustic Pulses." In: *Physical Review Letters* 110.26 (2013), p. 266602. DOI: 10.1103/PhysRevLett.110.266602.

[28] L. Le Guyader et al. "Dynamics of Laser-Induced Spin Reorientation in Co/$SmFeO_3$ Heterostructure." In: *Physical Review B* 87.5 (2013), p. 054437. DOI: 10.1103/PhysRevB.87.054437.

[29] W. Li et al. "Acoustically Assisted Magnetic Recording: A New Paradigm in Magnetic Data Storage." In: *IEEE Transactions on Magnetics* 50.3 (2014), pp. 37–40. DOI: 10.1109/TMAG.2013.2285018.

[30] D. Lide. "CRC Handbook of Chemistry and Physics, 84th Edition Edited." In: *Journal of the American Chemical Society* 126.5 (2004), pp. 1586–1586. DOI: 10.1021/ja0336372.

[31] I. H. Malitson. "Interspecimen Comparison of the Refractive Index of Fused Silica." In: *JOSA* 55.10 (1965), pp. 1205–1209. DOI: 10.1364/JOSA.55.001205.

[32] I. H. Malitson. "Refraction and Dispersion of Synthetic Sapphire." In: *JOSA* 52.12 (1962), pp. 1377–1379. DOI: 10.1364/JOSA.52.001377.

[33] C. Marceau et al. "Femtosecond Filament Induced Birefringence in Argon and in Air: Ultrafast Refractive Index Change." In: *Optics Communications* 283.13 (2010), pp. 2732–2736. DOI: 10.1016/j.optcom.2010.03.004.

[34] M. Mattern et al. "Concepts and Use Cases for Picosecond Ultrasonics with X-Rays." In: *Photoacoustics* 31 (2023), p. 100503. DOI: 10.1016/j.pacs.2023.100503.

[35] M. Mattern et al. "Towards Shaping Picosecond Strain Pulses via Magnetostrictive Transducers." In: *Photoacoustics* 30 (2023). DOI: 10.1016/j.pacs.2023.100463.

[36] M. J. Mehl et al. "The AFLOW Library of Crystallographic Prototypes: Part 1." In: *Computational Materials Science* 136 (2017), S1–S828. DOI: 10.1016/j.commatsci.2017.01.017.

[37] A. Mougin et al. "Strain in Single-Crystal $R\mathrm{Fe}_2(110)$ Thin Films (R = Y, Sm, Gd, Tb, $\mathrm{Dy}_{0.7}\mathrm{Tb}_{0.3}$, Dy, Er, Lu)." In: *Physical Review B* 59.8 (1999), pp. 5950–5959. DOI: 10.1103/PhysRevB.59.5950.

[38] A. Mougin et al. "Strain-Induced Magnetic Anisotropy in Single-Crystal $R\mathrm{Fe}_2(110)$ Thin Films ($R = \mathrm{Dy}, \mathrm{Er}, \mathrm{Tb}, \mathrm{Dy}_{0.7}\mathrm{Tb}_{0.3}$, Sm, Y)." In: *Physical Review B* 62.14 (2000), pp. 9517–9531. DOI: 10.1103/PhysRevB.62.9517.

[39] K. J. Palm et al. "Dynamic Optical Properties of Metal Hydrides." In: *ACS Photonics* 5.11 (2018), pp. 4677–4686. DOI: 10.1021/acsphotonics.8b01243.

[40] L. Pan and D. B. Bogy. "Heat-Assisted Magnetic Recording." In: *Nature Photonics* 3.4 (2009), pp. 189–190. DOI: 10.1038/nphoton.2009.40.

[41] T. Parpiiev et al. "Ultrafast Strain Excitation in Highly Magnetostrictive Terfenol: Experiments and Theory." In: *Physical Review B* 104.22 (2021), p. 224426. DOI: 10.1103/PhysRevB.104.224426.

[42] C. E. Patrick, G. A. Marchant, and J. B. Staunton. "Spin Orientation and Magnetostriction of $Tb_{1-x}Dy_xFe_2$ from First Principles." In: *Physical Review Applied* 14.1 (2020), p. 014091. DOI: 10.1103/PhysRevApplied.14.014091.

[43] H. Probst et al. "Unraveling Femtosecond Spin and Charge Dynamics with Extreme Ultraviolet Transverse MOKE Spectroscopy." In: *Physical Review Research* 6.1 (2024), p. 013107. DOI: 10.1103/PhysRevResearch.6.013107.

[44] J.-E. Pudell. "Ultraschnelle Magnetostriktion von Antiferromagnetischem Holmium." Universität Potsdam, 2015. URL: https://www.uni-potsdam.de/fileadmin/projects/udkm/Documents/BaMa_theses/pude2015msc.pdf (visited on 12/31/2024).

[45] I. Radu et al. "Transient Ferromagnetic-like State Mediating Ultrafast Reversal of Antiferromagnetically Coupled Spins." In: *Nature* 472.7342 (2011), pp. 205–208. DOI: 10.1038/nature09901.

[46] D. Royer and E. Dieulesaint. *Elastic Waves in Solids I: Free and Guided Propagation*. Springer Science & Business Media, 1999. 394 pp. ISBN: 978-3-540-65932-7.

[47] L. Sandlund et al. "Magnetostriction, Elastic Moduli, and Coupling Factors of Composite Terfenol-D." In: *Journal of Applied Physics* 75.10 (1994), pp. 5656–5658. DOI: 10.1063/1.355627.

[48] D. Schick et al. "udkm1Dsim—A Simulation Toolkit for 1D Ultrafast Dynamics in Condensed Matter." In: *Computer Physics Communications* 185.2 (2014), pp. 651–660. DOI: 10.1016/j.cpc.2013.10.009.

[49] D. Schick. "udkm1Dsim – a Python Toolbox for Simulating 1D Ultrafast Dynamics in Condensed Matter." In: *Computer Physics Communications* 266 (2021), p. 108031. DOI: 10.1016/j.cpc.2021.108031.

[50] N. Schoeni and G. Chapuis. *CrystalOgraph*. 2019. URL: https://www.epfl.ch/schools/sb/research/iphys/teaching/crystallography/crystalograph/.

[51] S. Shihab et al. "Counter-Rotating Standing Spin Waves: A Magneto-Optical Illusion." In: *Physical Review B* 95.14 (2017), p. 144411. DOI: 10.1103/PhysRevB.95.144411.

[52] Y. Shiroishi et al. "Future Options for HDD Storage." In: *IEEE Transactions on Magnetics* 45.10 (2009), pp. 3816–3822. DOI: 10.1109/TMAG.2009.2024879.

[53] J. Sievers. "Asphericity of $4f$-Shells in Their Hund's Rule Ground States." In: *Zeitschrift für Physik B Condensed Matter* 45.4 (1982), pp. 289–296. DOI: 10.1007/BF01321865.

[54] J. Smit and H. G. Beljers. "Ferromagnetic Resonance Absorption in $BaFe_{12}O_{19}$, a Highly Anisotropic Crystal." In: *Philips Res. Rep.* 10 (1955), pp. 113–130.

[55] A. von Reppert et al. “Persistent Nonequilibrium Dynamics of the Thermal Energies in the Spin and Phonon Systems of an Antiferromagnet.” In: *Structural Dynamics* 3.5 (2016), p. 054302. DOI: 10.1063/1.4961253.

[56] A. von Reppert et al. “Unconventional Picosecond Strain Pulses Resulting from the Saturation of Magnetic Stress within a Photoexcited Rare Earth Layer.” In: *Structural Dynamics* 7.2 (2020), p. 024303. DOI: 10.1063/1.5145315.

[57] A. von Reppert. “Magnetic Strain Contributions in Laser-Excited Metals Studied by Time-Resolved X-ray Diffraction.” Universität Potsdam, 2022, 61659 KB, XV, 311 pages. DOI: 10.25932/PUBLISHUP-53558.

[58] A. von Reppert. “Ultrafast Magnetostriction in Dysprosium Studied by Femtosecond X-Ray Diffraction.” Universität Potsdam, 2015. URL: https://www.uni-potsdam.de/fileadmin/projects/udkm/Documents/BaMa_theses/repp2015msc.pdf (visited on 11/29/2024).

[59] J. H. Weaver, D. W. Lynch, and C. G. Olson. “Optical Properties of Niobium from 0.1 to 36.4 eV.” In: *Physical Review B* 7.10 (1973), pp. 4311–4318. DOI: 10.1103/PhysRevB.7.4311.

[60] L. Willig. “Ultrafast Magneto-Optical Studies of Remagnetisation Dynamics in Transition Metals.” Universität Potsdam, 2019. URL: https://www.uni-potsdam.de/fileadmin/projects/udkm/Documents/PhD_theses/will2019phd.pdf (visited on 12/19/2024).

[61] M. Winter. *Titanium*. WebElements. 2024. URL: https://winter.group.shef.ac.uk/webelements/titanium/ (visited on 11/06/2024).

[62] J. Yang et al. “Diffractive Imaging of a Rotational Wavepacket in Nitrogen Molecules with Femtosecond Megaelectronvolt Electron Pulses.” In: *Nature Communications* 7.1 (2016), p. 11232. DOI: 10.1038/ncomms11232.

[63] E. B. Zaretsky and G. I. Kanel. “Invariability of Rate Dependences of Normalized Flow Stress in Niobium and Molybdenum under Conditions of Shock Compression.” In: *Journal of Applied Physics* 120.10 (2016), p. 105901. DOI: 10.1063/1.4962509.

[64] S. P. Zeuschner et al. “Tracking Picosecond Strain Pulses in Heterostructures That Exhibit Giant Magnetostriction.” In: *Structural Dynamics* 6.2 (2019), p. 024302. DOI: 10.1063/1.5084140.

[65] S. P. Zeuschner. “Magnetostriction and Timeresolved X-ray Diffraction on $TbFe_2$.” Universität Potsdam, 2017. URL: https://www.uni-potsdam.de/fileadmin/projects/udkm/Documents/BaMa_theses/zeus2017msc.pdf (visited on 11/15/2024).

A Appendix

A.1 Raw static hysteresis loop data

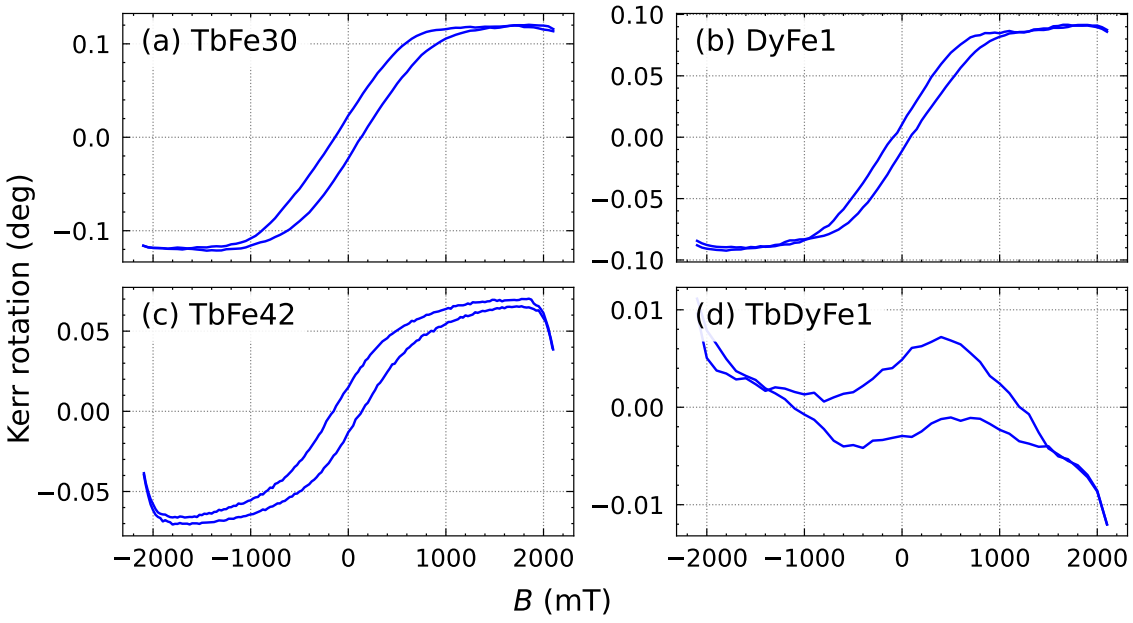

Figure 55: Uncorrected static hystereses of the three thin $REFe_2$ samples (a, b, d) and the thick uncapped $TbFe_2$ sample (c).

A.2 Fit results for demagnetization timescales in thin $REFe_2$

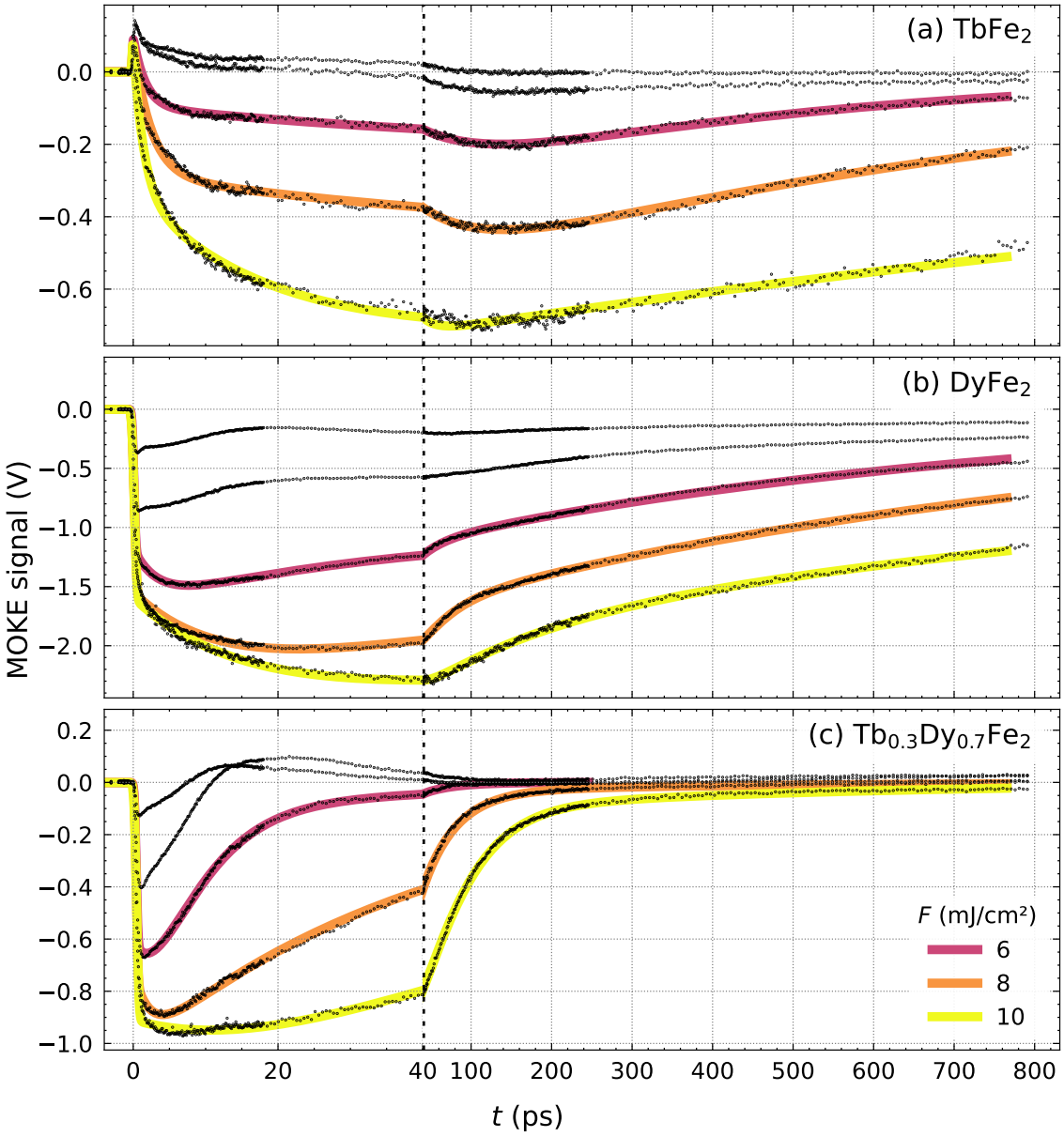

Figure 56: Fluence series for 20 nm $REFe_2$ specimen at the maximum external field $B_{ext} = 1400\,mT$ with the fitted curves for the three highest fluences. The fit parameters are given in table 5.

A.3 Additional data for rotation series thin $REFe_2$

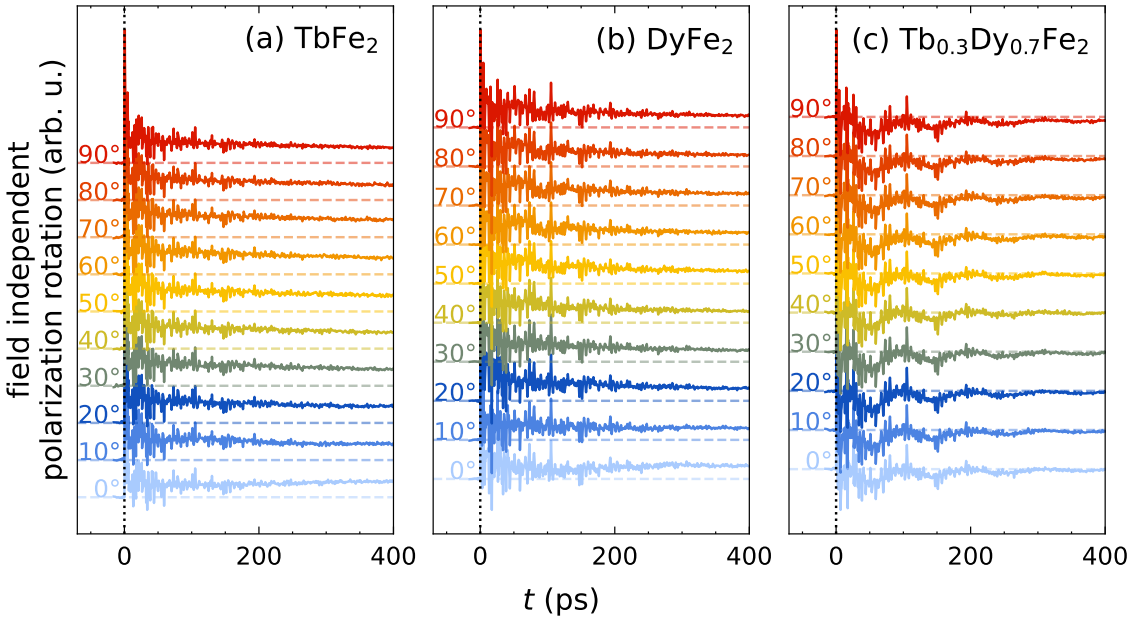

Figure 57: External field angle dependent measurements of the field-independent polarization rotation. As expected for a field-independent signal, the field angle does not significantly change these signals. The characteristic 10 GHz oscillation is again observed in Terfenol-D. As discussed in section 5.1.3, this feature may be caused by echos of shear waves.

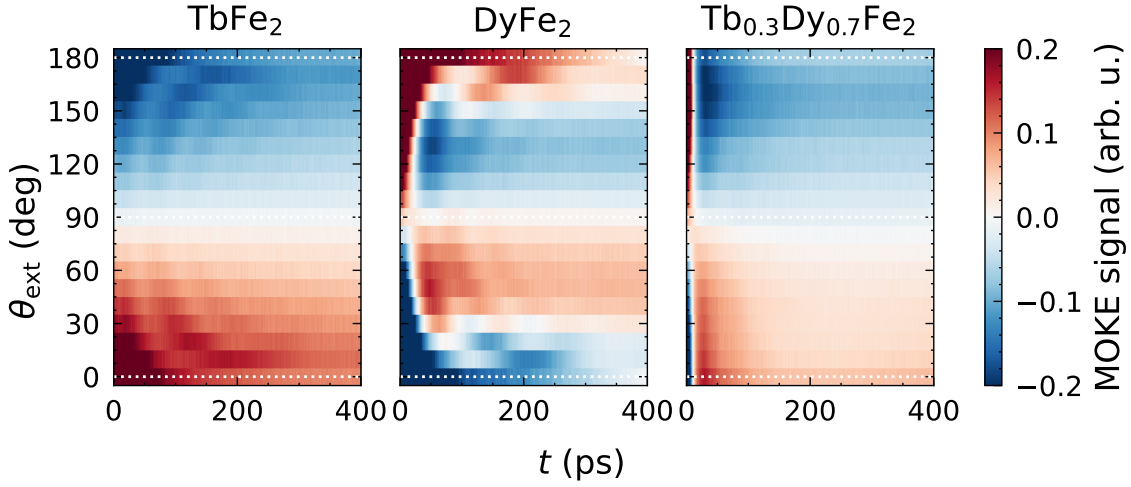

Figure 58: Comparison of the field angle dependent trMOKE measurements for the thin $REFe_2$ samples, showing the symmetry around 90°.

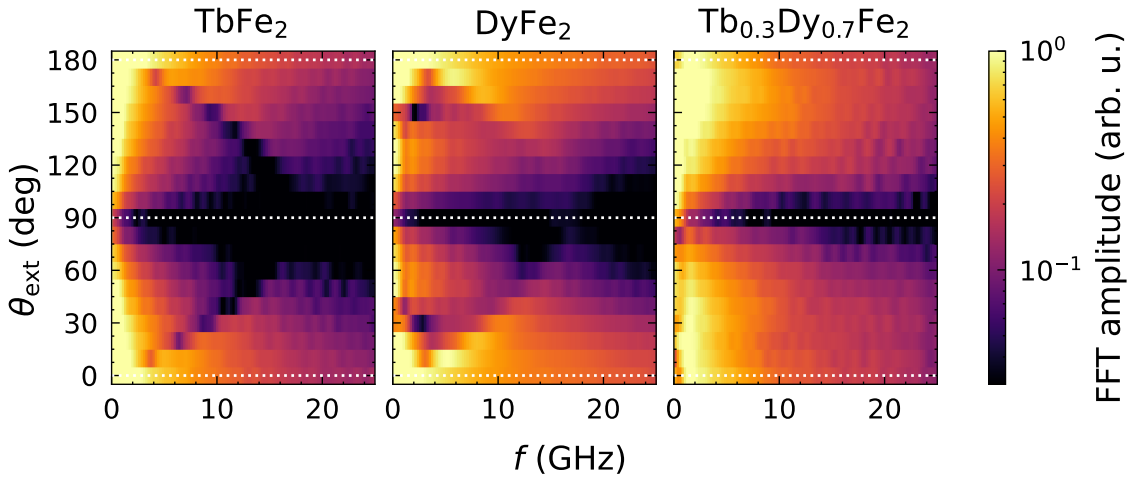

Figure 59: Fourier transforms of the full 180° datasets for all three $REFe_2$ materials, showing the symmetry around 90° and the precession frequencies, ranging from 5 to 15 GHz.

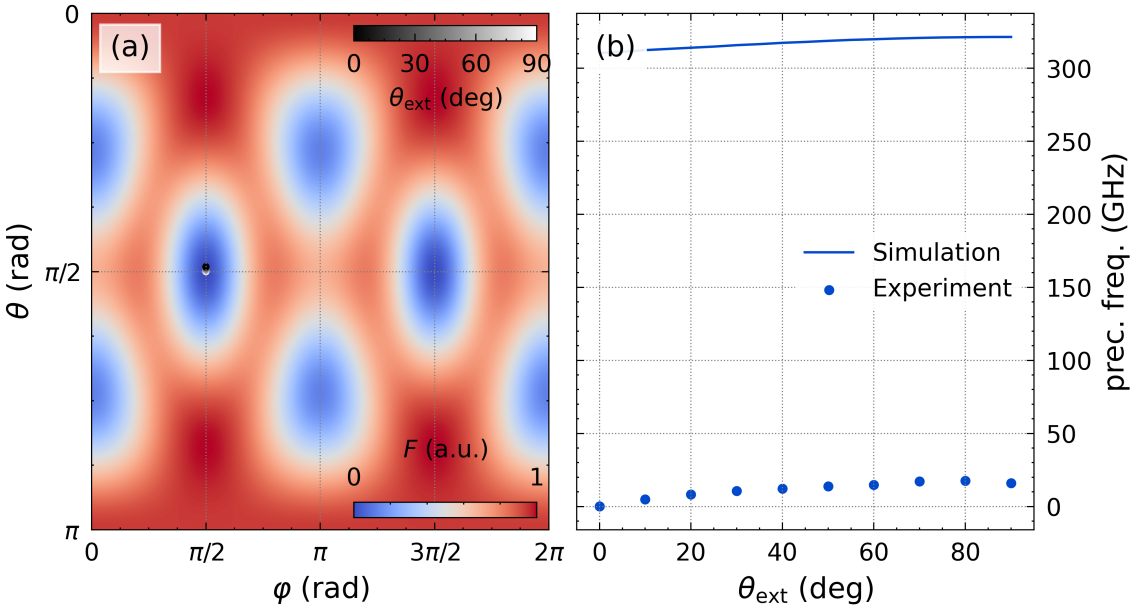

Figure 60: Simulation results for the free energy surface of $DyFe_2$ without an external field, plotted here as a 2D map, and the equilibrium magnetization orientation for a set of external field angles between 0° and 90° with a field strength of 350 mT (a). From the simulation follows that with the available external field the magnetization always stays close to the initial equilibrium position. This results in very high frequencies above 300 GHz, which were not observed during the experiments (b).

Acknowledgments

Writing the master thesis is an important step towards independent scientific work, that requires a lot of patience and perseverance. Without the help of many people, completing this project would have been impossible. I am grateful to everyone who supported me throughout the past year.
First and foremost, I want to thank Prof. Matias Bargheer for giving me the opportunity to work on this project and explore the fascinating topic of ultrafast magnetization dynamics. His optimism and enthusiasm about science were a constant source of motivation for me. His openness to discussing the latest results from the lab and his invaluable feedback have been fundamental to my work.
A special thank you goes to my supervisor Dr. Alexander von Reppert, for his outstanding support and guidance. His helpful ideas and suggestions were essential for my progress, and I really appreciate the time he dedicated to helping not just me, but everyone who sought his advice. His broad knowledge and attention to detail have steered me throughout this project and inspired me to continuously challenge and improve myself.
I also want to thank Fried Weber for supporting me in the lab and for our insightful discussions, especially about the theory and simulations of magnetization dynamics. His expertise has been immensely helpful in advancing my understanding.
I would also like to extend my appreciation to the entire UDKM group for fostering such a friendly, collaborative, and productive atmosphere. Each of you has motivated me in unique ways and helped me feel welcome in this new environment.
Finally, I want to thank my friends; without our little study group I certainly would not have made it even past the first bachelor semester. I am very grateful for your support and patience, and the time we could spend together.
Last, but absolutely not least, I want to thank my family, especially my parents, for their constant, unconditional support even in challenging times. Your encouragement and belief in me have been the foundation of my success. Without you, none of this would have been possible.

Authorship declaration

I hereby declare that I have prepared this master thesis independently, have not submitted it elsewhere for examination purposes and have not used any aids other than those specified. All knowingly used text excerpts, quotations or contents of other authors have been explicitly marked as such.

Potsdam, 15.01.2025

Constantin Walz